Aus dem Zentrum Physiologie und Pathophysiologie der
Universität zu Köln
Institut für Vegetative Physiologie

Geschäftsführende Direktorin: Universitätsprofessorin Dr.
rer. nat.T. Korotkova

Mitochondrial DNA deletions and depletion in dermal fibroblasts

Inaugural-Dissertation zur Erlangung der Doktorwürde der
Medizinischen Fakultät
der Universität zu Köln

vorgelegt von
Lena Katharina Reiter aus
Blaubeuren

promoviert am 26.Mai 2026

Gedruckt mit Genehmigung der Medizinischen Fakultät der Universität zu Köln

2026

Dekan: Universitätsprofessor Dr. med. G. R. Fink

1. Gutachterin: Privatdozentin Dr. med. J. Nätlitz
2. Gutachterin: Universitätsprofessorin Dr. rer. nat. A. Trifunovic

Erklärung

Ich erkläre hiermit, dass ich die vorliegende Dissertationsschrift ohne unzulässige Hilfe Dritter und ohne Benutzung anderer als der angegebenen Hilfsmittel angefertigt habe; die aus fremden Quellen direkt oder indirekt übernommenen Gedanken sind als solche kenntlich gemacht.

Bei der Auswahl und Auswertung des Materials sowie bei der Herstellung des Manuskriptes habe ich keine Unterstützungsleistungen erhalten.

Weitere Personen waren an der Erstellung der vorliegenden Arbeit nicht beteiligt. Insbesondere habe ich nicht die Hilfe einer Promotionsberaterin/eines Promotionsberaters in Anspruch genommen. Dritte haben von mir weder unmittelbar noch mittelbar geldwerte Leistungen für Arbeiten erhalten, die im Zusammenhang mit dem Inhalt der vorgelegten Dissertationsschrift stehen.

Die Dissertationsschrift wurde von mir bisher weder im Inland noch im Ausland in gleicher oder ähnlicher Form einer anderen Prüfungsbehörde vorgelegt.

Die dieser Arbeit zugrunde liegenden Experimente sind nach entsprechender Anleitung von von Frau PD Dr. med. Jana Nätlitz und der medizinisch-technischen Assistentin Frau Nadine Niehoff von mir selbst ausgeführt worden. Dazu gehören Zellkultur, die Genotypisierung der Versuchstiere, die Entnahme von DNA/RNA sowie die Durchführung von PCR- und qPCR Experimenten, die Proteinentnahme, Immunoblotting und immunhistologische Färbungen.

Die Bleomycin-Injektionen an den Versuchstieren (n=14) führte ich nach erfolgreichem Abschluss des tierversuchskundlichen FELASA-B-Kurses durch. Damit erweiterte ich den bereits bestehenden Datensatz (n=5) meiner Betreuerin, PD Dr. med. Jana Nätlitz. Das Scoring, die Tötung und die Entnahme des Hautgewebes wurden von mir in Zusammenarbeit mit Frau Nadine Niehoff getätigt. Alle Auswertungen wurden nach entsprechender Anleitung von mir vorgenommen.

Die verwendeten Softwares umfassten Excel, CellProfiler, Fiji, NDP.view2, Prism und Inkscape. Die Einweisungen zu den Mikroskopen in der Imaging Facility im CECAD und den Softwares NDP.view2 und Cellprofiler erfolgten durch Dr. Christian Jüngst und Peter Zentis.

FACS-Analysen wurden im ZMMK von Dr. Gunter Rappl sowie im Zentrum für Biochemie mit Frau Dr. Julia Etich durchgeführt.

Erklärung zur guten wissenschaftlichen Praxis:
Ich erkläre hiermit, dass ich die Ordnung zur Sicherung guter wissenschaftlicher Praxis und zum Umgang mit wissenschaftlichem Fehlverhalten (Amtliche Mitteilung der Universität zu Köln AM 132/2020) der Universität zu Köln gelesen habe und verpflichte mich hiermit, die dort genannten Vorgaben bei allen wissenschaftlichen Tätigkeiten zu beachten und umzusetzen.
Köln, den 25.09.2024

Unterschrift: .....

Danksagung

Mein herzlichster Dank geht an

Herrn Prof. Dr. rer. nat. Rudolf Wiesner, für die Vergabe meines Dissertationsthemas sowie für seine fortwährende Betreuung während meiner Zeit im Labor. Seine wissenschaftliche Expertise, Geduld und die durchgehend gewährte Unterstützung sowie seine wertvollen Ratschläge haben mir geholfen diese Arbeit zu verwirklichen und mich stets motiviert, mein Bestes zu geben.

meiner Betreuerin und Doktormutter, Frau PD Dr. med. Jana Nätlitz, die mich vom ersten Tag an begleitete und mir den Einstieg in die Welt der Wissenschaft ermöglichte. Durch ihre wertvollen Hinweise, konstruktiven Anregungen und ihre beständige Unterstützung, sowohl fachlich als auch persönlich, konnte ich zahlreiche Herausforderungen meistern und mein Forschungsprojekt erfolgreich abschließen. Die Zusammenarbeit mit ihr hat mir das nötige Selbstvertrauen und die Zuversicht gegeben, zukünftige berufliche Herausforderungen zu bewältigen.

unseren technischen Assistentinnen, Frau Nadine Niehoff und Frau Katrin Lanz. Von Frau Niehoff habe ich maßgeblich praktische Fertigkeiten und das notwendige Gefühl für den wissenschaftlichen Alltag im Labor erlernt. Frau Lanz danke ich für ihre moralische Unterstützung und ihr unerschütterliches Vertrauen in mich.

unsere Postdocs Dr. Thomas Paß, Prof. David Pla-Martín und Dr. Julia Boix. Ihre fachliche Expertise und die wertvolle Unterstützung bei der Interpretation wissenschaftlicher Ergebnisse sowie bei zahlreichen Eckpunkten meiner Dissertation waren für meinen Fortschritt von unschätzbarem Wert.

Dr. Julia Etich und Dr. Gunter Rappl für ihre praktische und fachliche Unterstützung bei FACS-Analysen. Mein Dank geht auch an Prof. Dr. Thomas Krieg, dessen inhaltliche Denkanstöße unsere Publikation bereichert haben.

Dr. Christian Jüngst, der mir mit Geduld und Hingabe die Grundlagen der Mikroskopie vermittelt hat, sowie bei Herrn Peter Zentis, der mir bei der Auswertung von Kollagenmatrizen eine essenzielle Anlaufstelle war.

die Dermatohistologie-Abteilung für die Unterstützung bei der H&E- und TM-Färbung unserer Hautschnitte sowie bei PD Dr. Doris Helbig für ihre Vermittlung dermatohistopathologischer Auswertung von Morphea-Proben aus der BioMaSOTA-Datenbank.

das Team der Tierhaltung in der Pharmakologie für ihre stets reibungslose und zuverlässige Unterstützung, die für unsere Tierversuche unverzichtbar war.

den mir zur Verfügung gestellten Stipendien, SFB829 und Köln Fortune, die es mir ermöglicht haben, mich vollständig diesem Projekt zu widmen.

meine englischen Freunde Maureen und Paddy, die mühsam die sprachlichen Korrekturen meiner Doktorarbeiten übernommen haben.

meine Familie, insbesondere Eltern und Geschwistern, die mir stets Rückhalt gegeben und an mich geglaubt haben. Ohne ihre Unterstützung wäre mein heutiger Weg nicht denkbar.

meine Kommilitoninnen und Kommilitonen der Universität zu Köln: Janina, Noah, Miriam, David, Leo, Anna, Naresh, Max, Lene, Leonie. Sie haben mir eine wertvolle Gemeinschaft unter den Promovierenden geboten.

meinen Mitbewohnerinnen und Mitbewohnern sowie Freunden Naomi, Hans, Vincent, Helen und Lina danken, die stets für Ablenkung sorgten und mir den Spaß am Leben in anstrengenden Zeiten vor Augen hielten.

Michi, der mir nicht nur den Mut gab, eine experimentelle Doktorarbeit zu beginnen, sondern mich durch alle Höhen und Tiefen dieser intensiven Zeit trug. Er war meine größte Stütze, mein Berater und Begleiter, mit dem ich wertvolle wissenschaftliche Diskussionen führen konnte und der mir stets zur Seite stand. Seine beständige Unterstützung und Zuversicht haben maßgeblich an dieser Arbeit beigetragen.

An Sonja und Ilja,

Table of contents

Abbreviations

α-SMA	α-Smooth Muscle Actin
ATP	Adenosine Triphosphate
BMP	Bone morphogenetic protein
CD	Common deletion
DNA	Deoxyribonucleic acid
ECM	Extracellular Matrix
EMT	Epithelial-to-Mesenchymal Transition
EndoMT	Endothelial-to-Mesenchymal-Transition
ETC	Electron Transport Chain
FAO	Fatty Acid Oxidation
FGF	Fibroblast Growth Factor
IL	Interleukin
IPF	Idiopathic pulmonary fibrosis
KO	Knockout
MMT	Mesothelial-to-mesenchymal-transition
mtDNA	Mitochondrial DNA
mtSSB	mtDNA single-stranded DNA-binding proteins
MTCO1	Mitochondrially encoded cytochrome c oxidase I
NTP	Nucleotide Triphosphate
nucDNA	Nuclear DNA
OxPhos	Oxidative Phosphorylation
PCG-1α	Peroxisome proliferator-activated receptor gamma coactivator 1- α
PDGF	Platelet-Derived-Growth-Factor
Polymerase γ	POL-γ
ROS	Reactive Oxygen Species
SASP	Senescence-Associated-Secretory-Phenotype
SSc	Systemic Sclerosis
TFAM	Mitochondrial Transcription Factor A
TGF-β	Transforming growth factor β
$Twinkle^{FIBRO}$	TwinkleK320E Col1α2Cre+

1. Summary

This study explores the impact of mitochondrial DNA (mtDNA) mutations on metabolic and physiological functions in dermal fibroblasts. Mitochondria, providing an important source of the cellular energy requirements, are essential in multiple vital processes. Thus, mtDNA damage often resulting from mutations and consequently leading to mitochondrial stress, can drive ageing, inflammation and cancer. Diseases characterised by large mtDNA deletions, such as progressive external ophthalmoplegia (PEO) or sensory ataxic neuropathy with dysarthria and ophthalmoparesis (SANDO) syndrome, are known to shorten lifespan and present with severe neuromuscular and neurodegenerative symptoms. Dermatological features, which may include rashes, hair abnormalities and altered pigmentation, have been occasionally reported in these conditions, but remain poorly investigated.

Dermal fibroblasts are crucial in maintaining skin homeostasis, orchestrating numerous functions, such as extracellular matrix production, wound healing and immune responses. These energy-demanding functions require an efficient mitochondrial energy supply, which starts to deteriorate with damaged mtDNA, mitochondrial dysfunction and ageing-associated decline. mtDNA damage in fibroblasts has been described upon UV irradiation, where mtDNA deletions accumulate, resulting in key skin ageing signs, such as dermal thinning, loss of elasticity and the formation of wrinkles. However, mutated mtDNA can accumulate to a certain threshold without causing measurable functional harm to the cell or organ, leading to a mosaic picture of normal and damaged cells in the tissue. These facts underline the importance of studying correlations between mtDNA damage and cellular function in fibroblasts.

Here, the effect of accumulating mtDNA deletions in the skin, resembling the physiological ageing process, was investigated. A mouse model, harbouring a dominant-negative mutation (K320E) of the mitochondrial helicase Twinkle, a crucial enzyme in mtDNA replication, was used. The mutation associated with PEO and SANDO syndrome can be activated specifically in dermal fibroblasts by Tamoxifen (Twinkle^{FIBRO}; Rosa26-STOP-loxP-Cre-System). To assess the role of mtDNA in fibroblasts, cells were examined under normal and challenged conditions. mtDNA deletions accumulate in Twinkle^{FIBRO} fibroblasts *in vivo. In vitro,* fibroblasts show increased replication rates favouring transmission of shorter mtDNA, gradually resulting in mtDNA depletion, while maintaining a functional respiratory chain. They show decreased proinflammatory and fibrotic mediators *in vitro*, and Bleomycin-induced fibrosis is dampened in Twinkle^{FIBRO} mice *in vivo*. This is partly due to an attenuated differentiation of Twinkle^{FIBRO} fibroblasts into myofibroblasts.

2. Zusammenfassung

In dieser Studie haben wir die Auswirkungen mitochondrialer DNA (mtDNA) Mutationen auf die physiologischen Funktionen von Hautfibroblasten untersucht. Mitochondrien, die eine wichtige Quelle für den Energiebedarf der Zelle darstellen, sind für viele lebenswichtige Prozesse essenziell. Schäden an der mtDNA, die häufig durch Mutationen entstehen, führen zu mitochondrialem Stress und können zu Alterungsprozesse, Entzündungen und Krebs beitragen. Erkrankungen mit großen mtDNA-Deletionen wie die progressive externe Ophthalmoplegie (PEO) oder das SANDO-Syndrom (sensorische ataktische Neuropathie mit Dysarthrie und Ophthalmoparese) verkürzen die Lebensspanne und verursachen schwere neuromuskuläre und neurodegenerative Symptome. Dermatologische Begleiterscheinungen wie Hautausschläge, Haarveränderungen und Pigmentstörungen sind gelegentlich beschrieben, aber wenig erforscht.

Dermale Fibroblasten sind entscheidend für die Aufrechterhaltung der Hauthomöostase indem sie zahlreiche Funktionen wie die Produktion der extrazellulären Matrix, Wundheilung und Immunantworten steuern. Diese energieintensiven Prozesse hängen von einer intakten mitochondrialen Funktion ab, die mit Alter, mtDNA-Schäden und Dysfunktion abnimmt. Besonders bei UV-induzierten Mutationen wurden mtDNA-Deletionen mit

Hautalterungszeichen wie Verdünnung der Dermis, Elastizitätsverlust und Faltenbildung in Verbindung gebracht. Dabei kann sich mutierte mtDNA bis zu einem gewissen Schwellenwert ansammeln, ohne die Zellfunktion nachweisbar zu beeinträchtigen – was zu einem Mosaik gesunder und geschädigter Zellen führt. Dies verdeutlicht die Relevanz, den Zusammenhang zwischen mtDNA-Schäden und Zellfunktion in Fibroblasten weiter zu erforschen.

In dieser Arbeit wurden die Auswirkungen von akkumulierenden mtDNA-Deletionen in der Haut untersucht, die dem physiologischen Alterungsprozess ähnelt. Zu diesem Zweck verwendeten wir ein Mausmodell mit einer dominant-negativen Mutation (K320E) der mitochondrialen Helikase Twinkle, einem Schlüsselenzym der mtDNA-Replikation. Durch Tamoxifenfütterung wird die mit PEO und SANDO assoziierte Mutation spezifisch in dermalen Fibroblasten aktiviert (Twinkle^{FIBRO}; Rosa26-STOP-loxP-Cre-System). Um zu verstehen, welche Rolle geschädigte mtDNA in Fibroblasten spielt, untersuchen wir Fibroblasten unter normalen und belastenden Bedingungen. Das Modell zeigt, dass mtDNA-Deletionen in Twinkle^{FIBRO} Fibroblasten *in vivo* akkumulieren. *In vitro* zeigten diese Fibroblasten eine erhöhte Replikationsrate, was die Weitergabe verkürzter mtDNA begünstigt und allmählich zu einer mtDNA-Depletion führt, während die Atmungskette unbeeinträchtigt bleibt. Twinkle^{FIBRO} Fibroblasten zeigten eine anti-entzündliche Signatur *in vitro*, und Bleomycin-induzierte Fibrose war in Twinkle^{FIBRO} Mäusen abgeschwächt, was unter anderem auf eine reduzierte Differenzierung zu Myofibroblasten zurückzuführen ist.

3. Introduction

This study explores the effects of mitochondrial DNA (mtDNA) mutations on dermal fibroblast metabolism and physiology, focusing on the impact of mtDNA deletions and depletion on mitochondrial function and skin homeostasis.

3.1 Background and project overview

Mitochondria are essential organelles in eukaryotic cells, primarily known for supplying energy through oxidative phosphorylation (OxPhos). Beyond generating ATP, mitochondria are pivotal for regulating calcium levels, orchestrating proliferation and apoptosis, synthesising membrane lipids, nucleotides, but also heme and steroids, making them essential for maintaining tissue homeostasis[1]. These functions, however, are susceptible to changes in the mitochondrial genome. Damage to mtDNA leads to accumulating mutations that disrupt mitochondrial function, causing cell death and compromising organ integrity. This simplified mechanism is involved in various pathomechanisms, such as mitochondrial diseases, chronic inflammation, tumour formation, and ageing[2,3].

Compared to nuclear DNA (nucDNA), the mitochondrial genome is more error-prone, given the less effective repair mechanisms, higher replication rates and proximity to reactive oxygen species (ROS) generated during mitochondrial respiration[4]. Maternally transmitted and somatic mtDNA mutations contribute to the overall mtDNA mutation load[5]. These mutations can coexist with wild-type mtDNA, a state termed heteroplasmy[3], where clonal expansion of mutated mtDNA can lead to dysfunction if the mutation load surpasses a “biochemical threshold”. This results in compromised mitochondrial function and OxPhos[6]. The resulting respiratory chain (RC)-deficient cells can create a mosaic pattern within the tissue, disrupting organ function once a “phenotypical threshold” is exceeded. However, studies underscore the organ-specific threshold for mtDNA mutations to induce RC deficiency and tissue impairment, which highly depends on organs, cells and the individuum itself[6,7].

Genetic mitochondrial diseases, like progressive external ophthalmoplegia (PEO), the severe sensory ataxic neuropathy with dysarthria and ophthalmoparesis (SANDO) syndrome, and Kearns–Sayre syndrome[8], are characterised by large mtDNA deletions. In these multisystemic diseases, tissues with high energy demands such as skeletal muscle, the heart and the brain are affected[9-11]. Thus, severe symptoms such as lactic acidosis, atrioventricular blocks, cardiomyopathies, seizures and strokes impact mortality. Mitochondriopathies often present early in life with childhood stunting, muscle weakness and neurodegenerative issues. However, diagnostic challenges, lack of therapies, and multi-organ failure frequently result in early death[12].

Mitochondrial dysfunction has been increasingly associated with age-related pathologies and has been identified as a hallmark of ageing (Figure 1)[13]. It has become clear that mtDNA alterations such as point mutations, deletions, and depletion drive ageing processes and reduce lifespan, without necessarily resulting in RC deficiency. This underlines the importance of distinguishing mtDNA damage and mitochondrial damage[14,15]. *POLGA* (polymerase-γ) knock-in mice, which express a proof-reading-deficient version of DNA polymerase, show that a substantial increase in mtDNA point mutations and deletions leads to a variety of premature ageing symptoms, including osteopenia, anaemia, heart enlargement, alopecia and reduced subcutaneous fat[14]. There has been emerging research in the accumulation of mtDNA damage in energy-demanding post-mitotic tissues such as the heart, muscle and brain, correlating with ageing and age-related diseases[2]. For instance, mtDNA alterations and mitochondrial-related genes have been widely demonstrated to foster neurodegenerative processes such as Alzheimer's or Parkinson's disease[16]. Our laboratory could link mosaic RC-deficient cardiomyocytes in mice, reflecting the ageing heart, to the development of cardiac arrhythmia[17].
Despite significant advances in understanding mitochondrial dysfunction in various tissues, the skin, as the body's largest organ serving multiple roles such as barrier protection, thermal regulation, hydration, sensory perception and immune defence, remains underexplored. While mitochondriopathies such as SANDO-syndrome or KSS predominantly manifest with severe neurodegenerative and skeletomuscular conditions, due to the high energy demands of these tissues, skin-related issues are often overlooked, likely masked by the severity of lifethreatening symptoms. However, a relevant fraction of patients present with dermatological symptoms, including rashes, hair abnormalities and altered pigmentation[18,19]. Thus, skin pathologies can be associated with mitochondriopathies and occasionally indicate genetic disorders.
mtDNA deletions are prevalent in ageing skin, particularly in sun-exposed areas[20]. Notably, UV irradiation penetrates the skin and increases the number of large-scale mtDNA deletions, either directly or through Reactive Oxygen Species (ROS) formation, contributing to oxidative base damage[21]. Specifically, UV-A directly impacts dermal fibroblasts and induces mtDNA deletions, such as the well-characterised "common deletion"[22]. Dermal fibroblasts, the dominant cells in the dermis, are key homeostasis regulators and have functions, such as wound healing orchestration, extracellular matrix (ECM) production and immunological signalling. In the context of UV-A radiation, a decline in these functions results in the pathognomonic features of photoageing, including dermal thinning, loss of elasticity, formation of wrinkles, and impairment of the skin's barrier function.
UV-A radiation is therapeutically used for various dermatological conditions, including fibrotic disorders like Morphea or Scleroderma, which underlie chronic inflammation and excessive

ECM production by activated fibroblasts (myofibroblasts). Several mechanisms of phototherapy improving fibrotic burden have been elucidated, including increased apoptosis, immunomodulation and antifibrotic effects[21], while a potential contribution of mtDNA deletions remains largely unknown. However, the role of mtDNA damage and mitochondrial dysfunction has been of recent interest in fibrotic disorders. Fibroblasts derived from Systemic Scleroderma (SSc) skin revealed a significant increase in mitochondrial respiration, driven by a higher OxPhos demand, with an overall loss of respirasomes (supercomplex of Complex I, II and IV)[23]. Furthermore, in SSc fibroblasts, the mitochondrial transcription factor A (TFAM), which is crucial for mtDNA replication, was shown to be reduced, concomitant with a mtDNA copy number loss and increased release of mtDNA in damaged cells[24]. Regarding the mutation load threshold resulting in mitochondrial respiration dysfunction, fibroblasts seem to tolerate high levels of deletions, although this has not yet been investigated and may be affected by triggers such as fibrosis[6,25]. Further research into mtDNA mutations in dermal fibroblasts is crucial, enabling a better understanding of their potential role in human health and lifespan. In this project, we focus on fibroblast function while accumulating mtDNA deletions to further understand how they rely on functioning mitochondria to maintain skin homeostasis. We apply a mouse model harbouring a dominant-negative mutant of the mitochondrial replicative helicase Twinkle (Rosa26-STOP System), expressing the fibroblast-specific Cre Recombinase (Collagen1A2 Cre^{ERT}/R26-K320E-Twinkle, short: $Twinkle^{FIBRO}$) activated upon Tamoxifen treatment. Thus, mtDNA deletions accumulate specifically in dermal fibroblasts upon Tamoxifen treatment, mimicking physiological fibroblast ageing. Moreover, under *in vitro* conditions where proliferation occurs, the mitochondrial replicative machinery is impaired, leading to a gradual depletion of mtDNA. Therefore, this model is ideal for studying the specific consequences of mtDNA damage.

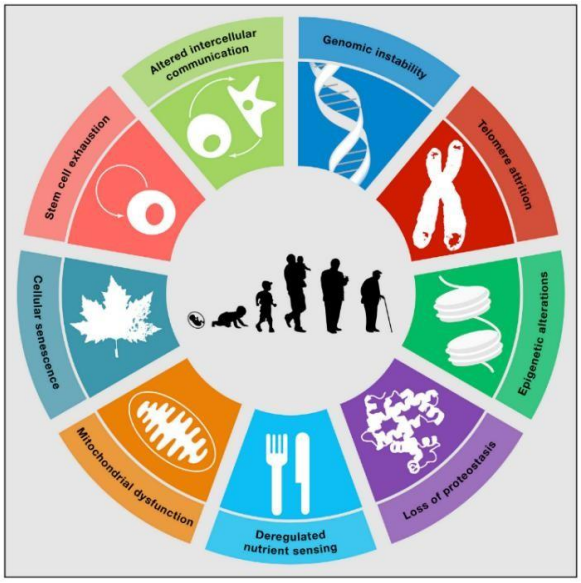

Figure 1: Hallmarks of ageing. This scheme outlines some of the most well-studied hallmarks of ageing, including mitochondrial dysfunction, which we will focus on in this study. This figure is adapted from Hallmarks of Ageing: an Expanding Universe, Lopez-Ótin et al. in Cell, 2023[13].

3.2 Skin structure and function

The skin is the largest human organ, acting as a sheath separating the body from the external environment and performing various functions. It prevents chemical and pathogen intrusion, limits water loss, plays key roles in immune regulation, orchestrates thermoregulation and wound healing, enables sensory perception and contributes to vitamin D synthesis through UV-dependent metabolisation[26,27,28].

The skin comprises three layers (Figure 2). The outer layer is the epidermis, which consists of keratinocytes firmly attached to the dermis by dermal-epidermal junctions (see 3.2.1). The dermis is the underlying connective tissue layer, containing abundant collagen and elastin fibres. It separates the epidermis from the subcutis, mostly consisting of loose connective tissue and fat. Figure 3 depicts and describes the anatomical differences between the skin of mice and humans.

3.2.1 Epidermis

The epidermis, measuring between 0.1 and 1mm in thickness, contains no blood vessels and several layers of tightly packed cells, mainly keratinocytes, melanocytes, and Merkel cells. Once generated in the basal layer, these cells grow vertically toward the upper layer in a process called terminal differentiation[29]. In the outer layer, dead keratinocytes contain keratin and build a stratified squamous epithelium. The dermal-epidermal junction is a dynamic interface interdigitating between the epidermis and the dermis, ensuring mechanical shear resistance, intercellular connection and biomolecular diffusion. This region includes the basal layer of the epidermis, the basement membrane, and the papillary dermis. The first is the deepest layer of the epidermis, consisting of a single row of keratinocytes, and is attached to the basement membrane via hemidesmosomes. The basement membrane, further divided into the lamina lucida and lamina densa, is a thin layer containing glycoproteins and collagens. This region contains anchoring complexes, including hemidesmosomes, filaments, and fibrils, extending from the lamina densa into the papillary dermis and providing structural integrity[30].

3.2.2 Dermis

The dermis beneath the basement membrane of the epidermis varies in thickness between 0.3 mm and 3.0 mm, thickest on palms and soles and thinnest in eyelids and genitals[31]. The papillary dermis is the upper layer and comprises loosely arranged connective tissue fibres. Below is the reticular layer, consisting of densely compressed collagen fibres. The vascularised dermis nourishes the avascular cells of the epidermis and regulates body temperature. Skin firmness and adhesion arise from the interdigitation of the dermis and epidermis, where the rete pegs of the epidermis interlace with the papillary dermis, creating the unique fingerprints on human fingers[28].

The dermis consists of cells, fibres, blood vessels, and amorphous mass. In the dermis, fibroblasts are the dominant type of cells responsible for producing collagen fibres. Both will be further described in the chapters 3.2.4 and 3.2.5. The amorphous mass of the dermis consists of two glycosaminoglycans, hyaluronic acid, and dermatan sulfate. This ground substance binds to water and arbitrates the transport of hormones, nutrients, or waste products through the dermis. During movement, it acts as a lubricant substance between the collagen and elastic fibre network and dampens shocks. The dermis also hosts sweat glands, sebaceous glands, hair follicles, nerves and sensory receptors[28].

3.2.3 Subcutis

Lastly, the subcutaneous layer consists of adipose tissue, glands, blood, lymphatic vessels, and nerves. Specifically, the “white” fat represents the largest reservoir of body fat, the remaining being visceral, or “brown” fat, in infants[31]. White fat comprises adipocytes that are essential to store energy in the form of fatty acids, which can be mobilised upon need to produce ATP. Adipose tissue also covers endocrinological functions, such as glucose homeostasis, lipid metabolism, and angiogenesis[32]. This layer also contributes to thermal insulation and dampens mechanical shocks.

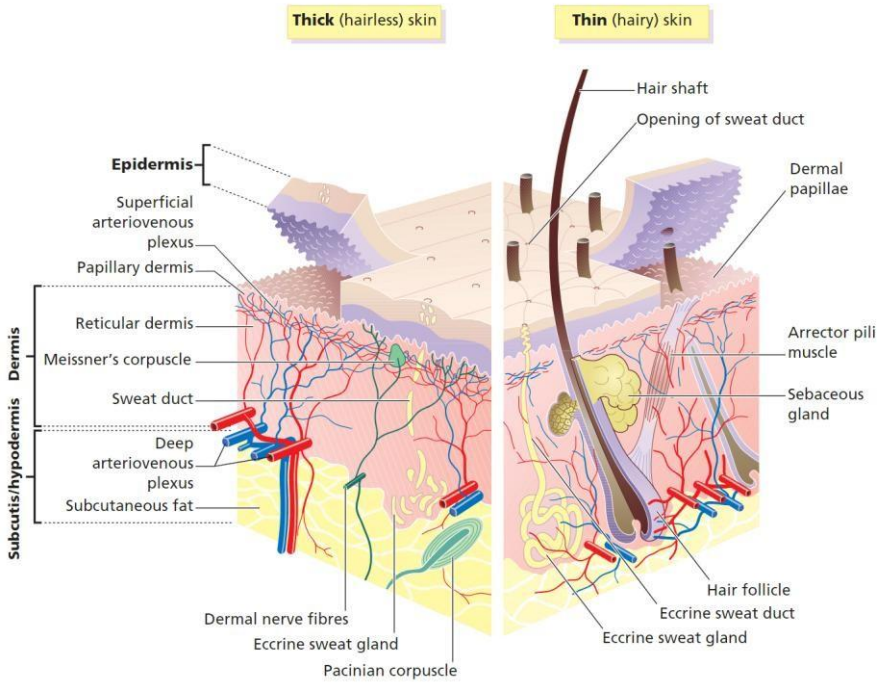

Figure 2: Skin anatomy. This three-dimensional representation highlights the main anatomical components of the three layers of the skin, namely the epidermis, dermis and hypodermis. This figure is adapted from The Function and Structure of the Skin, Weller et al., in Clinical Dermatology 5th edition, 2014[28].

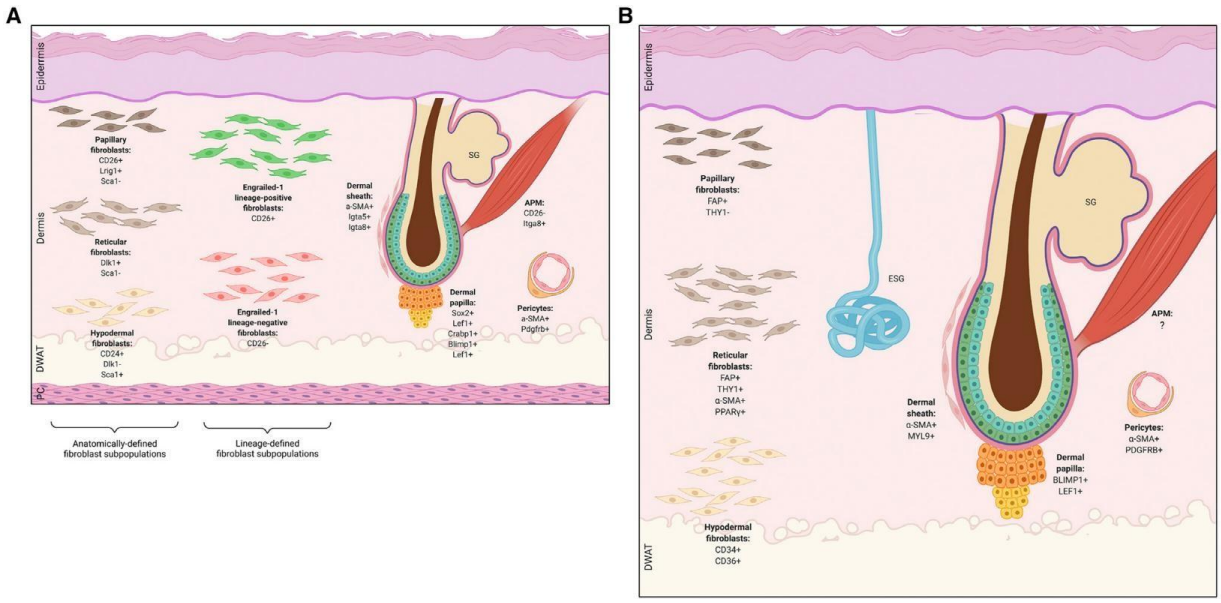

Figure 3: Skin layers of mouse and human in comparison. (A) Mouse skin structure, including the panniculus carnosus muscle [33] beneath the subcutis. **(B)** Human skin structure in direct comparison to mouse skin anatomy. All layers are thicker (100 µm in humans vs. 25 µm in mice) and contain more reticular dermal tissue. Notably, rete ridges and eccrine sweat glands (ESG) are only present in the mouse paw skin. Additionally, human skin exhibits fewer hair follicles (HFs), resulting in fewer stem cells and progenitors. The scheme also depicts various mesenchymal subpopulations. SG: sebaceous gland; DWAT: dermal white adipose tissue; APM: arrector pili muscle. This figure is adapted from Wound Healing, Fibroblast Heterogeneity, and Fibrosis, Talbott et al., Cell Stem Cell, 2022[34].

3.2.4 Fibroblasts

The most prominent cells in the dermis are fibroblasts, of interest to this project. These spindleshaped cells are ubiquitous in mammals, named for their observed role in producing new connective tissue upon wound healing in the skin (Figure 3)[35]. They are responsible for the organ-specific synthesis of extracellular matrix (ECM), consisting of collagen, proteoglycans, elastin, laminin, reticulin, and fibronectin, which are also referred to as the “matrisome”[36]. Additionally, they finely orchestrate ECM dynamics through deposition, degradation, and modification of these proteins, utilising enzymes such as matrix-metalloproteinases (MMPs) and lysyl oxidase (LOX)[37,38]. Fibroblasts also provide three-dimensional information to their environment, typically in embryonic development and tissue regeneration[39], and maintain tissue homeostasis through a fibroblast-specific secretome, including various metabolites, cytokines, and growth factors[34].

In adult skin, fibroblasts are typically quiescent but differentiate into myofibroblasts upon biochemical or physical signalling. Myofibroblasts develop contractile fibres containing αSmooth-Muscle-Actin (a-SMA), enabling ECM remodelling via traction force, together with myosin fibres[40]. They proliferate, migrate, and facilitate collagen synthesis and tissue contraction to remodel damaged tissue[41,42]. They also regulate inflammation, particularly by modulating macrophages, which is essential for pathogen defence and tissue regeneration[43]. The regulation of fibroblasts involves multiple signalling pathways, notably platelet-derived

growth factor (PDGF) and transforming growth factor-β (TGF-β). PDGF, a pro-survival growth factor, supports fibroblast development, differentiation, self-renewal, proliferation, and migration. The importance of PDGF is highlighted in mouse models with a knockin of the *pdgfra* gene, the locus of the PDGF tyrosine kinase receptor α, leading to hyperplasia of stromal fibroblasts in embryos or the development of fibrosis phenotypes[44]. On the contrary, *pdgfra* knockout in adult hair follicle dermal stem cell lineage results in a significant loss of self-renewal of stem cells and hair follicles[45]. Differentiation of myofibroblasts, however, is dominantly controlled by TGF-β (chapter 3.4). This pro-survival growth factor activates and maintains the myofibroblast state but is also involved in physiological functions such as proliferation, apoptosis, embryogenesis, angiogenesis, or tissue remodelling.

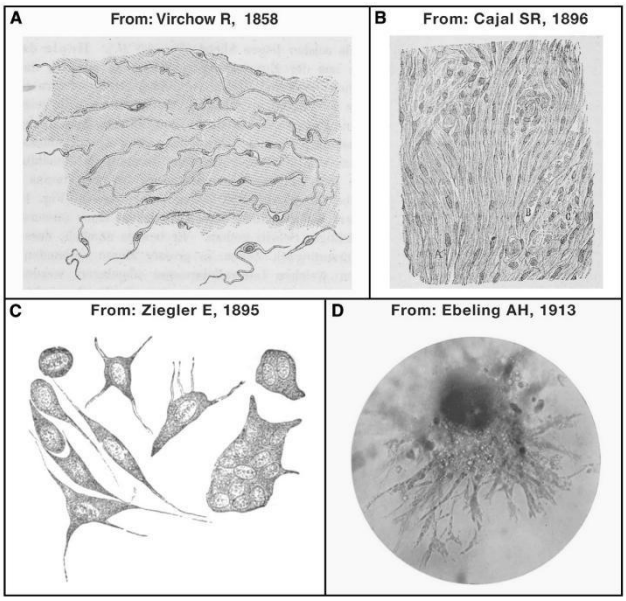

Figure 4: First representations of fibroblasts. (A) First drawings of fibroblasts by Rudolf Virchow in 1858. **(B)** Drawing of fibroblasts within newly secreted connective tissue in keloid formation, Cajal 1896. **(C)** Various representations of fibroblasts, drawn by Ziegler in 1985. **(D)** Microphotograph of embryonic chick heart fibroblasts by Ebeling in 1913. Adapted from Fibroblasts origins, definitions and functions in health and disease, Plikus et al. 2021[41].

3.2.5 Collagen

Collagen, primarily produced by myofibroblasts, is a major component of the ECM in the skin, providing firmness and preventing excessive tearing[46]. Collagen molecules comprise three polypeptide chains, forming a triple helix with non-helical segments at both ends. They build microfibrils (Figure 5 B) and aggregate into larger macrofibrils, the collagen fibres (Figure 5 D)[47]. Covalent cross-links with lysine and hydroxylysine ensure proper alignment. Type I collagen is the most prevalent, accounting for 85% of skin collagen and found in tendons and bones, while Type III collagen accounts for 15% and is present in blood vessels. Defects in collagen synthesis can lead to conditions like Osteogenesis Imperfecta and Ehlers-Danlos syndrome[47].

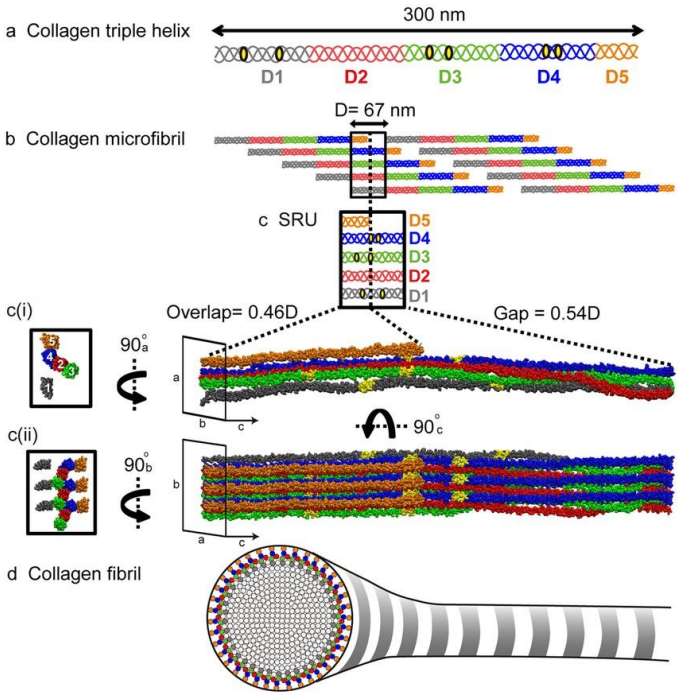

Figure 5: Collagen I structure. (A) The collagen monomer consists of a heterotrimer triple helix, two α1 and one α2 chains (300x1.5 nm). The collagen monomer is separated into five D-segments, each 67 nm long, except for D5 (30.8 nm). **(B)** Collagen microfibril. Five monomers are bundled and overlap by one D-period. **(C)** The smallest repeating unit (SRU) represents a D-period length and contains the entire sequence of all D-segments. **(Ci)** Atom model of SRU. **(Cii)** Three replicates of SRU along the b-axis to represent the fibril surface, cross section, and longitudinal view, left and right, respectively. Here, the overlap and gap regions become clear. The former contains all segments, whereas the gap lacks D5. **(D)** Collagen fibril: The collagen monomers are packed in a concentric fashion. The alternating overlap and gap regions account for the striated pattern of the fibril when stained with heavy metals and viewed under electron microscopy. The Figure is adapted from Cryptic binding sites become accessible through surface reconstruction of the type I collagen fibril, by Zhu et al. in Nature, Scientific Reports, in 2018[48].

3.3 Wound healing

A significant feature of fibroblasts is the coordination of physiological wound healing. Wound healing re-establishment injured tissue in three phases (Figure 6). First, the inflammatory phase involves damaged vessels forming clots and releasing chemokines to recruit inflammatory cells, promoting fibroblast and endothelial cell migration. Second, the proliferative phase activates angiogenesis, delivering nutrients and oxygen vital for healing, while myofibroblasts synthesise ECM and contract granulation tissue. Lastly, scar formation remodels granulation tissue, balancing MMP enzymes and inhibitors, and includes collagen and elastin matrix remodelling[49]. This prolonged phase lasts from several days to years, during which myofibroblasts resolve and decrease through apoptosis.

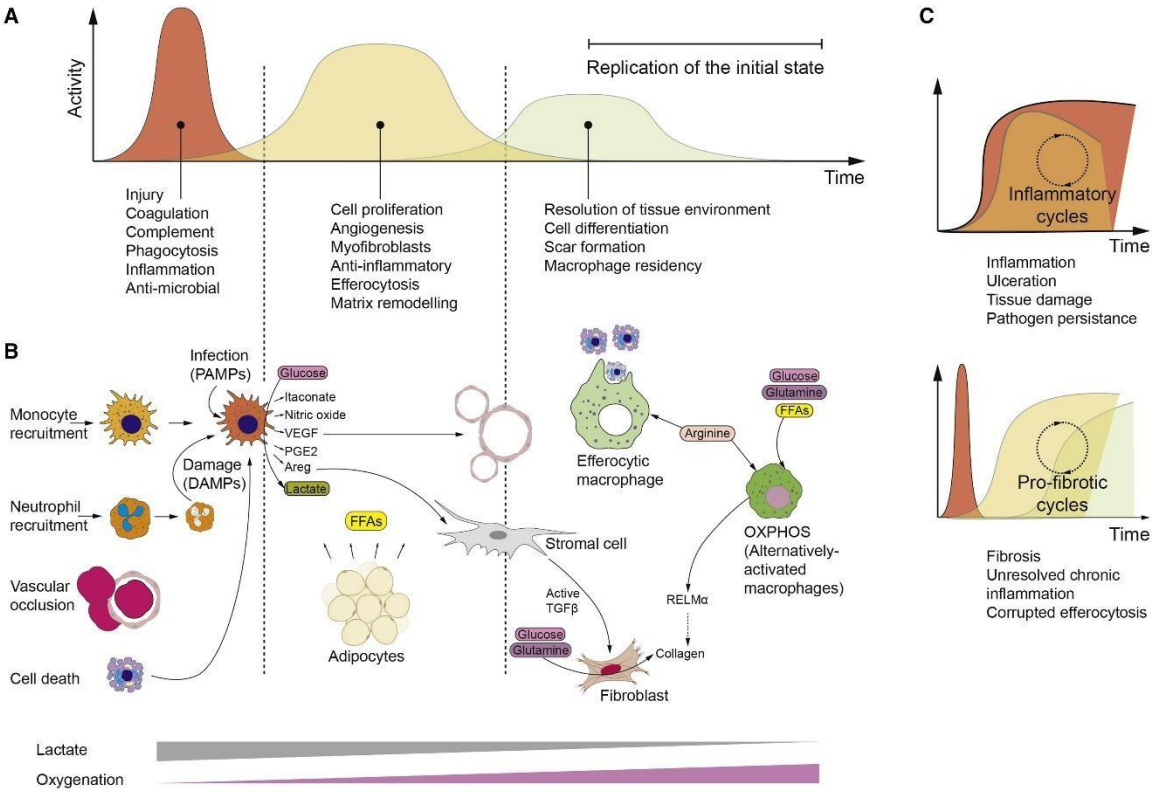

Figure 6: Cellular metabolism and dynamics in wound healing. (A) The temporal patterns of the repair phases show cellular response in wound healing. On the x-axis, time after injury is represented, whereas the yaxis depicts the major events of activity. The three phases are early inflammation (red), intermediate proliferation (yellow), and late-stage resolution and scar formation (green). **(B)** Involved immune and stromal cells in the distinct phases of wound healing. All cells adapt their metabolism in response to changes in nutrient and oxygen availability, supporting tissue repair and the production of growth factors. **(C)** Schematics of dysregulated wound healing responses disrupting physiological repair dynamics. Upper panel: persistent inflammation leads to tissue damage, as seen in chronic infections or cancer. Lower panel: failure in resolution results in uncontrolled fibrosis. The figure is adapted from Inflammation and metabolism in tissue repair and regeneration by S. Eming, Science, 2017[50].

Abbreviations: PAMP, pathogen recognition receptor; DAMP, damage-associated molecular pattern; VEGF, vascular endothelial growth factor; TGFβ, transforming growth factor; FFAs, free fatty acids; PGE2, prostaglandin E2; Areg, amphiregulin; Relmα, resistin-like molecule.

3.4 Fibrosis

Chronic fibrosis is a pathological response akin to wound healing but fails to resolve, leading to the accumulation of ECM proteins that disrupt tissue organisation and impair organ function. Common causes include mechanical injuries, chronic exposures to chemicals or toxins, persistent infections, genetic disorders or chronic autoimmune diseases. Fibrosis is a central feature of rheumatological diseases such as Systemic Sclerosis (SSc), rheumatoid arthritis, or Lupus erythematosus[51]. Mitochondrial dysfunction, alimenting chronic inflammation, has been hypothesised to be an important underlying cause in fibrotic diseases, such as SSc interstitial lung disease (SSc-ILD)[52]. Current research examines the cellular origins and mediators that activate or eliminate myofibroblasts, along with elements driving inflammation. Understanding these factors is important for antifibrotic treatment targets, as fibrosis of organs deeply affects patient outcomes and is a potent contributor to worldwide morbidity and mortality[53].

Although fibrosis mechanisms remain incompletely understood, it is widely accepted that tissue injury triggers an inflammatory response with activation of local and infiltrating immune cells[54]. These cells secrete cytokines and chemokines that stimulate mesenchymal and other cells to differentiate into myofibroblasts or matrix-producing cells, driving fibrogenesis. Multiple progenitor types contribute to this pool, including epithelial, mesothelial, and endothelial cells (via epithelial-, mesothelial-, and endothelial-to-mesenchymal transitions), tissue-resident fibroblasts, fibrocytes, pericytes, and other mesenchymal cells, with their relevance depending on organ and inflammation type[55]. However, not all cells solely promote fibrosis. Macrophages, perhaps the most fundamental source of TGF-β secretion, also phagocytose pro-fibrogenic cells and activate MMPs[56]. Finally, the array of inflammatory cells transforms the matrix architecture and plays important immunomodulation roles, resulting in a microenvironment that progressively favours the development of chronic inflammation and cancer[57].

The relevance of the pro-fibrotic environment becomes clear in autoimmune diseases like SSc, characterised by a type 2 immune response with elevated cytokines, T-cells, and activated macrophages that promote fibrosis[58]. While primarily serving as a defence to remove noxious compounds or pathogens, persistent inflammation causes tissue damage and cell death, releasing more pro-fibrotic mediators, if the underlying cause persists or when repair processes become dysregulated. Besides, non-peptide mediators, such as excessive reactive oxygen species (ROS) in SSc, can induce myofibroblast differentiation and heighten inflammatory responses[59,60]. However, interleukins from both the innate and adaptive immune systems, such as IL-1b and IL-6, can also exert protective functions and attenuate fibrosis development[61], as seen in the liver and skin[62,63].

TGF-β is considered the critical regulator of wound healing and fibrosis, involved in physiological and pathological inflammatory responses (Figure 7). TGF-β is secreted by platelets, macrophages, lymphocytes, or fibroblasts, and functions in an autocrine and paracrine fashion, ultimately stimulating ECM production in fibroblasts[64]. Integrin-mediated reservoir degradation, increasing TGF-β levels, can add to aberrant TGF-signalling[65]. Thus, not only TGF-β secretion but also abnormal activation is involved in fibrosis.

The role of this pluripotent growth factor is highlighted in fibroblast overexpression of the TGFβ receptor type I, further increasing SSc's clinical and biochemical hallmarks[66]. In these autoimmune diseases, this effector cytokine is known to be a primary driver of fibrosis and to correlate with disease severity[64]. Conversely, inhibition of TGF-β prevents skin fibrosis and is effective against established Bleomycin-induced dermal fibrosis in mouse models[67]. However, genetic loss of TGF-β in mice results in massive systemic inflammation, tissue necrosis, severe wasting syndromes, and increased cancer risk, additionally suggesting a role as a potent regulator of excessive inflammation[68,69,70].

Therefore, modulating TGF-β, potentially uncovering life-threatening risks, requires tight regulation. Drugs like Pirfenidone, which target TGF-β, have been explored for idiopathic pulmonary fibrosis (IPF) and have shown manageable side effects in clinical trials[71]. Additionally, other downstream targets within the TGF-β pathway, such as Fibroblast Growth Factor III (FGFRIII) or PDGFR, revealed a therapeutic potential with Nintedanib (Figure 8), although further clinical studies are necessary to fully understand their efficacy[72].

Fibrosis, once deemed irreversible, is partly reversible depending on the disease stage. For example, liver cirrhosis shows histological improvement after treating hepatitis B, C, or schistosomiasis[73]. In chronic kidney disease, improvements have been noted in type 1 diabetes patients post-pancreas transplantation[74]. These findings have spurred research into experimental mouse models to identify targets for fibrosis regression, focusing on removing the underlying cause of damage, degrading ECM surplus, and eliminating myofibroblasts. The most effective way is to remove the cause of the injury, as shown in the antiviral treatment of hepatitis. When targeted treatments are unavailable or the cause is unknown, directly modulating the ECM becomes a strong alternative. Popular targets for ECM modulation are MMPs, a group of endopeptidases produced by several types of cells that can directly degrade fibrotic matrix, or LOX (3.2.4), which enhances collagen contraction. For example, UVA-1 irradiation used in phototherapy increases MMP expression, supporting the degradation of collagen[75]. However, direct or indirect activation of MMP in mouse models does not necessarily result in improved fibrosis and can sometimes worsen it[76]. LOXL2 blockage successfully attenuates fibrosis in the heart, lung, and liver in mice, whereas clinical trials using the monoclonal antibody Simtuzumab (LOXL2-inhibitor) did not improve survival in IPF patients so far[77].

Lastly, an essential target to sustain the resolution of fibrosis is the elimination of myofibroblasts themselves. This can be achieved by modulating cell fate through approaches such as inducing apoptosis, senescence, dedifferentiation, or reprogramming. For example, the IκB kinase inhibitor Sulfasalazine or the proteasome inhibitor Bortezomib facilitate myofibroblast apoptosis and support attenuation of liver cirrhosis[78,79]. Mice with a senescencedefective ccn1 mutant, a matricellular protein that is dynamically expressed in wound sites, showed increased fibrosis, which was reversed by topical CCN1 application, underscoring the role of senescent cells in tissue repair[80]. Dedifferentiation, where myofibroblasts revert to a progenitor-like phenotype, can be induced by factors like FGF 1 and 2 or through reprogramming of cell lineages[81]. Specifically, Plikus et al. investigated the successful conversion of dermal myofibroblasts in wounds into adipocytes via administration of the bone morphogenetic protein, mimicking an embryonic pathway[82].

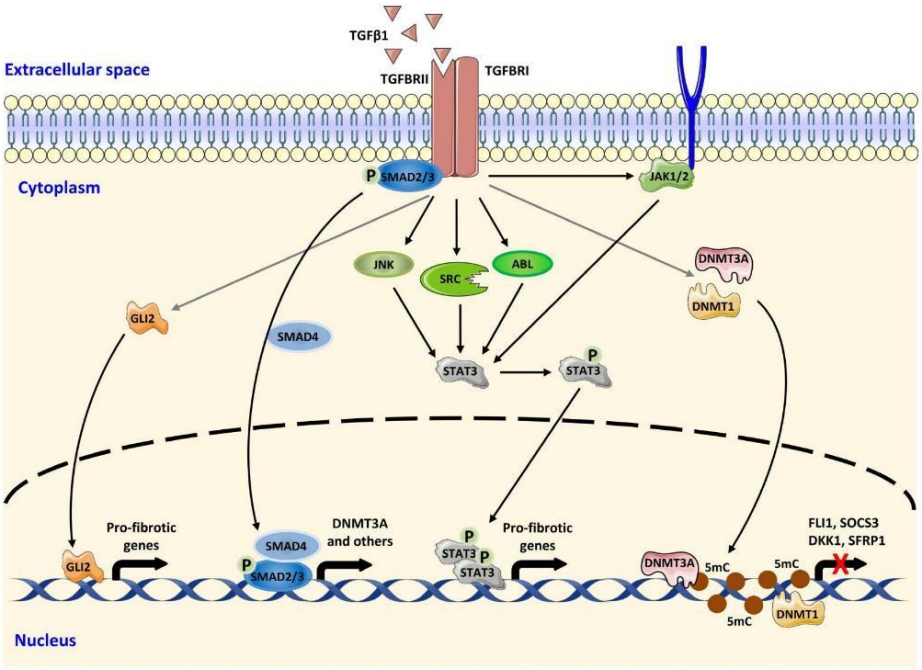

Figure 7: TGF-β signalling and interactions with profibrotic pathways. In its active form, TGF-β1 (one of the three isoforms of TGF-β) binds to the hetero-tetrameric receptor TGF-βRII and dimerises with TGF-βRI, leading to phosphorylation. TGF-β can then activate the canonical SMAD or non-canonical pathways, such as MAPKs or PI3K/AKT, although SMAD is the most studied so far. The TGF-βRI-III receptor complexes act as serine-threonine kinases, facilitating the recruitment and phosphorylation of receptor-regulated SMAD proteins (SMAD 2 and 3). Together with SMAD 4, this complex induces gene expression in the nucleus[83].
Adapted from Cellular and molecular mechanisms in fibrosis by Dees et al., in Experimental Dermatology, 2021[72].

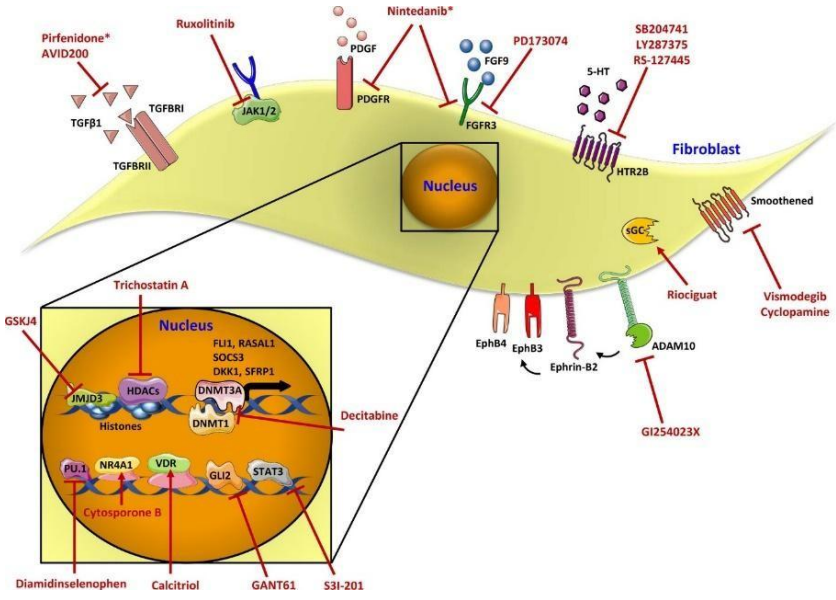

Figure 8: Representation of potential targets for antifibrotic treatment. Arrows and "┬" indicate activation and inhibition, respectively. Asterisks indicate that the medication is approved for clinical use in SSc-associated lung disease and IPF. This scheme is adapted from Cellular and molecular mechanisms in fibrosis by Dees et al., in Experimental Dermatology, 2021.

3.5 Mitochondria in skin homeostasis

3.5.1 Skin relies on mitochondria for metabolism, energy supply and homeostasis

The epidermis is a high-turnover organ that relies on the supply of ATP from OxPhos for maintenance[84]. However, this does not apply to all cells. A disrupted electron transport chain (ETC) through Mitochondrial transcription factor A (TFAM) ablation in basal layer located stem cells does not necessarily result in impaired epidermal proliferation and differentiation in neonatal mice, provided mitochondrial dynamics remain intact[85]. Conversely, in a related model involving TFAM KO mice, observable impairments in skin barrier function occur as the mice age, likely from reduced levels of Reactive Oxygen Species (ROS)[86].

Dermal fibroblasts are also energy-demanding and require functional mitochondrial metabolism to ensure viability, proliferation or ECM synthesis[87,88]. The ability of fibroblasts to migrate, particularly in dense collagen matrices, also depends on adequate ATP levels[89]. Dysfunctional mitochondria in fibroblasts can be involved in the onset of many autoimmune diseases. For instance, rising evidence shows that oxidative stress can drive the fibrotic phenotype of Systemic Sclerosis (SSc) fibroblasts[90,91].

3.6 Skin ageing in the context of dysfunctional mitochondria

3.6.1 Definition and Aetiology

Skin ageing is a complex process with no universal definition. However, it is commonly associated with progressive atrophy of the epidermis and dermis, loss of collagen fibres, pigmentation changes, increased inflammatory processes, leading to a loss of essential functions. We further distinguish intrinsic and extrinsic ageing. The former is also known as the natural chronological ageing process, which involves inevitable cell degeneration through nuclear and mtDNA damage, epigenetic influences, immune deregulation, and hereditary factors. Extrinsic skin ageing, primarily associated with photoageing, refers to the impact of external factors such as lifestyle, smoking, alcohol consumption, UV exposure, and the environment[92].

Both intrinsic and extrinsic ageing are associated with gradual impairment of mitochondrial function and oxidative stress. This concept was initially introduced in the "Free Radical Theory of Ageing" by Harman in 1956, which posits that accumulated mtDNA mutations disrupt metabolism, increasing ROS production in a vicious cycle[93]. This theory initially highlighted the role of mtDNA damage in ageing tissues but has since been revised. While aged dermal fibroblasts show elevated ROS levels[94], it remains unclear whether this reflects mitochondrial dysfunction or broader cellular changes. For instance, increased ROS may result from enhanced leakage from dysfunctional mitochondria or weakened antioxidative systems, which reduce ROS elimination[36]. Furthermore, the mitochondrial genome is more equipped against

oxidative stress than previously assumed (e.g. through repair enzymes such as mtDNA polymerase)[95,96]. Additionally, the origin of mtDNA mutations is numerous, allowing for other sources beyond ROS, as for example replicative errors in mtDNA, as revealed in nextgeneration sequencing studies[97,98].

Rather than a gradual accumulation of mutations via repeated oxidative damage, single-cell studies suggest that clonal expansion of cells with high mutational loads may better explain the impact of mtDNA damage in ageing[99]. Dysfunctional cells, when reaching a critical threshold, can compromise the function of entire organs, particularly in metabolically active tissues like the brain, heart, and muscle[100]. Thus, the relationship between oxidative stress, mtDNA mutations, and ageing is more complex than originally proposed, and the extent to which ROS production accounts for mtDNA mutations and drives ageing remains controversial. In the context of skin, ageing is consistently linked to reduced mitochondrial function, contributing to premature ageing phenotypes[14,101]. Specifically, mtDNA mutations in the skin correlate with higher age and UV exposure, contributing to both chronological and photoageing, respectively[87,95]. These mutations have therefore become widely recognised as a biomarker of skin ageing[102,103]. The most frequently found mutation is the so-called “common deletion”, exhibiting the highest level of heteroplasmy in sun-exposed areas and, therefore, more associated with photoageing[104,105]. Other mutations, such as the T414G point mutation in the control region, also accumulate in ageing dermal fibroblasts[20]. Thus, different patterns of mtDNA aberrations contribute to ageing processes, which will be briefly introduced in the following sections.

3.6.2 Photoageing

Photoageing is induced by exposure to UVA (320-400 nm), UVB (280-320 nm), and nearinfrared IRA (>700 nm), and is characterised by epidermal thinning, resulting in skin dryness and wrinkles. UVA and IRA, which reach the dermis, induce mtDNA deletions, and increase chronic oxidative stress, impair collagen metabolism and induce neovascularisation, thus prominent features of photoageing[87].

The “common” 4977 bp deletion (CD), induced by oxidative stress and environmental factors, has been in the spotlight in previous years due to its strong association with UV exposure in skin ageing[104]. Kaneko et al. observed a significant correlation between high levels of CD in UV-exposed (German) versus lower levels in sun-protected (Japanese) women. Notably, CD was less frequently detected in Caucasian patients with extrinsic ageing hallmarks, putatively due to a selective process that attenuates the accumulation of damaged mtDNA. Fibroblasts derived from Kearns-Sayre-Syndrome patients, an inheritable genetic disease with

considerable accumulation of mtDNA deletions, show increased ROS levels and Lysil oxidase activity (LOX) (3.2.4), similar to photoaged skin[106].

Although the extent of ROS contribution to mtDNA deletions remains uncertain, UV-induced mtDNA deletions cause insufficient energy production and retrograde mitochondrial signalling pathways that convey functional and structural changes in the skin, while ROS signalling independently contributes to photoageing phenotypes (e.g. through enhanced MMPs activation)[87,101].

3.6.3 Chronological ageing

In chronological ageing, defects of repair mechanisms for nuclear and mitochondrial DNA become increasingly likely over time, leading to mutations and accompanied by elevated ROS production and loss of function, resulting in various skin abnormalities. Compared to photoageing, this type exhibits a leathery appearance with deeper wrinkles and uneven pigmentation. MtDNA aberrations drive skin ageing in a mouse model with inducible mtDNA depletion via a dominant-negative polymerase-γ mutation. Singh et al. described ageing symptoms, such as wrinkles, inflammation and hair loss, which were reversed by restoring mtDNA after stopping mutant expression[107]. Similar inflammation was observed in keratinocytes expressing the K320E-Twinkle mutation, suggesting a link between subclinical inflammation and mtDNA depletion in the epidermis[84]. In human fibroblasts, an age-dependent decrease of complex II has been observed in senescent populations. Senescence is an important contributor to chronological ageing in skin cells, displaying a pro-inflammatory phenotype called Senescence-Associated-Secretory-Phenotype (SASP). There is evidence that chronic, low-grade senescence-associated inflammation, known as “Inflammageing”, promotes ageing[27,108].

Photoageing and chronological ageing have different yet partly common backgrounds and are deeply intertwined. Both are subjected to an accumulation of mtDNA deletions, oxidative stress, high levels of ROS, and inflammation in the epidermal and dermal layers.

3.7 Function of mitochondria in eucaryotic cells

Mitochondria are elementary in eucaryotic cells and have a unique organisation responsible many functions. The outer and inner mitochondrial membrane (OMM and IMM, respectively) form two compartments: the mitochondrial matrix and the intermembrane space (Figure 9). The OMM is highly permeable to solutes, transporting many metabolites. Additionally, the proteins in OMM are crucial for mitochondrial quality control, dynamics, and communication with other cellular organelles. The IMM has a restricted permeability and is responsible for harbouring proteins for ATP production. This membrane forms deep invaginations, the socalled cristae, conferring a large surface enabling the establishment of a chemiosmotic force, and

enclosing the mitochondrial matrix. This space contains mtDNA, ribosomes, enzymes such as the tricarboxylic acid and ß-oxidation, and produces ATP[109]. Mitochondrial quantity depends on tissue and cell type (approximately 800 in hepatocytes, up to 100.000 in oocytes[110]) and on cellular needs[111]. During their life cycle, mitochondria perpetually undergo fusion, fission and motility, a process referred to as mitochondrial dynamics, allowing mitochondria to adapt to various stressors and meet the cell's demands by adjusting their number, size, and positioning to maintain cellular homeostasis[112].

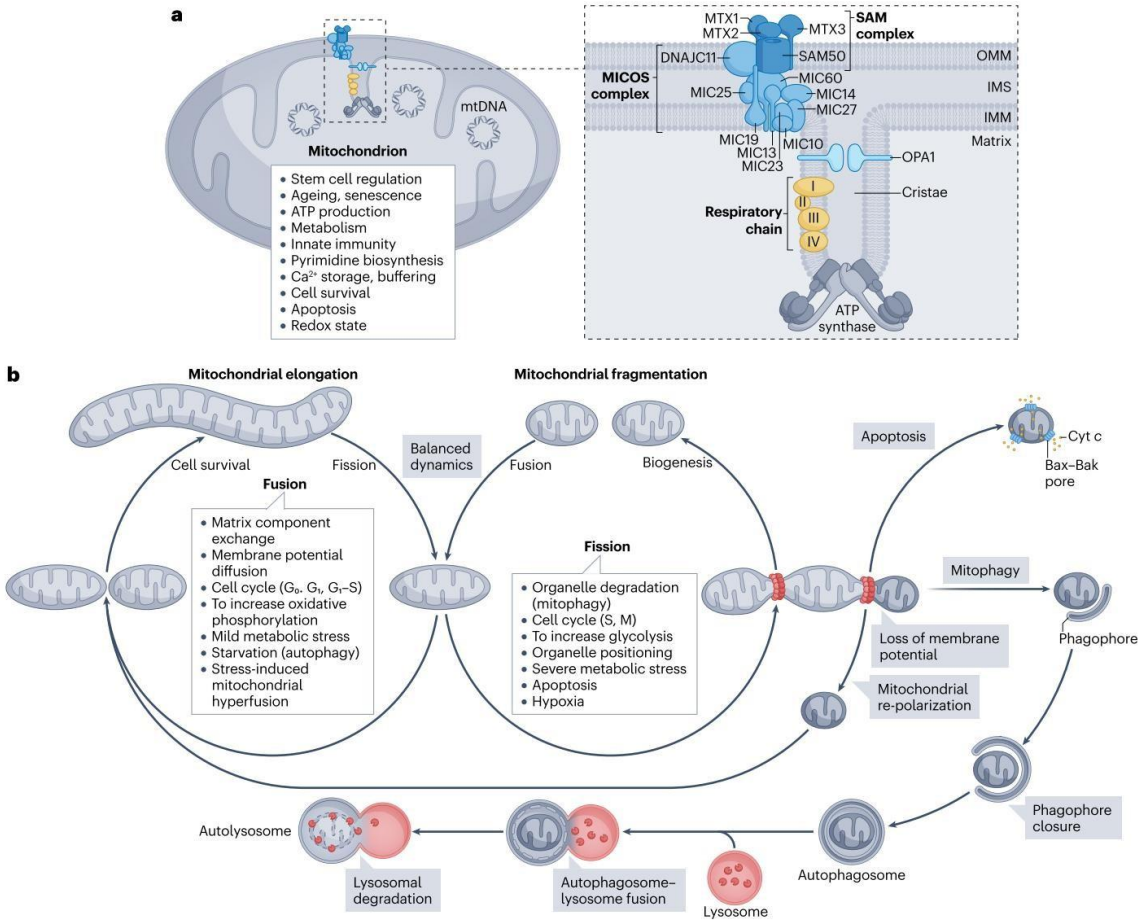

Figure 9: Mitochondrial structure and life cycle. **A.** Mitochondria regulate not only energy production but also numerous cell functions, as listed. Key structural components like the outer/inner mitochondrial membrane and the mitochondrial intermembrane space bridging complex maintain cristae architecture and membrane contact. **B.** Mitochondria undergo dynamic cycles of fission and fusion in response to metabolic demands and stress. Elongation protects functional mitochondria against cell death and mild stress, while fragmentation typically occurs during mitosis and severe stress responses to ensure adequate distribution of mitochondria to daughter cells. Stressors can include apoptosis or mitophagy, where small dysfunctional mitochondria are degraded within autophagosomes. This figure was adapted from "Molecular mechanisms of mitochondrial dynamics" by Tabara et al., in Nature reviews molecular biology, 2025[112].

Abbreviations: BAK: Bcl-2 Antagonist Killer; Cyt c: Cytochrome c; DNAJC11: DnaJ Heat Shock Protein Family (Hsp40) Member C11; IMM: Inner Mitochondrial Membrane; IMS: Intermembrane Space; MDCs: MitochondrialDerived Compartments; MICOS: Mitochondrial Contact Site and Cristae Organizing System; Mitochondrial
Intermembrane Space Bridging; mtDNA: Mitochondrial DNA; MTX1–MTX3: Metaxins 1 to 3; OMM: Outer Mitochondrial Membrane; OPA1: Optic Atrophy 1; SAM50: Sorting and Assembly Machinery Component 50 Homologue.

3.7.1 Quality control system

Mitochondria rely on a finely tuned quality control system, utilising mitochondrial fragmentation and removal of dysfunctional parts (Figure 9)[112]. This involves mechanisms such as fusion and fission events, mitophagy, and mitochondrial biogenesis[113]. Fission is generally coupled to the cell cycle and relocates smaller mitochondrial units inside a cell based on energetic demand and preservation of mitochondrial integrity, while dysfunctional fragments are degraded in autophagosomes. Fusion is the subsequent process, attaching the fragmented pieces into a connected mitochondrial network[113]. Mitochondrial biogenesis is a process to meet increased energy demands and to replace damaged mitochondria. Overall, those dynamics in mitochondrial architecture play an essential role in cell homeostasis and are involved in metabolic disorder, tissue degeneration and disease.

In the context of ageing, particularly in skin, this dynamic balance is progressively disrupted. Ageing fibroblasts show increased mitochondrial fragmentation under stress, reduced biogenesis, and impaired fusion-fission dynamics, marked by lower ATP production and higher ROS[114,115]. This dysfunction can trigger premature senescence and contribute to hallmark features of aged skin[116]. Additionally, external stressors like UV irradiation exacerbate mitochondrial damage by inducing mtDNA deletions and promoting further fragmentation and accelerating photoageing by hindering functional mtDNA exchange and defective genome clearance[113].

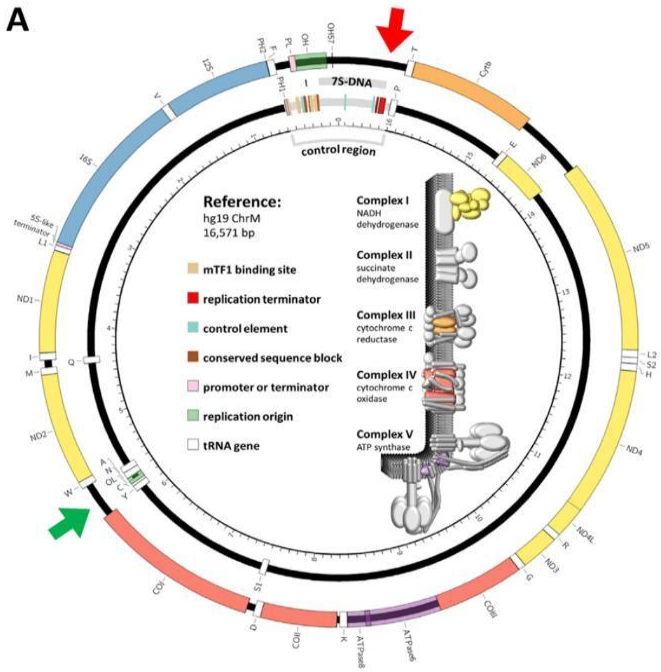

Figure 10: mtDNA reference map. The human mtDNA genome encodes 13 OxPhos proteins (in respective colours), while nucDNA encodes the remaining 80% (in grey).

3.7.2 Mitochondrial DNA

The maternally inherited mtDNA is a circular double-stranded genome of approximately 16.5 kb located in the mitochondrial matrix. It comprises an inner light (L) strand and an outer heavy (H) strand, and encodes 37 genes in humans: 22 tRNAs, 2 rRNAs, and 13 protein subunits of the electron transport chain and ATP synthase (Figure 10). The endosymbiotic theory suggests that mitochondria were once independent bacteria engulfed by another organism unable to respire, providing an evolutionary advantage. Encoded initially by mtDNA, genes were gradually transferred to nucDNA. Although the 13 proteins from mtDNA represent only about 1% of the mitochondrial proteome, they are vital for OxPhos, working alongside nuclearencoded genes[117].

MtDNA is more prone to damage than nucDNA due to limited repair mechanisms DNA[118] and a 10-fold higher mutation rate. Notably, the physiological free radicals produced during mitochondrial respiration impact mtDNA due to its location near the RC. However, cells can tolerate high levels of damaged mtDNA due to the presence of abundant WT mtDNA; mitochondrial DNA can coexist in both mutated and non-mutated forms, known as heteroplasmy, enabling the cell to tolerate high levels of damaged mtDNA. In contrast, homoplasmy refers to a state where only one type of mtDNA is present. Diseases can arise when heteroplasmy surpasses a tissue-specific threshold[119] .

3.7.3 mtDNA replication

mtDNA replication is orchestrated by a replisome, which includes polymerase-γ (Polγ), a Topoisomerase I, mtDNA single-stranded DNA-binding proteins (mtSSB), and the Twinkle helicase (3.7.4). Peroxisome proliferator-activated receptor gamma coactivator 1-alpha (PCG1a) controls the expression of replication and mitochondrial transcription factors A (TFAM) and B2 (TFB2M) are essential for the transcription apparatus[120]. Among several suggested models, the 'strand-displacement' model is widely accepted. Replication occurs unidirectionally from two origins (Ori), where each L- and H-chain synthesis starts (Figure 11). The H-chain represents approximately two-thirds of the mtDNA and originates from OriH. A stem-loop structure is formed for mitochondrial RNA polymerase (POLRMT) to recognise OriL, from which the L-strand synthesis occurs in the opposite direction. This results in two complete double-stranded daughter mtDNA molecules. Different models have been described in deletion formation. For instance, replication fork stalling of one strand leads to spurious annealing of mtDNA single-strand regions with direct repeats[9]. This results in a loop excluded from replication, a process called replication-slippage. Another mechanism is copy-choice recombination, in which secondary structures can be formed by the exposed single-stranded regions displaying direct repeats. If these structures persist, this DNA sequence is deleted during the second replication[118].

Compared to nucDNA, mtDNA repair mechanisms are poorly characterised, though some processes have been identified. The best described mechanism is base excision repair to counteract oxidised bases, while nucleotide excision and mismatch repair activities are still objects of ongoing research. During this process, mtDNA is mostly degraded, triggering replication to reconstitute the genomic pool[118]. Multiple techniques monitor mtDNA replication. For instance, Falkenberg et al. reconstituted a functional mitochondrial replisome *in vitro*, using human recombinant proteins and adding artificial DNA templates and labelled dNTPds, allowing visualisation of replicative steps through gel electrophoresis. *In vivo*, mtDNA replication can be tracked using Single Molecule Analysis of Replicating DNA (SMARD), which involves the insertion of labelled nucleosides such as Thymidine analogues, allowing visualisation of nascent DNA chains by immunofluorescence. A classic and widely available approach to quantify mtDNA depletion is the quantification of the relative mtDNA to nucDNA copy number using qPCR[121].

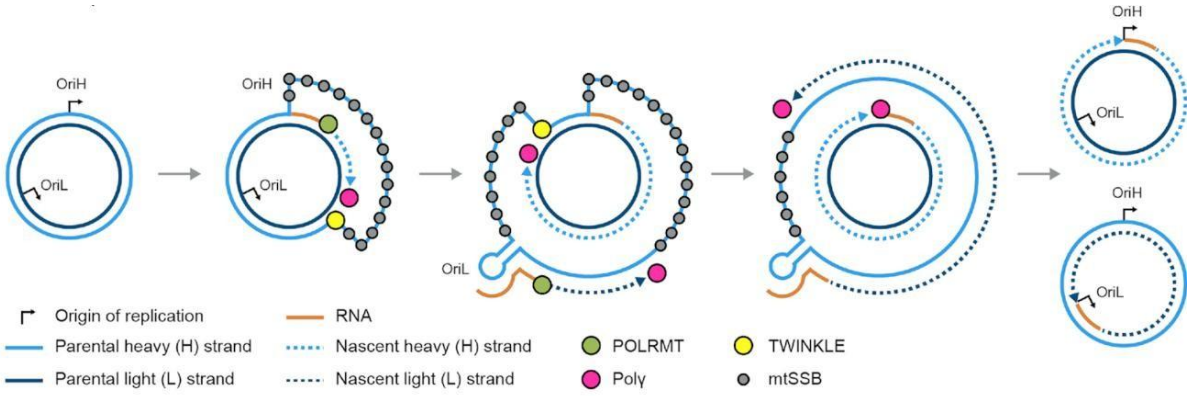

Figure 11: Representation of the strand-displacement model for mtDNA replication. Two replications occur for the heavy (H) and light (L) strands. The associated Origins (Ori) are OriH and OriL, respectively. Replication initiates at OriH, where the mitochondrial RNA polymerase (POLRMT) synthesises short RNA sequences that prime DNA synthesis by DNA polymerase gamma (Polγ). The Twinkle helicase advances ahead of Polγ, unwinding the DNA in an ATP-dependent manner. The exposed parental H-strand is stabilised by mitochondrial single-stranded DNA-binding protein (mtSSB) to prevent erroneous replication events. When the replication machinery reaches OriL, a single-stranded stem-loop structure forms, which blocks mtSSB binding. This structure is recognised by POLRMT, which synthesises a short RNA primer at the OriL site, initiating L-strand synthesis. Polγ then replaces POLRMT, allowing the unidirectional and continuous replication of both nascent strands, ultimately resulting in two complete double-stranded mtDNA molecules. Adapted from Mechanisms of replication and repair in mitochondrial DNA deletion formation, by Gabriele A Fontana et al., in Nucleic Acids Research, in 2020.

3.7.4 Twinkle

Twinkle is a hexameric helicase essential for mtDNA replication and copy number regulation[120,122]. Twinkle KO mice models show severely depleted mtDNA, while overexpression increases mtDNA copy number[122,123]. This ring-shaped hexamer belongs to the DnaB family and is similar to the bacteriophage T7 gene 4 protein helicase, the latter commonly used as a model to study Twinkle helicase and human mitochondrial replication systems[124].

Upon mtDNA replication, Twinkle catalyses 5′ to 3′ NTP-dependent unwinding of the mtDNA duplex. Heptameric conformation may occur to support the stability and functionality of this

process (Figure 12)[125]. Twinkle mutations can disrupt oligomerization, affecting the helicase's flexibility and dynamics, which impairs mtDNA loading and unwinding.

Twinkle mutations are correlated to more than 30 diseases, where patients display mtDNA deletions and depletion, leading to OxPhos deficiency and neuromuscular symptoms. This molecular background underlies the development of autosomal dominant progressive external ophthalmoplegia (adPEO) and rarely in sensory ataxic neuropathy with dysarthria and ophthalmoplegia (SANDO) syndrome[10,126]. adPEO a disease characterised by progressive myopathy, starting in the extra-ocular muscles, along with general weakness and neurological symptoms like parkinsonism or depression. A common trait is the accumulation of mtDNA deletions in post-mitotic tissues, which also correlates with disease progression, precisely in the brain, skeletal muscle, and heart. Targeting Twinkle is ideal to investigate the effect of defective mtDNA replication machinery, by inducing the accumulation of mtDNA deletions in post-mitotic tissue and mtDNA depletion in rapidly replicating cells[17,84].

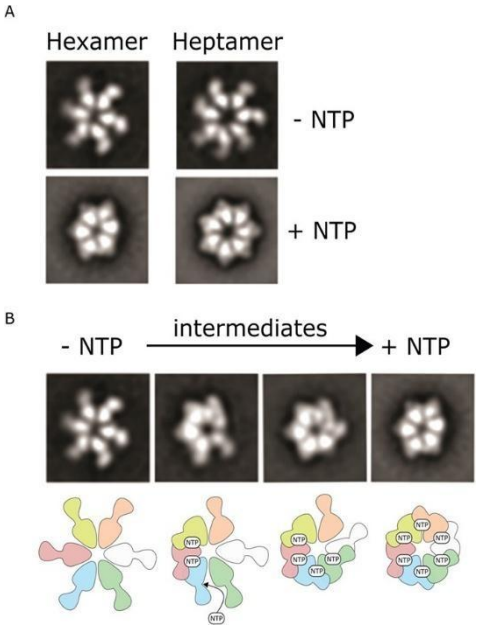

Figure 12: Wildtype Twinkle helicase structure and conformational changes. (A) The twinkle helicase forms hexameric and heptameric oligomers. The enzyme forms a flexible star-like conformation and is compact in the absence and presence of nucleotide triphosphate (NTP). **(B)** Scheme representation of sequential primase domain folding. Upon NTP hydrolysis, the helicase domains rotate about each other, generating the mechanical force to secure DNA unwinding. All pictures stem from single-particle negative staining electron micrography. The figure is adapted from Structural basis for adPEO-causing mutations in the mitochondrial TWINKLE helicase by Peter et al., in Human Molecular Genetics in 2019.

3.8 Experimental design

To explore the effect of accumulating mtDNA deletions *in vivo*, we induced the Twinkle mutation via Tamoxifen feeding in adult mice and collected skin samples. These were either used for fibroblast isolation for cell culture purposes or whole skin extraction, with subsequent use such as histological analysis or dermal protein and DNA/RNA isolation. To investigate mtDNA

depletion *in vitro*, we isolated fibroblasts from newborns and activated the Twinkle mutation with 4-Hydroxy-Tamoxifen treatment. We first aimed to investigate the effect of mtDNA depletion in Twinkle^{FIBRO} fibroblasts *in vitro* by assessing extended mitochondrial parameters and fibroblast function. We then evaluated the Twinkle^{FIBRO} mice phenotype *in vivo* in the steady state and after fibrosis induction, simultaneously accelerating mtDNA deletion accumulation and inducing a chronic inflammatory response, potentially altered upon mtDNA mutation accumulation. After observing no imminent phenotype in the steady state but attenuated fibrosis in Twinkle^{FIBRO} mice, we further investigated fibroblast functions, including proliferation, apoptosis, senescence, autophagy and differentiation.

3.9 Aims of this study

Overall, this study explores the role of mtDNA deletions in skin fibroblasts and in dermal fibrosis. Specifically, we address the following questions:

- How do mtDNA indels affect mitochondrial function and mtDNA integrity in fibroblasts *in vitro*?
- What are the effects of specific mtDNA mutations on the respiratory chain in Twinkle^{FIBRO} fibroblasts *in vitro* and *in vivo,* in both unchallenged and pathologic conditions?
- How do mtDNA deletions affect mitochondrial function in Twinkle^{FIBRO} skin *in vivo,* particularly in the context of fibrosis?
- How is fibrosis development affected in Twinkle^{FIBRO} mice?
- How do cellular functions, such as proliferation, apoptosis, senescence, autophagy/mitophagy and differentiation of fibroblasts with gradually accumulating mtDNA deletions, influence the fibrotic development in Twinkle^{FIBRO} mice?

  What are the novel findings on the potential impact of small-scale mtDNA damage on skin health?

4. Materials and Methods

4.1 Animals

All animal studies were approved by the University of Cologne's animal care committee and local government authorities (Bezirksregierung Köln; Landesamt für Natur, Umwelt und Verbraucherschutz (LANUV, Recklinghausen, breeding Az 2016.A410 and experimental setup Az 2019.A101)).

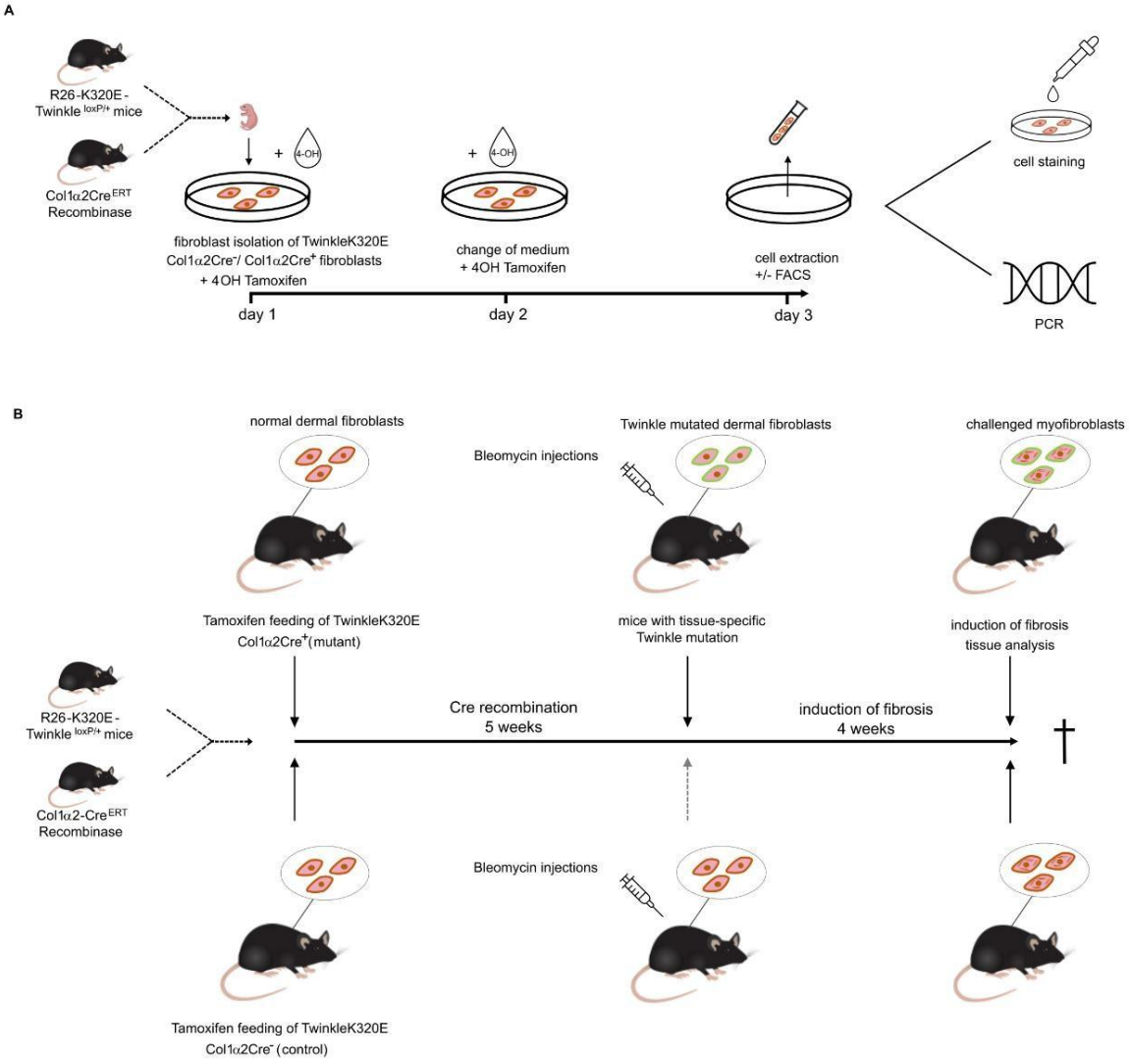

Figure 13: Transgenic K320E-Twinkle/Col-Cre mouse model. (A) Cell harvesting and treatment: fibroblasts were isolated from WT or Twinkle^{FIBRO} mice. These fibroblasts were treated with 4-Hydroxy-Tamoxifen for 48 hours, with the medium replaced after the first 24 hours. As only 30% of the dermal fibroblasts expressed Col1A2CreER$^{+/-}$ after treatment, cell sorting was performed, and only GFP-expressing fibroblasts were collected for subsequent experiments, except for flow cytometry or PCR experiments. **(B)** Mouse Treatment Protocol: Twinkle^{FIBRO} mice, aged 27 to 30 weeks, were fed a diet supplemented with Tamoxifen for 5 weeks. After this period, mice were switched to a regular diet and received repetitive Bleomycin injections for 4 weeks. Following the treatment period, mice were sacrificed, and tissues were harvested for subsequent experiments. The figure was made using Inkscape, and schemes of mice were retrieved from Pixabay on June 19th, 2021.

4.1.1 Generation of K320E-Twinkle^{FIBRO} mice

K320E-Twinkle^{FIBRO} mice were generated by crossing Col1A2CreER$^{+/-}$ mice[127] with R26K320E-Twinkle$^{loxP/+}$ mice (Baris et al., 2015). The COL1A2 gene encodes for the pro-α2 chain, the main component of Collagen type I[47]. This promoter induces the expression of K320E-Twinkle in fibroblasts but not in other type 1 Collagen-producing cells. Thus, Twinkle^{FIBRO} mice express a dominant negative Twinkle Helicase[9] under control of the ColCre^{ERT} recombinase exclusively in dermal fibroblasts, activated by feeding Tamoxifen (400mg per kg diet, Envigo) (Figure 13). Littermates with the genotype R26-K320ETwinkle$^{loxP/+}$/Col1A2CreER$^{-/-}$ were used as controls. The background of all mice is the strain C57BL/6J. The mice were held in our breeding facility (Dezentrales Tierhaltungsnetzwerk der Medizinischen Fakultät, Weyertal, Cologne, Germany), under standard pathogen-free conditions with a variable number of mice, typically ranging from 1 to 4 in cages of the same gender.

4.1.2 Genotyping

Tail tips of mice were lysed in 150 µl of first lysing buffer (2,5M NaOH, 20mM EDTA) for 45 minutes at 96°C in a shaking incubator at 300 rpm. Next, samples were placed on ice for 5 minutes. The samples were vortexed, and the same volume of second lysis buffer (4M TrisHCl, pH 7,6) was added. Tubes were then vortexed again and centrifuged for 1 minute at 1000g at room temperature. The supernatant containing the DNA was used for PCR, and the samples were prepared, as shown in Table 1, using the DreamTaq Green PCR Master Mix (Thermo Fisher Cat.No.: K1081). The used primers were: ROSA KE forward (5'AAAGTCGCTCTGAGTTGTTATC3'), ROSA KE rev (5'GATATGAAGTACTGGGCTCTT3'), Col1A2 forward (5'CGATGTTGAACTTGTTGCTGA3'), Coal1A2 reversed (5'GATTGTCTTGCCCCATTCAT3'). The PCR was run in a Thermocycler (Biometra, Anyltika Jena). PCR products were resolved on a 1,2% agarose gel in 1x TAE (40mM Tris base, 20mM Acetic acid, and 1mM EDTA) buffer (Table 2) containing ethidium bromide (0.8 µg/ml). 1,2 g agarose was added to 100 ml of 1x TAE buffer, and the mixture was heated in a microwave at 800 W until the liquid was clear. By stirring on a magnetic stirrer, the solution was cooled down, and finally, 2,5 µl of ethidium bromide was added. The liquid gel was poured into the gel chamber, and a 12-18 teeth comb was inserted. After 15 minutes, the gel was polymerised. 10 µl of PCR sample and 5 µl of DNA ladder (GeneRuler 100 bp DNA Ladder, ready-to-use, premixed with 6X TriTrack DNA Loading dye, Thermo Fisher, SM0243) were applied, and electrophoresis was performed in 1x TAE buffer at 120V for 1h. PCR products were visualised under UV light (EL Logic 200 Imaging system). All samples from mice containing the K320ETwinkle construct in their genome display two bands (indicating the KE and WT

genotype), while one band in the Col1A2CreER$^{+/-}$ PCR indicates the presence of the Cre Recombinase (Figure 14).

Master Mix	25 µl
Green DreamTaq	12,5 µl
Primer “all in one”	1,0 µl
Water	11,5 µl
DNA	1,25 µl

Table 1: PCR Master Mix for Genotyping of one sample.

50x TAE buffer in deionised water (recipe for 1L)	
Tris	242 g
Na-EDTA x $2H_2O$	18,61 g
glacial acetic acid	57,1 ml
pH = 8.3	

Table 2: Buffer solution containing Tris base, Acetic acid and EDTA, used for agarose gel electrophoresis.

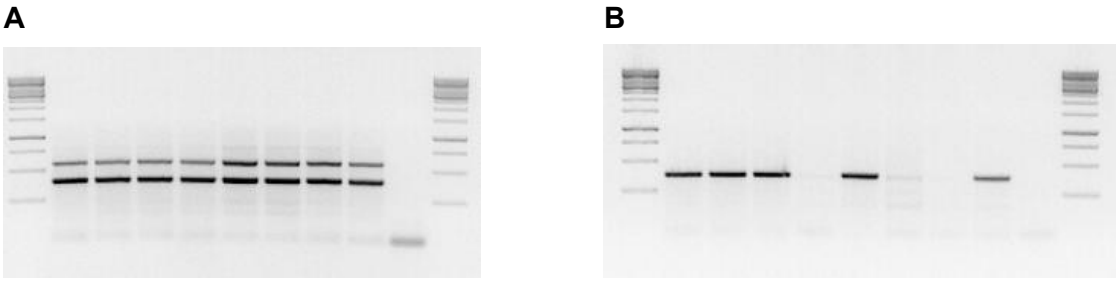

Figure 14: Gel electrophoresis for determining mouse genotypes. (A) PCR products indicating K320E and wt gene and **(B)** Col1α2-recombinase, respectively. Samples that display or lack a band in B represent mutants and controls, respectively.

4.2 Fibrosis induction

Fibrosis was induced by intradermal injections of Bleomycin solution (Bleomedac) 5 times a week for 4 weeks (Figure 13). Bleomycin is a cytotoxic agent that induces inflammation and fibrosis with the production of pro-inflammatory and pro-fibrotic cytokines as well as Collagen 1 and activation of the a-SMA gene[51,128]. The mice received 100 µg Bleomycin (1mg/ml in NaCl) alternating between the lower left and right corners of the predefined injection area, which increased the resulting fibrotic surface. Vehicle control mice received NaCl solution only.

The Bleomycin experiment involved isolating the mice to protect the fibrotic area from being inadvertently affected by scratching by peer mice. For a similar reason, the injections were placed at the neck, as this is inaccessible to the mouse itself. The neck was shaved regularly, facilitating injection into the dermis. The control of correct intradermal injection implied a macroscopically visible bulla

For anaesthesia animals were positioned in a box with a continuous supply of isoflurane

(initiation 4,5% in 2L/min O2 air pressure at 600ml/min) and fell asleep within 2-3 min. Then, anaesthesia was continued via an inhalation mask to ensure the constant flow of the narcotic gas (maintenance at 2,5% Isoflurane and 1,5 L/min O2 and 400ml/min air pressure) (Figure 15 A). Dexpanthenol (Bepanthen®) was applied on the eyes to protect from drying.
24h after the last Bleomycin injection, mice were killed by carbon dioxide inhalation, as cervical dislocation would harm the neck tissue and influence histology results. Hair was removed and the skin was excised and separated, as shown in Figure 15 B.

4.3 Protein isolation

The region shown in Figure 15 B was cut for protein isolation, and the skin was peeled off with scalpels and scissors. After removing at under the dermis, the skin was spread on a 0,8% trypsin solution (2,5% Trypsin, Gibco) in dPBS (Dulbecco's Phosphate Buffered Saline, Gibco) solution at 37°C for 1-2 hours. After incubation, the epidermis and dermis can be carefully separated and stored. From here on, the protocol is the same as for protein isolation of cells. To extract proteins, 100-300 µl RIPA (Radioimmunoprecipitation assay buffer) (Roche) lysis was applied to the homogenised tissue or cells. After incubation on ice for 1h and 15 minutes, the lysate was centrifuged at 14.000 rpm at 4°C for 10 minutes. The supernatant was transferred, protein concentration was quantified by the Pierce BCA Protein Assay Kit (Thermo Fisher) and stored at -80°C.

A **B**

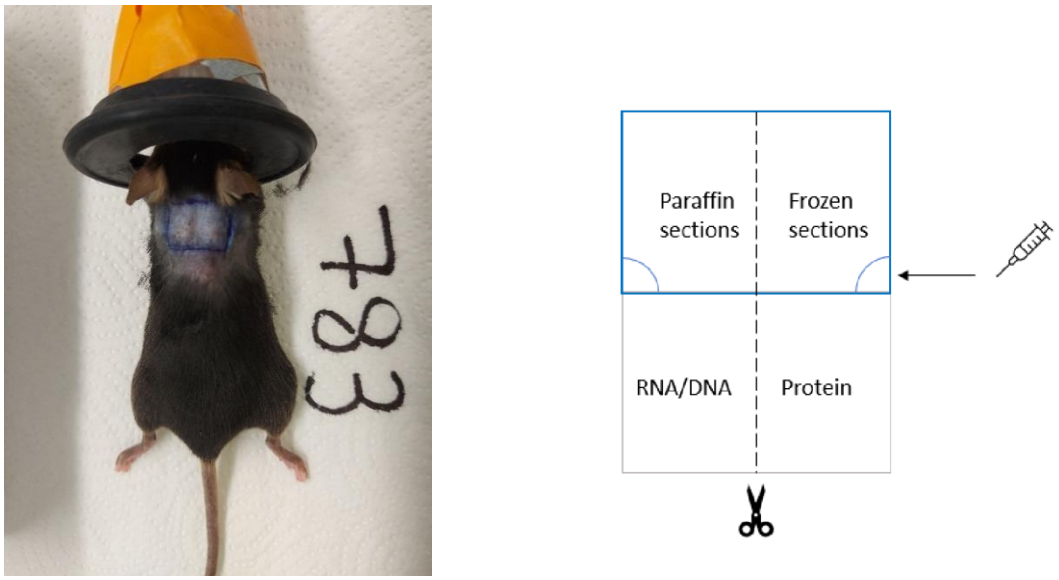

Figure 15: Fibrosis induction in Twinkle^{FIBRO} mice. (A) Mouse under Isoflurane anaesthesia during Bleomycin injection. **(B)** Sampling of the skin. The blue square refers to the marked region on the neck of the mouse, whereas the dotted lines show where the skin was further cut. The corners refer to the location of the daily injections.

4.4 RNA Isolation

For RNA isolation tissue of the region shown in Figure 4 B was used. 100 µl of BCP (1-bromo3-chloro-propane) per 1 ml of Trizol was added to each sample and mixed vigorously for 15 seconds, followed by an incubation of 5-10 minutes at room temperature. Samples were centrifuged at 12.000 g at 4°C for 15 minutes. The upper clear aqueous phase was transferred to a new tube. 500 µl Isopropanol per 1ml of Trizol was poured into each tube. After inverting several times, samples were again incubated for 5-10 minutes. Next, they were centrifuged for 10 minutes. The resulting RNA pellet was resuspended in 1ml 75% Ethanol in DEPC-H_2O (Diethylpyrocarbonate). Samples were centrifuged for 5 minutes, and the supernatant was discarded.

The RNA pellet was rewashed in 75% Ethanol in DEPC-H_2O and centrifuged. The liquid was removed by drying in air for 10 minutes. The pellet was then resuspended in 30 – 50 µl of nuclease-free water (depending on pellet size) and then incubated for 10 minutes at 55°C and 300 rpm in a thermomixer. RNA was stored at -80°C.

4.5 DNA Isolation

To obtain an adequate amount of tissue, frozen skin was cut on dry ice using punching material (pfm medical, Kai medical, Disposable Biopsy punch, diameter of 4mm) and weighed (Figure 16). The tissue was cut into small pieces using scalpels and placed in a tube. DNA Isolation was performed using the Blood & Tissue kit (QIAGEN®), according to the manufacturer's protocol.

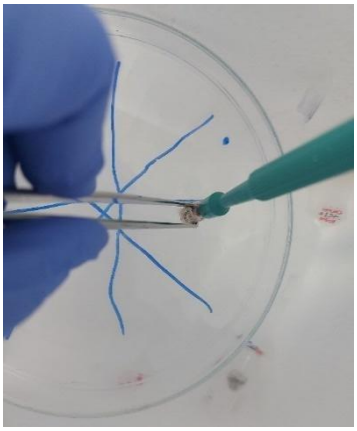

Figure 16: Tissue biopsies. Small punches were made from frozen fibrotic skin to obtain the precise weight of 25 mg per sample.

4.6 Quantitative PCR

To determine the relative mtDNA copy number *in vitro* and *in situ,* quantitative PCR (qPCR) was performed on whole genomic DNA from fibroblasts and dermal lysates, respectively. The qPCR was carried out with the Quantitect SYBR Green RT-PCR Kit (QIAGEN®) (Table 3) according to the manufacturer's protocol, using the following primers (5'-3'): mtDNA: forward

5’-CCTATCACCCTTGCCATCAT, reverse 5’-GAGGCTGTTGCTTGTGGTAC. nucDNA (*pecam 1*): forward 5’-ATGGAAAGCCTGCCATCATG, reverse 5’-TCCTTGTTGTTCAGCATCAT. A MicroAmp Fast 96well Reaction Plate (Thermo Fisher) was used, and biological triplicates were pipetted, including water as a negative control. qPCR results were obtained with the QuantStudio 1 Real-Time PCR system (Applied Biosystems, Thermo Fisher). The relative nuc/mtDNA ratio was determined using the formula $2^{-\Delta\Delta Ct}$ (Δ: delta, Ct: cycle threshold) in Excel:

$$\textit{Relative mtDNA copy number} = 2^{-\Delta\Delta Ct}$$

$$\textit{Where } \Delta Ct \textit{ (of control or mutant)} = Ct \textit{ (nucDNA)} - Ct \textit{ (mtDNA)}$$

$$\Delta\Delta Ct = \Delta Ct \textit{ (controls or mutants)} - \Delta Ct \textit{ (controls)}$$

To measure gene expression of Collagen 1 (*col1)*, cDNA from Twinkle^{FIBRO} skin and the following primers were used (5’-3’): forward 5’-ACGTCCTGGTGAAGTTGGTC, reverse 5’TCCAGCAATACCCTGAGGTC. GAPDH (*gapdh*) was used as a housekeeping gene, with the following primers: forward 5’-ACTCCACTCACGGCAAATTC, reverse 5’ TCTCCATGGTGGTGAAGACA. The amplified PCR fragments had a maximum length of 250 bp, with an annealing temperature of 60°C. The relative gene expression was calculated using the relative quantification $2^{-\Delta\Delta Ct}$ in Excel:

$$\textit{Gene expression} = 2^{-\Delta\Delta Ct}$$

$$\textit{Where } \Delta Ct \textit{ (of control or mutant)} = Ct \textit{ (gene of interest)} - Ct \textit{ (housekeeping gene)}$$

$$\Delta\Delta Ct = \Delta Ct \textit{ (controls or mutants)} - \Delta Ct \textit{ (controls)}$$

SYBR Green RT-Master Mix	**10 µl**
Primer For. (10 µM)	0,4 µl
Primer Rev. (10 µM)	0,4 µl
Water	5,2 µl
DNA 5 ng/µl	4 µl

Table 3: qPCR SYBR Green Master Mix for one sample.

4.7 Cell Culture

Fibroblasts were isolated from newborn (P0-3) Twinkle^{FIBRO} mice, which were killed by decapitation to perform cell culture experiments. They were then subjected to a disinfection series: Betaisodona with dPBS (Dulbecco’s Phosphate Buffered Saline, Gibco) 1:1 for 2 minutes, immersed in dPBS, Ethanol 70% for 1 minute, immersed again in dPBS, and Antibiotic-Antimycotic (Gibco) for 2 minutes. Then the mice’ skin was removed and thoroughly minced using scalpels (nr. 22) and scissors and placed in a Falcon tube containing Collagenase I (Worthington, Cat-No: CLS-1(400 U/ml) for 2 hours, shaking vigorously every

15 minutes. The collagenase solution (10ml) was filtered through a 70 µm filter (Starlab, Hamburg, Germany). The samples were centrifuged at 5000 rpm for 5 minutes. Petri dishes were coated with Collagen G (Sigma) for 1,5-2h at room temperature or overnight at 4°C and washed once with PBS before the fibroblasts were plated in Dulbecco's modified Eagle Medium + GlutaMAXtm (Gibco) supplemented with 10% Fetal Bovine Serum (FBS) (Gibco/ Thermo Fisher), 1x Pen/Strep (Gibco/Thermo Fisher), 2mM Pyruvat (Gibco/Thermo Fisher) and 50 µg/ml Uridine[129]. Cells were incubated at 37°C with 5% CO_2 and passaged up to 3 times until they reached 90% confluency. For splitting purposes, a 2,5% Trypsin solution (Gibco) was applied for 5 minutes at 37°C. An equal volume of DMEM was used to stop the reaction. The samples were centrifuged and plated on new petri dishes.

4.7.1 Mutation induction

The K320E Twinkle mutation was activated in freshly isolated K320-Twinkle$^{ColCre-/+}$ fibroblasts using 4-OH Tamoxifen (5□M in DMEM, SigmaH-7904) (Figure 13). Since Tamoxifen is metabolised in the liver to its active form *in vivo*[130], this hydroxylated and thus already activated form of Tamoxifen has to be used *in vitro*. The cells were treated with 4-OH for 48 hours. Once the cells were ready for experiments, they were used directly or snap-frozen and stored in a nitrogen tank.

4.7.2 FACS

4.7.2.1 Procedure for flow cytometric cell sorting

Cells were trypsinised as described above, and adding PBS stopped the reaction. Samples were centrifuged, filtered through nylon-mesh filters with 30 µm pore size (Sysmex cell tricks) and resuspended in FACS Buffer (1% BSA, 2 mm EDTA in DPBS) so that the concentration was 10 Mio/ml (= 1 × 10^7 cells per ml). Cells were sorted due to their GFP tag labelling, measured at a fluorescence between 10^3 and 10^4 (Figure 17) on a FACSAria III cell sorter using FACSDiva Version 6.1.1 (BD Biosciences) or FlowJo Version 7.6.4 (TreeStar) software. Control cells served as an autofluorescent baseline measurement and differentiation from GFP+ cells.

A Control **B** Mutant

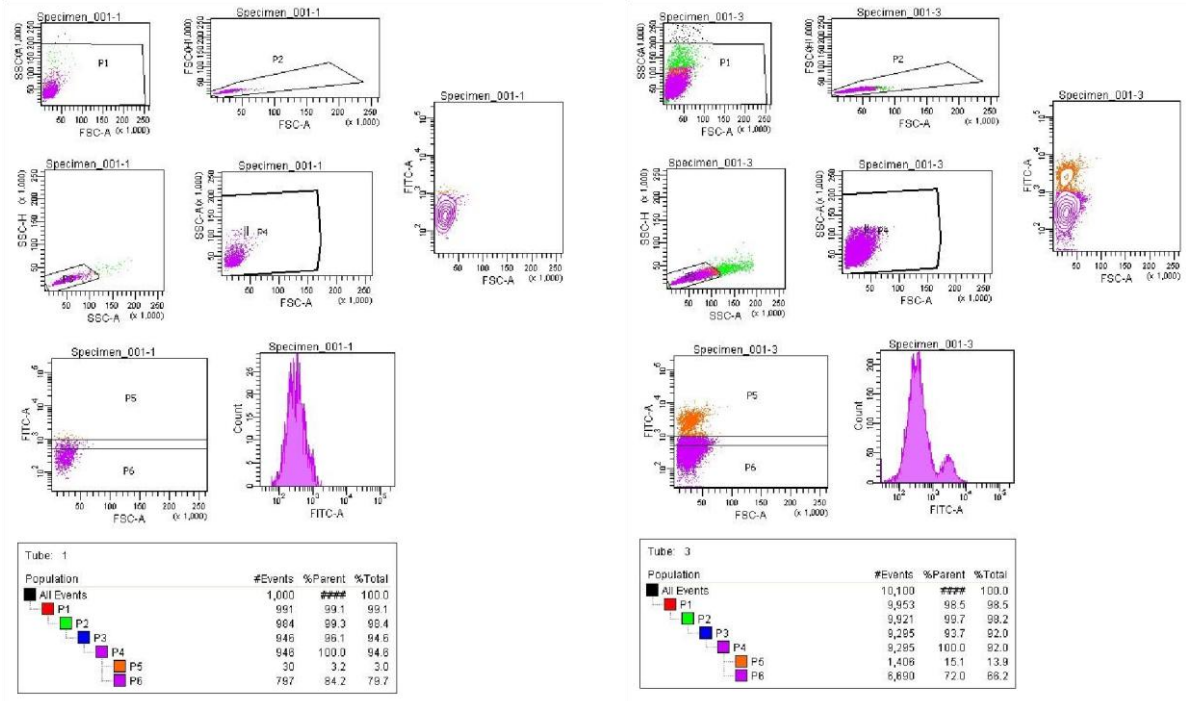

Figure 17: FACS of Twinkle^{FIBRO} fibroblasts sorted by GFP expression in (A) control and **(B)** mutant. The workflow of all cells is shown in Population 1 (P1). Total events were gated in a scatter plot and subjected to FSC-based (P2) and SSC-based (P3) single-cell gating to exclude doublets. P4 shows the workflow of single cells. The population P5 refers to the GFP+ cells – those present in the control's graph likely represent artefacts - and P6 refers to the remaining cells that express a certain amount of autofluorescence. The histogram of mutants shows the GFP+ population in the right peak (FITC-A between 10^3 and 10^4). FCS-A and SSC-A represent size and granularity, respectively, and are displayed on a linear scale. On the other hand, FITC's values detect the GFP signal and are presented on a logarithmic scale. Count on the y-axis are the events, thus, cells per second. Abbreviations: SSC: Side Scatter; FSC: Forward Scatter; H: Height; A: Area; P: population; FITC: Fluorescein isothiocyanate; GFP: Green Fluorescent Protein.

4.7.2.2 Procedure for flow cytometric analysis

Fibroblasts were isolated and diluted in 300µl of FACS Buffer, then kept on ice[131]. GFP$^{-/+}$ cells were analysed with a FACSCanto II flow cytometer (Becton Dickinson). The analysis involved a minimum of 10,000 cells. Wild-type and Twinkle^{FIBRO} fibroblasts were treated as described above, then isolated, washed with PBS, and resuspended in 200µl phenol-free Hanks' Balanced Salt Solution (HBSS) with Mg^{2+} and Ca^{2+} (Gibco/ Thermo Fisher) at a concentration of 1 × 10^6 cells/ml. Cells were stained for reactive oxygen species (ROS), mitochondrial membrane potential (mtMP), and mitochondrial mass using MitoSOX (2.5 µM for 20 min), TMRM (100 nM for 30 min), and Mitotracker Deep Red (50 nM for 30 min) at 37°C before sorting. To assess mtMP, cells were gated into TMRM^{low} and TMRM^{high} populations. MtMP was quantified by comparing the relative distribution of signal intensity in GFP$^-$ and GFP$^+$ cells within each gate. To study mitophagy induction in Twinkle^{FIBRO} fibroblasts, cells were stained with Mitotracker (50 nM) and treated with low-dose CCCP (10 µM) for 12 h to induce mitophagy. Mitotracker staining was performed before CCCP treatment to ensure accurate interpretation, since this staining depends on mtMP, which is reduced upon treatment with protonophores.

Positive controls for ROS and mtMP were treated with H_2O_2 (200 µM) and CCCP (60 µM), respectively. Samples were co-stained with SytoxBlue (500 nM) to exclude dead cells, washed with FACS buffer (1% BSA, 2 mM EDTA in PBS), and analysed by flow cytometry. Cell debris was excluded using FlowJo V7.6.3 software (Treestar, Ashland), and the viable GFP^+ or GFP^- populations from Tamoxifen-treated $ColCre^+$ fibroblasts were measured. This method allowed for intraindividual comparison, showing that GFP^- populations of $ColCre^+$ fibroblasts behaved similarly to GFP^- populations of $ColCre^-$ fibroblasts. Mean fluorescence intensity in the PE (MitoSOX) or APC (Mitotracker Deep Red) channels and the percentage of PE^{low} and PE^{high} cells (TMRM) were determined.

4.8 Long-Range PCR

An established method for determining the presence of deletions is long-range PCR. This type of PCR allows the amplification of a DNA fragment larger than 5 Kb using a particular type of high-fidelity DNA polymerase. Conventional Taq polymerase is usually used for DNA fragments less than 2 or 1 Kb, as its specificity decreases beyond that, and the likelihood of incorrect incorporation of dNTPs increases[132]. Therefore, we amplified the deleted mtDNA molecules of $Twinkle^{FIBRO}$ dermal lysates *in situ* using the Long-Range PCR Kit (Biotechrabbit), including a high-fidelity Taq Polymerase with a 3' to 5' exonuclease activity of high specificity and fidelity. PCR was performed according to the manufacturer's protocol. Used primers (Sigma) were (5'-3'): mLRmtDNA-F 5' GTTCAACGATTAAAGTCCTACGT and mLRmtDNA–R 5' –GTTGTTTGATCCTGTTTCGTG. The PCR conditions were 96°C for 3 minutes, 25 cycles of 95°C for 30 seconds, 55°C for 30 seconds, 68°C for 7 minutes, 20 cycles of 95°C for 30 seconds, 55°C for 30 seconds, 68°C for 14 minutes and 68°C for 10 minutes. After completion of the PCR, a 6x loading dye was added to each sample (Lambda DNA/HindIII-Marker, Thermo Fisher). The samples were loaded onto a 1% agarose gel electrophorese and the gel ran in TAE Buffer at 80 mV for 1h30. Stained with ethidium bromide (0,8 µg/ml), the PCR products were visualised under UV light.

4.9 Immunohistochemistry

4.9.1 Paraffin sections

After cervical dislocation, whole and fibrotic skin were cut, as shown in Figure 15 B and Figure 18. The fibrotic region labelled in blue was cut in the middle. The first half was spread out on a sheet of paper and cut again along the long axis. The two skin sections were placed horizontally in kerosene cassettes between sponges soaked in PFA 4% and stored overnight in PFA 4%. The next day, paraffin embedding was performed in the Tissue Embedding and Histology Unit (TEHU) of the CMMC, University of Cologne. The dermis was dehydrated in

70% Ethanol and a series of Isopropanol at 45°C, cleared in xylene and immersed in paraffin wax at 65°C. The resulting paraffin blocks were stored at room temperature. Sections were cut on a microtome (12 µm thick), placed on water heated to 37°C and finally placed on a slide and dried overnight at 37°C.

4.9.2 Frozen cryosections

The second remaining part of the fibrotic region (Figure 15 B) was further used to produce frozen sections. This half was spread out on a sheet of filter paper and cut along the long axis once again. The two skin sections were mounted in cryomold (cryomold standard 25mmx20mmx5mm, Sakura) with OCT medium (Tissue-Tek), snap-frozen in liquid nitrogen, and stored at −80 °C until needed. The sections were then freshly cut using a cryotome at -20 °C (10-14 µm thick).

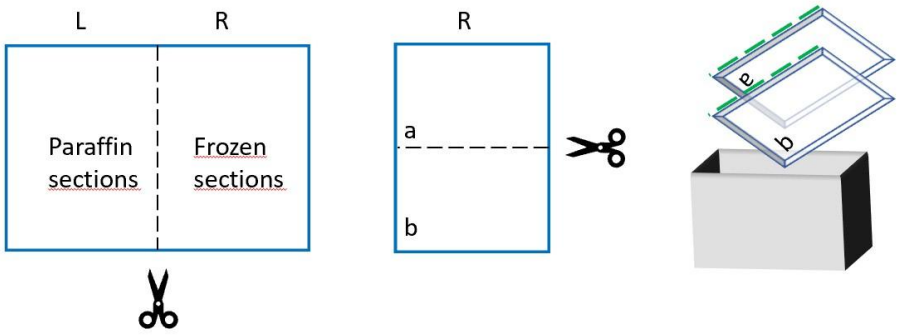

Figure 18: Modell showing frozen tissue embedding of Twinkle^{FIBRO} skin. The blue squared area refers to the fibrotic region in the neck area of the mice. The dotted line indicates where the skin was incised with the scalpel, while the dotted green line indicates which side of the tissue was incised for visual orientation. L and R refer to “left” and “right”, respectively; a and b allow visualising of the placement of the tissue in the mould (grey box). The illustration was made using PowerPoint.

4.9.3 Imaging

X-gal staining images were acquired using a light microscope (Nikon microscope Eclipse Ts 2-FL). Ki67, Collagen 1, HE and TM immunohistochemistry were visualised with a Slidescanner (S360, Hamamatsu) at different magnifications (NA 0,75, 20x and 40x). The Picro Sirius Red staining images were photographed under a polarised microscope (Leica DM4000 B, software: DISKUS 5.0) at 5x and 10x magnifications using consistent illumination. The remaining stainings were acquired with EVOS (FL Auto 2 Cell Imaging System) at CECAD, University of Cologne. The objectives used at the Evos Microscope are 5×, NA 0.15; 10×, NA 0.4; and 40×, NA 0.75. EVOS-acquired images were analysed using Fiji software.

4.9.4 Analysis

4.9.4.1 Counting Cells

After staining for Ki67, Caspase-3, α-SMA and x-gal, positive cells were counted manually according to specific morphological changes. For some of these stainings, positive cells were

normalised to the number of nuclei (indicated on the graph's y-axis). The epidermis, hair follicles and background were excluded, and DAPI-positive cells were outlined and quantified using the "analyse particle" function in Fiji software (Figure 19).

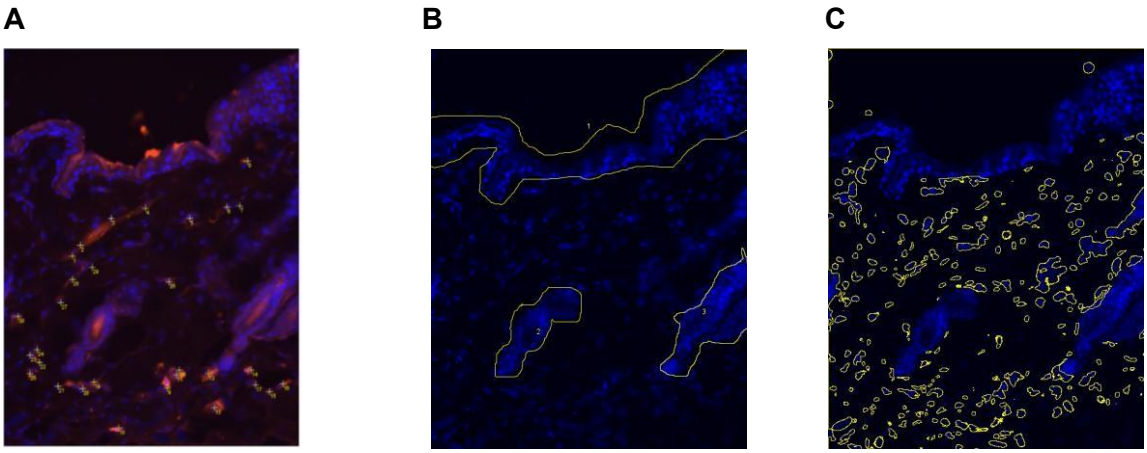

Figure 19: Work steps of apoptosis analysis in Twinkle^{FIBRO} dermis, using Fiji software. **(A)** Apoptotic cells are represented in red (RFP) and nuclei in blue (DAPI). Apoptotic cells are counted manually in all HPFs. **(B)** Next, the epidermis is excluded (middle image). **(C)** Ultimately, nuclei are quantified through particle analysis. For apoptosis assessment, the mean of apoptotic cells per HPF is divided by the mean of nuclei per HPF. The images were taken on an EVOS microscope and analysed using Fiji.

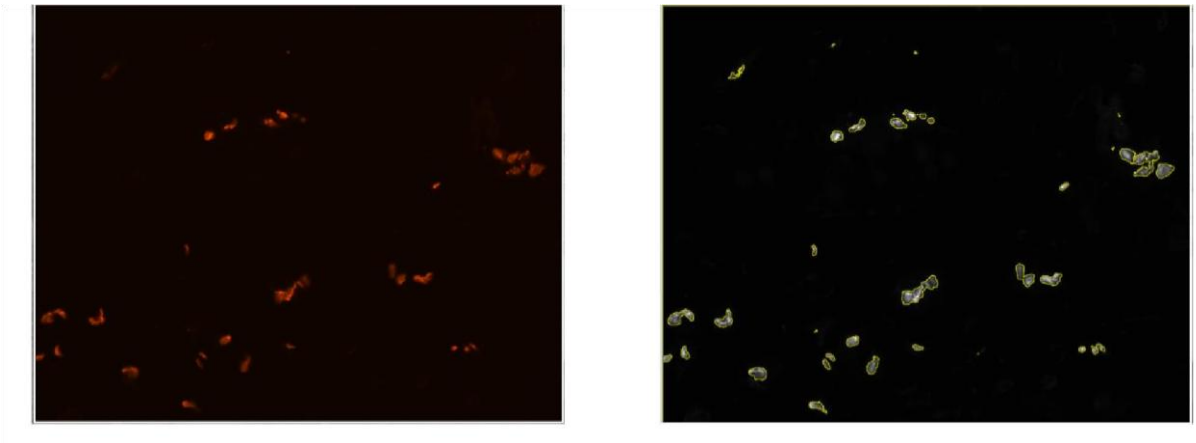

Figure 20: Work steps of morphometric analysis of myofibroblast differentiation in Twinkle^{FIBRO} skin, using Fiji software. The first image shows a raw shot of αSMA staining (Red Fluorescence Protein (RFP) filter).
The second image shows the selection of myofibroblasts only (yellow line), permitting accurate measurement of MFI within the boundary, excluding the background. The photos were taken using an EVOS microscope and analysed using Fiji.

4.9.4.2 Quantifying Signal Intensity

The density of collagen fibres or the extent of protein expression was measured using the mean signal intensity. For Collagen 1, colour deconvolution using Fiji software highlighted collagen fibres specifically. Next, the dermal area was defined, and the epidermis, hair follicles and background were excluded. The resulting area was analysed using the Mean Fluorescence Intensity (MFI) function. For α-SMA expression, the picture type was changed to a 16-bit image and the threshold was adjusted until the background turned black and only fluorescent cells were seen (Figure 20). Next, a selection of cells was created and saved to ROI Manager. From

here, MFI could be assessed in isolated myofibroblasts, excluding the background. The mean MFI value per High Power Field (HPF) (7000 × 5500 µm²) was used to compare mutants and controls.

4.9.4.3 Morphometric analysis

Thickness and width were quantified (Figure 21) on HE-stained skin for assessment of fibrosis. Images were acquired with the Slidescanner (S360, Hamamatsu) at different magnifications (NA 0,75, 20x and 40x) and analysed with NDP-view2 software (Hamamatsu). The thickness and width of the largest fibrotic region were measured in a blinded manner by two independent investigators. Skin thickness can vary from mouse to mouse, so the maximum measured thickness was further normalised by dividing it by the thinnest region, referring to the standard skin size.

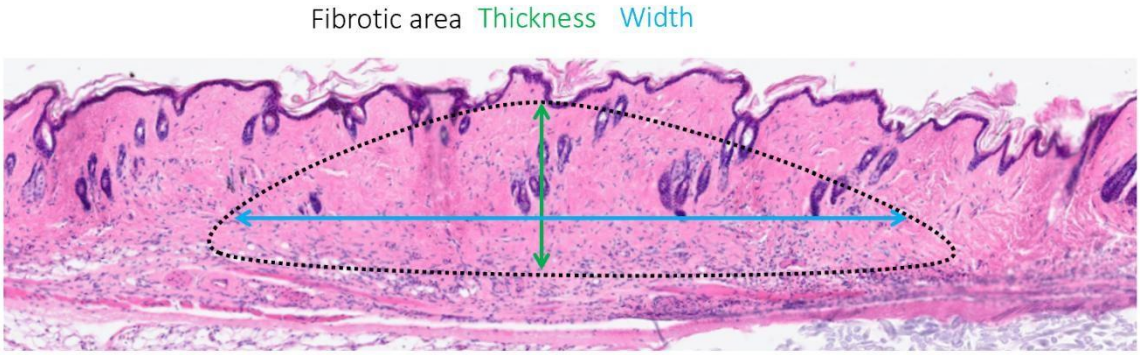

Figure 21: Morphometric analysis of fibrotic skin in HE-staining of Twinkle^{FIBRO} skin. This section shows a fibrotic area (black, in dotted lines) that exhibits stigmata such as increased ECM deposits, scarce hair follicles and a corrugated epidermis. Thickness (green) and width (blue) are represented. The image was made using the Hamamatsu slide scanner; quantitative measurement was performed using NDP-view2 software. The figure was created on PowerPoint.

4.9.4.4 Texture analysis

For Second Harmony Generation (SHG) images, five representative Regions of Interest[133] (120x120 pixels) of the fibrotic region were selected in Fiji (

Figure 22), and the mean intensity and entropy were measured using Cell profiler software. A pipeline for each ROI was applied on Cell profiler, in which 256 grey levels and a texture scale of 5 were set. The results were exported to Excel. For the mean intensity, MFI was assessed. The Gray-level co-occurrence matrix (GLCM) method was used to calculate entropy: a set of features is extracted from a cross-diagonal matrix, relying on grey levels, and used to describe texture information. For image I, a matrix of relative frequencies p(i,j), defined as the number of pixel pairs (i,j), separated by distance d, at a specified angle θ. For Entropy, measuring the complexity of pixel intensity distributions within an image, the following formula was used[134]:

$$Entropy = -\sum_{i}\sum_{j} p\,(i,j) Log2\; p(i,j)$$

For Picro Sirius Red staining, a pipeline identifying, counting and measuring the intensity of collagen fibres with manually predefined sizes was used. The total amount of collagen fibres was normalised to the total area of the dermis using Excel.

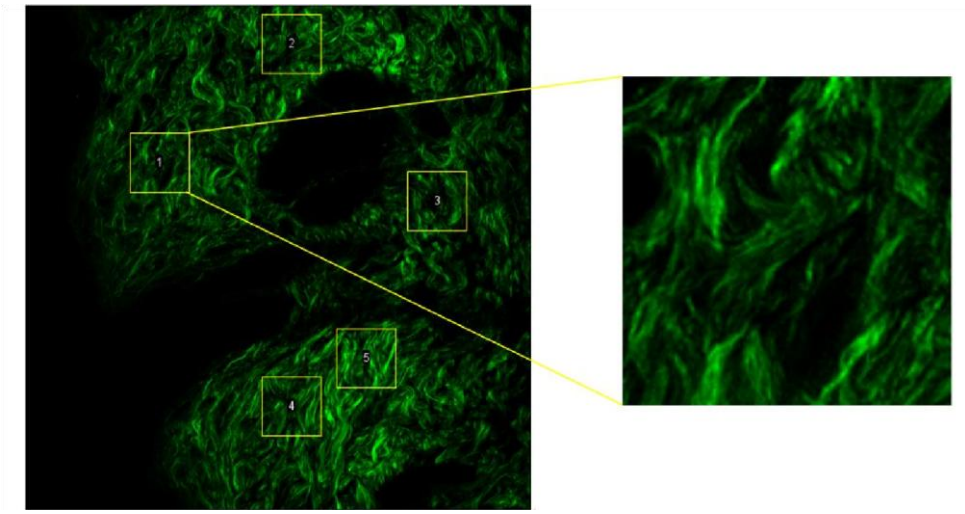

Figure 22: Representative ROI selection on Fiji of SHG imaging of Bleomycin-treated Twinkle^{FIBRO} mouse. The left picture shows a representative SHG shot, and the right image is a close-up of ROI 1. Each ROI was further analysed using Cell Profiler software.

4.9.5 α-Smooth Muscle Actin

4.9.5.1 In situ

To investigate the differentiation of fibroblasts into myofibroblasts, α-Smooth Muscle Actin (αSMA) stress fibres were detected on frozen cryosections of Twinkle^{FIBRO} skin.

To ensure good adhesion of the skin to the slide, the frozen cryosections were air-dried for 20 minutes and fixed in acetone at -20°C for 2 minutes. The slides were washed three times in PBS for 5 minutes. They were then blocked with a 10% FCS/-PBS solution for 30 minutes and briefly washed in PBS. The Cy3 conjugated αSMA (Sigma, C6198) antibody was diluted to 1:250 in Antibody Diluent (DAKO) and applied to the slides for 1 hour in the dark at room temperature. Because of its Cy3 conjugation, it can be directly used, and no secondary antibody is required. Merely DAKO was applied to the negative control. Finally, the slides were washed in PBS and covered with Fluoromount-G, including 4',6'-diamidin-2'-phenylindoldihydrochloride (DAPI) (Invitrogen).

4.9.5.2 In vitro

GFP+ sorted Twinkle^{FIBRO} fibroblasts were fixed with PFA 4% and permeabilised with Triton x100 in PBS for 10 minutes. After washing with PBS, cells were blocked with 5% Bovine Serum Albumin (BSA) in PBS at room temperature. Next, αSMA Cy3 antibody diluted in DAKO 1:300 was applied in the dark, at room temperature for 1 h. The negative control received DAKO

diluent containing no antibody. After washing, the slides were mounted with Fluoromount-G, including DAPI.

4.9.5.3 Positive controls

Biopsy punches of wild-type mice seven days after wounding served as a positive control for *in situ* staining, as myofibroblasts develop SMA-fibres in granulating tissue[49]. Tumor Growth Factor (TGF-β, R&D Systems, 240-B) treated cells (1ng/µl) were used for *in vitro* staining, as it induces differentiation to myofibroblasts in a canonical (SMAD-dependant, TGFBR1) or noncanonical way (MAPK/JNK/p38 pathway, TGFBR2)[135].

4.9.6 Collagen 1

Collagen 1 analysis was performed on paraffin-embedded slides. Sections were deparaffinised, hydrated, and underwent antigen retrieval using a citrate buffer (pH=6). Endogenous peroxidase activity was blocked with a methanol-H_2O_2 solution. After blocking with Normal Goat Serum (NGS), sections were incubated with the Col1 antibody (1:2000, Cedarlane, Burlington, USA) in antibody diluent overnight at 4°C. As a second antibody, a biotin-conjugated donkey anti-rabbit antibody was used (1:2000, Jackson Laboratory, Bar Harbor, USA). Following incubation with the ABC kit (Vector Laboratories, Newark, USA), Col1 was visualised using DAB for 3 minutes (Vector Laboratories), and sections were counterstained with haematoxylin.

4.9.7 Sirius Red staining

For further collagen assessment, Sirius Red staining was performed with the Picro-Sirius Red Kit Dianova (Calibre Scientific, Holland, US). The paraffin slides were deparaffinised in xylol for 20 minutes. Next, they were hydrated in Isopropanol, followed by a decreasing series of alcohol. After rinsing with deionised water, the slides were stained with Weigert's Iron Hematoxylin for 5 minutes. After rinsing again, the slides were imbued with warm tap water. Next, the cytoplasm was decolourised using 0.75% HCl alcohol, and the Picro Sirius Red solution was added for 1h15. The sections were rinsed with 0.5% acetic acid water and dehydrated with an increasing ethanol series and xylol for 10 and 2 minutes, respectively.
Lastly, slides were covered with Entellan (Sigma).

4.9.8 Caspase-3

An antibody against caspase-3 (Cell signaling, #9664) was used to assess the apoptosis rate in Twinkle^{FIBRO} mice. The frozen cryosections were air dried and then fixed with 4% PFA at room temperature. The slides were washed once in PBS and subsequently blocked with 5% normal goat serum (NGS) 0,3% Triton x-100 in PBS for 1h. The Caspase-3 Antibody was diluted 1:200 in DAKO and applied overnight at 4°C. On the next day, the samples were

washed with PBS. The second antibody, goat-anti-rabbit Alexa Fluor 555 (Thermo Fisher molecular probes, A-21428), was diluted 1:500 in DAKO and applied for 1h in the dark. The negative control received DAKO only. After washing in PBS, the slides were mounted with Fluoromount-G, including DAPI nuclear background staining.

4.9.8.1 Positive controls

Keratinocytes from the epidermis were used as a positive control, containing a high apoptotic rate in the basal layer[29].

4.9.9 Beta Galactosidase enzymatic activity

4.9.9.1 In situ

Senescence was analysed by β-galactosidase activity. 5-Brom-4-Chlor-3-Indolyl-Beta-DGalactopyranosid (x-gal) was used as a chromogen substrate for β-Galactosidase, which turns x-gal into a colourless galactose and hydrolyses 4-Chlor-3-Brom-Indigo, which creates an intensive blue precipitate. The frozen cryosections were air dried and fixed with 0,2% glutaraldehyde for 20 minutes. They were washed thrice for 5 minutes with 2 mM $MgCl_2$/0,02 % NP-40 in PBS. Slides were covered with an x-gal working solution (PBS pH=6, potassium chloride 5mM, $MgCl_2$ solution 1mM and x-gal 1mg/ml) (R0404, Thermo Fisher) overnight at 37°C. The negative control received PBS only. The slides were washed as described and counterstained with a nuclear fast red solution (ScyTek Laboratories) for 5 minutes at room temperature. Afterwards, slides were dehydrated by increasing alcohol series (50%, 75%, 95% and 99%) and then mounted with Kaiser's glycerol gelatine, previously heated up to 65°C.

4.9.9.2 In vitro

GFP+ sorted Twinkle^{FIBRO} fibroblasts were fixed with 0,2% glutaraldehyde at room temperature for 10 minutes. They were washed with PBS and covered with the x-gal working solution overnight at 37°C in the dark. The negative control was covered with PBS only. Cells were rewashed and mounted with Kaiser's glycerol gelatine, previously heated to 65°C.

4.9.9.3 Positive controls

Sections of the caput epididymis from WT adult mice were used for *in situ* staining. This region, situated at the superior pole of the testis, connects the efferent ducts to the testicle. In this mature tissue, senescent cells are abundant[136]. Positive control for *in vitro* staining was performed with isolated wild-type dermal fibroblasts. Senescence was induced by yirradiation[137] using the Biobeam 8000 (CECAD, AG Schumacher) at room temperature, with a dose of 15 Gray (dose rate of ± 5 Gy/minute). A cylindrical irradiation container (140x220mm)

provided a homogeneous irradiation flux with a Cs137 gamma-ray source and a total activity of 81,4 TBq ± 20% (i.e. up to 20% deviation of the irradiation source). The fibroblasts rested for seven additional days, changing DMEM once after three days. X-gal staining of the irradiated fibroblasts was performed as described above.

4.9.10 Ki67

For proliferation rate assessment, Ki-67 detection was performed in routine diagnostics of the Dermatohistology at the University of Cologne, according to the Leica® BOND™ protocol. The sections were dewaxed using 100% alcohol. Antigen retrieval was done with an epitope retrieval (ER2 solution) for 20 minutes at 100°C. Next, peroxide was applied for 5 minutes.
After washing, proteins were blocked with NGS (#5425) for 20 minutes. The Ki-67 antibody (PA0118, Leica) was diluted in SignalStain® Antibody Diluent (#8112), and samples were incubated for 30 minutes. Detection was enhanced by counterstaining with Hematoxylin. Sections were dehydrated in 95% and 100% ethanol, followed by xylene, twice each time for 10 seconds. Lastly, sections were mounted with SignalStain® Mounting Medium (#14177).

4.9.10.1 Positive controls

For ki-67 staining, the positive control was the epidermis, a highly proliferating tissue[29].

4.9.11 Skin Morphology

Haematoxylin-Eosin and Trichrom-Masson staining were performed in the Dermatohistology routine diagnostics, Dermatology department of the University Hospital Cologne. Pictures were taken on the Hamamatsu Slidescanner (S360), NA 0,75, 20x, and 40x.

4.9.11.1 HE-staining

The paraffin slides were deparaffinised in xylol for 15 minutes. Next, they were hydrated in a decreasing series of alcohol. After rinsing with deionised water, the slides were stained with Hematoxylin for 10 minutes. After rinsing again, the slides were imbued with warm tap water. Next, the slides were stained with eosin for 10 seconds, highlighting the cell cytoplasm. After rinsing, sections were dehydrated in a rising alcohol series and, lastly, paraffinised with xylol for 5 minutes.

4.9.11.2 Trichrom Masson-staining

Like HE-staining, slides were deparaffinised in xylol and decreasing alcohol series. After rinsing in deionised water, samples were stained with Resorcin-Fuchsin for 15 minutes and iron-Hematoxylin for 3 minutes. They were rinsed and shortly dipped in HCL. After rinsing, slides were imbued in Goldner-solution and rinsed again in deionised water, acetic, and deionised

water. This procedure was repeated thrice, with the Goldner-solution staining for 1, 5 and ultimately 4 minutes. Lastly, sections were paraffinised in a rising alcohol series and xylol.

4.9.11.3 Morphometric analysis

For fibrotic assessment, thickness and width were quantified for objective measurement (Figure 21). Images were acquired with the Slidescanner (S360, Hamamatsu) at different magnifications (NA 0,75, 20x and 40x) and analysed with NDP-view2 software (Hamamatsu). The thickness and width of the largest fibrotic region were measured in a blinded manner by two independent investigators. Skin thickness can vary from mouse to mouse, so the maximum measured thickness was further normalised by dividing it by the thinnest region, referring to the standard skin size.

4.9.12 Second Harmony Generation (SHG)

HE Paraffin slides of Bleomycin-treated Twinkle^{FIBRO} mice were used for collagen structure analysis. Pictures of the most representative fibrotic areas were taken on a multiphoton microscope (TCS SP8MP; Leica Microsystems, CECAD) equipped with a Ti:Sa laser (Chameleon Vision II; Coherent). 1024x1024 pixel images, picturing collagen and elastin molecules, were acquired via LAS X software (Leica Microsystems).

4.10 Immunoblotting

To detect protein expression in Twinkle^{FIBRO} fibroblasts, immunoblotting was performed with sodium dodecyl sulfate-polyacrylamide gel electrophoresis (SDS-PAGE).

1,5 mm thick gels were made in the laboratory using the BioRad recipe. First, a separating gel was prepared, containing 10% or 12% of 30% Acrylamide and 10% SDS (Table 4). In each chamber, 7,5 ml was added, and 1 ml of Isopropanol as an overlay prevented the gel from drying. 10 minutes later, the gel is polymerised and can be rinsed with water. The stacking gel, containing 4,5% of 30% Acrylamide, was added on top of the separating gel, and ten lane combs were directly inserted. After polymerisation, the comb was removed, and the gel was ready to be used.

30 µg of protein were mixed with 4x Laemmli buffer (Tris (1.0 M, pH 6.8) 10 mL, SDS 4.0 g, Glycerol 20 mL, β-Mercaptoethanol 10 mL, Bromophenol blue 0.1 g, dH2O to 50 mL) and dH2O (distilled), reaching a total volume of 20 µl. For protein denaturation, the samples were boiled at 95°C for 1 minute for the detection of MTCO1 complex subunit and up to 5 minutes for the detection of all remaining proteins (Table 7). They were then loaded into the wells, and the Pageruler prestained protein ladder (Thermo Fisher, 26616), reaching from 10 kDa to 180 kDa, was used as a loading dye in a separate well. The loaded gels were placed in the BioRad Holder Frame, and the electrophoretic separation occurred in running buffer (100 ml of the 10x

stock (Table 5) + 900 ml of dH2O) containing SDS to give all proteins a uniform negative charge. This enables migration toward the positively charged anode, whereby smaller proteins migrate faster, resulting in a separation according to the protein's size, measured in kDa. First, the samples were run at 100V, and after 30 minutes, once the samples had equally descended and a uniform line was seen, the voltage increased to 130V.

After 1h30-2h, the proteins were transferred onto a polyvinylidene difluoride (PVDF) membrane, which was previously activated in Methanol for 5 minutes. Placed between sponges and Whatman paper sheets, the gel is placed so the proteins are transferred from the gel to the membrane, thus moving from the cathode toward the anode. The electric current is set at 100V, and the transfer is emphasised by the transfer buffer (100 ml of the 10x stock (Table 6) +700 ml of dH2O + 200 ml of Methanol) and a cold environment (4°C).

After 2 hours of electroblotting, the membrane was shortly washed with H2O, and staining with Ponceau S (Serva, SV-0032) permitted the rapid visualisation of the effectiveness of the transfer and could also be used as a loading control. The membranes were washed in TBST (tris-buffered saline with the detergent Tween 20) (100ml 10x Stock TBS + 900ml dH2O + 500 µl Tween 20) 3 times for 5 minutes and subsequently blocked in 5% milk in TBST for 1h at room temperature, to avoid non-specific binding. After washing with TBST, the membranes were incubated in 5% milk in TBST containing the first antibody (Table 7) overnight at 4°C. The samples were then washed with TBST, incubated with the second antibody (Table 7) at room temperature for 1h and washed again.

The secondary antibody is conjugated to a Horse Radish Peroxidase (HRP) enzyme, which, in contact with a chemiluminescent substrate, cleaves it and luminescence results, allowing to visualise the proteins under exposure to light. The HRP reacted with the HRP substrate luminol from an enhanced electrochemiluminescence (ECL) solution (Advanced Chemiluminescence kit, GE Healthcare Life Sciences). The membranes were covered with ECL solution, inserted in a plastic film, and placed under the camera of the ImageQuant LAS 500 (Cytivia) for digital detection of the proteins. The ImageQuant is equipped with a Peltier-cooled, 8.3-megapixel CCD sensor and an F1.4/30 mm lens. It uses UV (365 nm), Blue (460 nm) and white (470-635 nm) epi-light. For pictures, the automatic exposure uses a pre-exposure of the membrane to determine the signal intensity. It suggests an exposure time for an optimal signal without saturating the image (1-30 minutes). Additionally, the incremental exposure mode was used, allowing a series of different exposure times (for instance, every 5 minutes) for a fine-tuned saturation measurement of the membrane. The image is analysed by densitometry, in which the integrated density of protein bands is measured in terms of optical density, using Fiji software.

	Separating gel		Stacking gel
Acrylamide (%)	**10%**	**12%**	**4,5%**
MilliQ H2O	3,43 ml	2,46 ml	1,75 ml
1,5M Tris pH 8,8	1,88 ml	1,88 ml	750 µl (pH 6,8)
30% Acrylamide	2,02 ml	3,0 ml	500 µl
10% SDS	75 µl	75 µl	30 µl
10% APS	75 µl	75 µl	30 µl
TEMED	7,5 µL	7,5 µL	3 µl

Table 4: Separating and stacking gel recipe for western blots. 10% gels were used for the detection of the following proteins: NDUFA9, SDH, UQCRC2, MTCO3, MTCO1, ATP-Synthase, and α-Smooth Muscle Actin. 15% gels: OxPhos Cocktail, P62 and LC3-B.

10x stock Running buffer (recipe for 1L)		
	Stock	**Final concentration**
30,28 g	Tris (mw: 121,14 g/mol) or TRIS BASE	250 mM
144,1 g	Glycine (mw: 75,07 g)	1,9 M
50 ml	20 % SDS	1 %
Dissolved in 1L deionised H20		

Table 5: 10x stock of SDS based Running buffer for 1L

10x stock Transfer buffer (recipe for 1L)		
	Stock	**Final concentration**
30,28 g	Tris (mw: 121,14 g/mol) or TRIS BASE	250 mM
144,1 g	Glycine (mw: 75,07 g)	1,9 M
Dissolved in 1L deionised H20, pH 8,3		

Table 6: 10x stock of Transfer buffer for 1L

Primary antibody	**Secondary antibody**
OxPhos	
Oxphos Cocktail (ab110413) 1:4000	Mouse 1:5000
Complex I: NDUFA9 (Invitrogen 459100) 1:1000	Mouse 1:5000

Complex II: SDH (Proteintech, 10620-1-AP) 1:2000	Rabbit 1:5.000
Complex III: UQCRC2 (abcam 14745) 1:1000	Mouse 1:5000
Complex IV: MTCO3 (Abcam, ab14744-100) 1:2000	Mouse 1:5000
Complex V: ATP Synthase Subunit-beta (Invitrogen, A21351) 1:1000	Mouse 1:5000
Autophagy	
P62 (Santa Cruz, sc-48402) 1:550	Mouse 1:5000
LC3-B (18725-1-AP**)** 1:1000	Rabbit 1:10.000
Differentiation into myofibroblasts	
Cy3 conjugated α-Smooth Muscle (Sigma, C6198) 1:250	
Loading control	
β-actin (Sigma) A1978, 1:1000	Mouse 1:1000
GAPDH (Milipore AB2302) 1:4000	Chicken 1:5000

Table 7: Primary and secondary antibodies used for Western Blots.

4.11 Statistical analysis

For all analyses conducted, statistical results were derived from Prism Version 8 software. The analyses employed were either unpaired two-tailed t-tests or Mann-Whitney tests, depending on the data distribution and assumptions of the respective tests. Whiskers were utilised to visually represent the means and standard deviations of the datasets. P-values <0.05 were deemed significant, with exact values reported directly on the graphs.

4.12 Material Table

Material	**Brand**	**Cat nr**
2,5% Trypsin	gibco	15090-046,
PBS (Dulbecco's Phosphate Buffered Saline)	gibco	14190.094
Pierce BCA Protein Assay Kit	Thermoscientific	23227
Sterile single-pack CellTrics® filters	Sysmex cell tricks	04-004-2326
TGF-β	R&D System	240-B
Antibiotic-Antimycotic	gibco	15240-096

Tissue-tek	Sakura	4583
Cryomold standard 25mmx20mmx5mm	Sakura	4577
Disposable Biopsy punch x20 4mm	Kaimedical	48401
αSMA Cy3 (red)	Sigma	C6198
Nuclear Fast Red Solution	ScyTek Laboratories	NFS125
Kaisers Glycerin-Gelatine	Roth	6474.1
X-Gal	Thermoscientific	R0404
Cleaved Caspase-3	Cell signaling	Asp175, #9664
Antibody Diluent 125 ml	DAKO	S3022
Alexa Fluor 555 - Goat anti-Rabbit IgG	Thermo Fisher molecular probes	A-21428
20x Phospho Inhibitor (PhosSTOP EASYpack)	Roche	04906 845 001
20x complete Inhibitor (Complete Mini, EDTAfree)	Roche	11836170001
Quantitect SYBR Green RT-PCR Kit	QIAGEN	A46012
Blood & Tissue kit	QIAGEN	69504
Long Range PCR Kit	Biotechrabbit	BR0300401
6x loading die Lambda DNA/HindIII-Marker	Thermo Fisher	SM0101
Immun-Blot PVDF Membrane, Roll, 26 cm x 3.3	BioRad	m1620177
Gel system	BioRad	1658050
ECL	Thermo Fisher	32106
Pageruler prestained protein ladder	Thermo Fisher	26617

5. Results

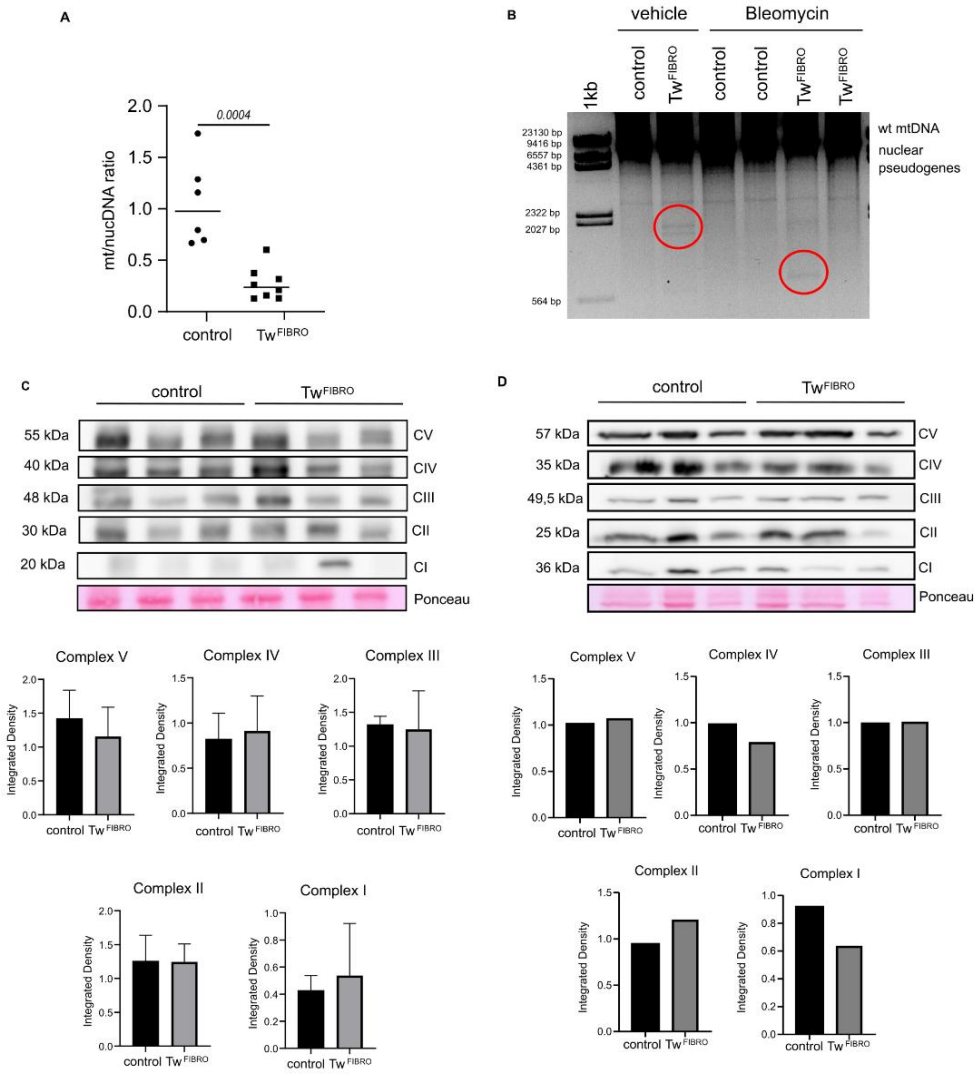

Figure 23: mtDNA deletions in Bleomycin-treated Twinkle^{FIBRO} mice do not significantly affect OxPhos stoichiometry. (A) mtDNA copy number of Twinkle^{FIBRO} fibroblasts *in vitro* relative to nuclear DNA quantified via qPCR (n = 6 controls; n = 8 Twinkle^{FIBRO}). **(B)** The long-range PCR products derived from mtDNA in dermal lysates *in situ* reveal an accumulation of deletions (red circles). The whole genome of treated and untreated Twinkle^{FIBRO} mice was replicated and made visible using Ethidium bromide under UV light. **(C)** Representative OxPhos subunits of Twinkle^{FIBRO} fibroblasts *in vitro* and **(D)** *in situ* in western blots. The graphs depict the relative change of the band's intensity for the respective complex relative to the mean of controls.

5.1 The K320E Twinkle mutation leads to mtDNA deletions *in vivo* and mtDNA depletion *in vitro*

Upon activation of K320E-Twinkle through Tamoxifen treatment, mtDNA deletions accumulate in the dermis of Twinkle^{FIBRO} mice. We analysed whole DNA genome in a long-range PCR to assess the panel of deletions in Twinkle^{FIBRO} mice. The resulting shortened mtDNA copies are visible as shorter PCR products (Figure 23 B). This differs from Twinkle^{FIBRO} fibroblasts *in vitro*, where mtDNA deletions are barely detectable (data not shown). Due to proliferation and

replication advantage of denser mtDNA in Twinkle^{FIBRO} fibroblasts under cell culture conditions[138], there is a significant decrease in mtDNA copy number, reducing the relative mtDNA content to 28% of nucDNA (p=0.0004, mean ± SD: 0.28 ± 0.16) (Figure 23 A). Conversely, we exclude that mtDNA is depleted in post-mitotic fibroblasts *in situ* (mean of controls ± SD: 1,89 ± 2,48 vs. mean of mutants ± SD: 1,77 ± 1,23) (Figure 27A). These results indicate that mtDNA deletions accumulate *in situ*, and mtDNA is depleted in fast-proliferating Twinkle^{FIBRO} fibroblasts *in vitro*.

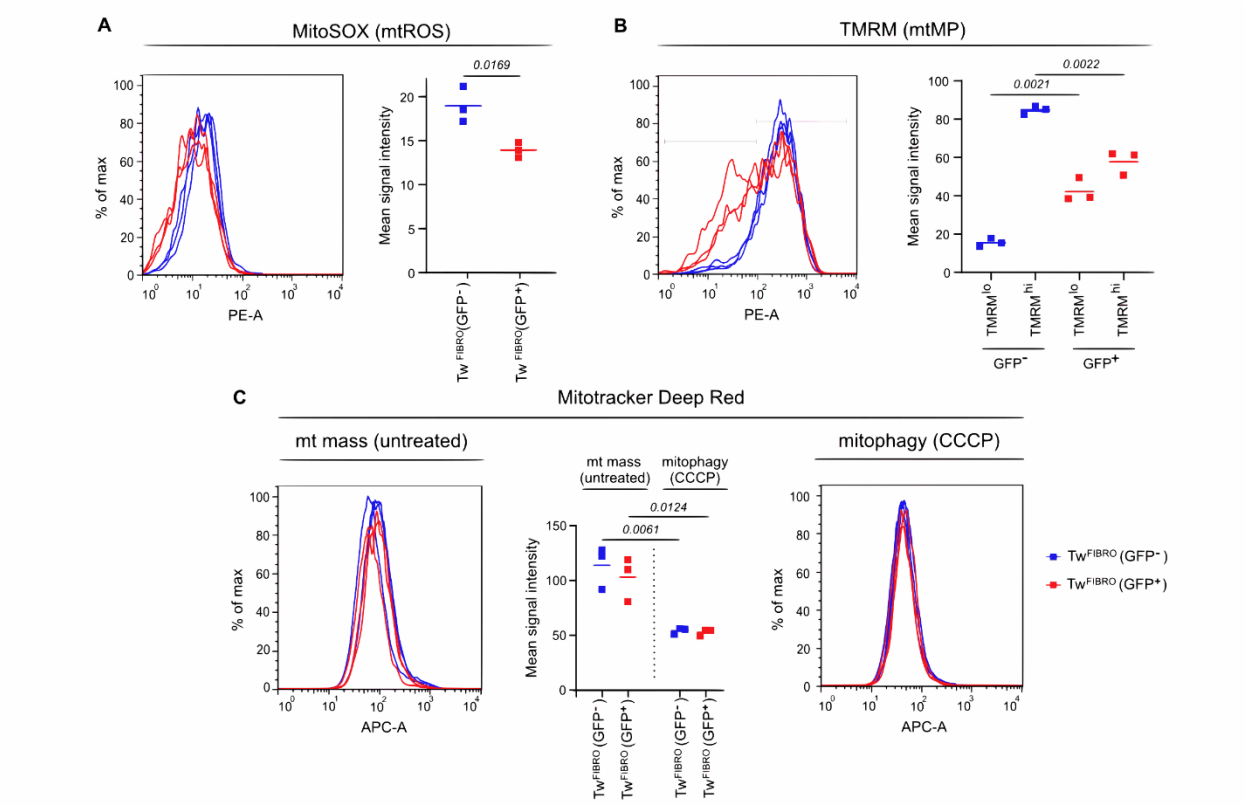

Figure 24: Analysis of mitochondrial parameters in flow cytometry. (A) Detection of mtROS production in Twinkle^{FIBRO} fibroblasts by MitoSOX staining (n = 3 mice per group). **(B)** mtMP was measured via TMRM staining, and GFP$^+$ vs GFP$^-$ fibroblasts derived from Twinkle^{FIBRO} mice were compared. Within these groups, the proportion of TMRM^{low} and TMRM^{high} populations are represented. **(C)** Analysis of mitochondrial mass in GFP$^+$ compared to GFP$^-$ fibroblasts via Mitotracker Deep Red. The mitochondrial mass "untreated" serves as a control for mitophagy induction ("CCCP"; treated with low dose = 10 µM). Each of the overlaid histograms and quantifications is represented. Three mice per group were used. For MitoSOX and TMRM, the PE-A channel was chosen for Mitotracker Deep Red APC-A.
Abbreviations: CCCP: carbonyl cyanide m-chlorophenyl hydrazone.

5.2 Mitochondrial ROS and mitochondrial membrane potential, but not OxPhos stoichiometry, are reduced in Twinkle^{FIBRO} fibroblasts

To understand the effect of mtDNA deletions and depletion on mitochondrial function, we investigated the expression of OxPhos complexes. Immunoblots of OxPhos complex stoichiometry revealed no direct impairment due to mtDNA deletions in Twinkle^{FIBRO} mice since the expression was not altered in a steady state (Figure 23 C). Similarly, OxPhos abundance

was also not affected in Tamoxifen-treated Twinkle^{FIBRO} fibroblasts (Figure 23 D) although we observed significant mtDNA depletion. Since these subunits likely represent the assembled complexes, we can conclude that the RC is not affected by mtDNA deletions in Twinkle^{FIBRO} mice and mtDNA depletion in Twinkle^{FIBRO} fibroblasts. Next, we performed flow cytometry experiments to analyse other important mitochondrial parameters. We gated GFP^{+} populations derived from mutant mice ("GFP^{+}") and compared them to cells that do not express GFP ("GFP^{-}"), serving as controls. Mitochondrial derived Reactive Oxygen Species (mtROS) levels, detected via MitoSox staining intensity, were significantly reduced in mutant cells (Figure 24 A). We measured the mitochondrial membrane potential (mtMP) of Twinkle^{FIBRO} fibroblasts using Tetramethylrhodamine methyl ester (TMRM) staining. We found a significant shift in mtMP, with an increased proportion of cells in the TMRM^{low} population ($p=0.0021$, mean ± SD: 15.47 ± 2.72 in GFP^{-} vs. 42.20 ± 6.16 in GFP^{+}), and a corresponding decrease in the TMRM^{high} population ($p=0.0022$, mean ± SD: 84.53 ± 2.27 in GFP^{-} vs. 57.77 ± 6.22 in GFP^{+}) (Figure 24 B). The relative redistribution between TMRM^{low} and TMRM^{high} gates indicates decreased mtMP. Lastly, Mitotracker Deep Red dye was used to assess mitochondrial mass ("untreated"), which was not altered in GFP^{+} fibroblasts compared to GFP^{-} fibroblasts (Figure 24 C).

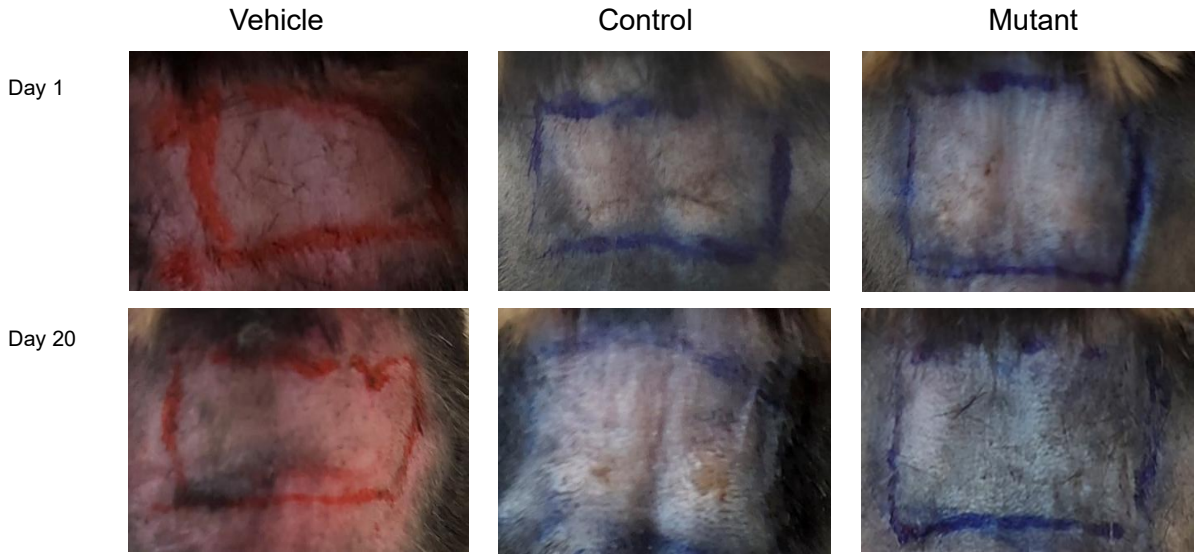

Figure 25: Photographs of the neck area of Vehicle (n = 4), controls (n = 7) and Twinkle^{FIBRO} mice (n = 8) during Bleomycin injections. Injections were administered at the two lower corners of the 1.5 × 1.5 cm square area, directed toward the centre of the square, with the injection sites alternating daily. The vehicles were treated with 0,9% NaCl solution. Due to the hair growth cycle, black spots may appear, for instance, on the vehicle on day 20.

5.3 The fibrotic phenotype is dampened in Bleomycin-treated Twinkle^{FIBRO} mice

To further analyse the effect of the Twinkle mutation amid chronic inflammation, we induced fibrosis *in vivo*. After ten days of Bleomycin injections, macroscopic inspections revealed an eczematous appearance and stiff texture in mutant and control mice. After four weeks, the

inflammatory phenotype was more pronounced in control mice, where the skin appeared more pruritic and irritated, displaying features of fibrotic tissue (Figure 25).

5.4 Morphometric analysis reveals an attenuated fibrosis in Bleomycin-treated Twinkle^{FIBRO} mice

Macroscopically, mutants had a reduced fibrotic appearance in the predefined area. To prove this impression microscopely, tissue after four weeks of Bleomycin treatment was assessed histologically. An overview staining with Trichrom-Masson enables insight into cell abundance and ECM deposition. Reduced collagen production can be observed in Twinkle^{FIBRO} mice, which is noticeable by less intense green staining than controls (Figure 26 B). Furthermore, a decrease in subcutaneous fat can be noted. The morphometric analysis was performed using HE sections. Thickness in Twinkle^{FIBRO} mice was significantly reduced over twofold compared to controls ($p=0.0281$, mean ± SD: 3.53 ± 0.61 mm in controls vs. 2,70 ± 0.37 mm in mutants) (Figure 26 C and D). Additionally, the width of the fibrotic region was significantly reduced ($p=0.0069$, mean ± SD: 5,65 ± 1.36 mm in controls vs. 3,90 ± 1.38 mm in mutants). Collagen analysis was corroborated with Sirius Red imaging to validate these results further. Under polarised microscopy, collagen fibres were counted and normalised to the total dermal area. This revealed fewer collagen fibres in Twinkle^{FIBRO} mice than in controls (Figure 26 K). This is consistent with collagen 1 expression, significantly reduced in Twinkle^{FIBRO} mice (Figure 26 H and I), concomitant with a diminished Col1 mRNA expression (Figure 26 J). This indicates that mtDNA deletions seem to affect fibrosis development in Twinkle^{FIBRO} mice.

We then scrutinised the structure of collagen deposition via Second Harmonic Generation Microscopy (SHG). This permits the visualisation of collagen density and quantitative assessment of collagen organisation with Gray Levels Co-occurrence Matrix (GLCM)[139]. The mean signal intensity, referring to the density of collagen molecules, showed a subtle but insignificant decrease in mutants while demonstrating the induction of fibrosis compared to vehicle mice (Figure 26 E-G). However, we could not observe any variation in entropy, an index for the random distribution of pixel intensity within an image. These results support our observation that fibrosis development is milder in Twinkle^{FIBRO} mice, but the organisation is not severely affected, neither in controls nor in mutants.

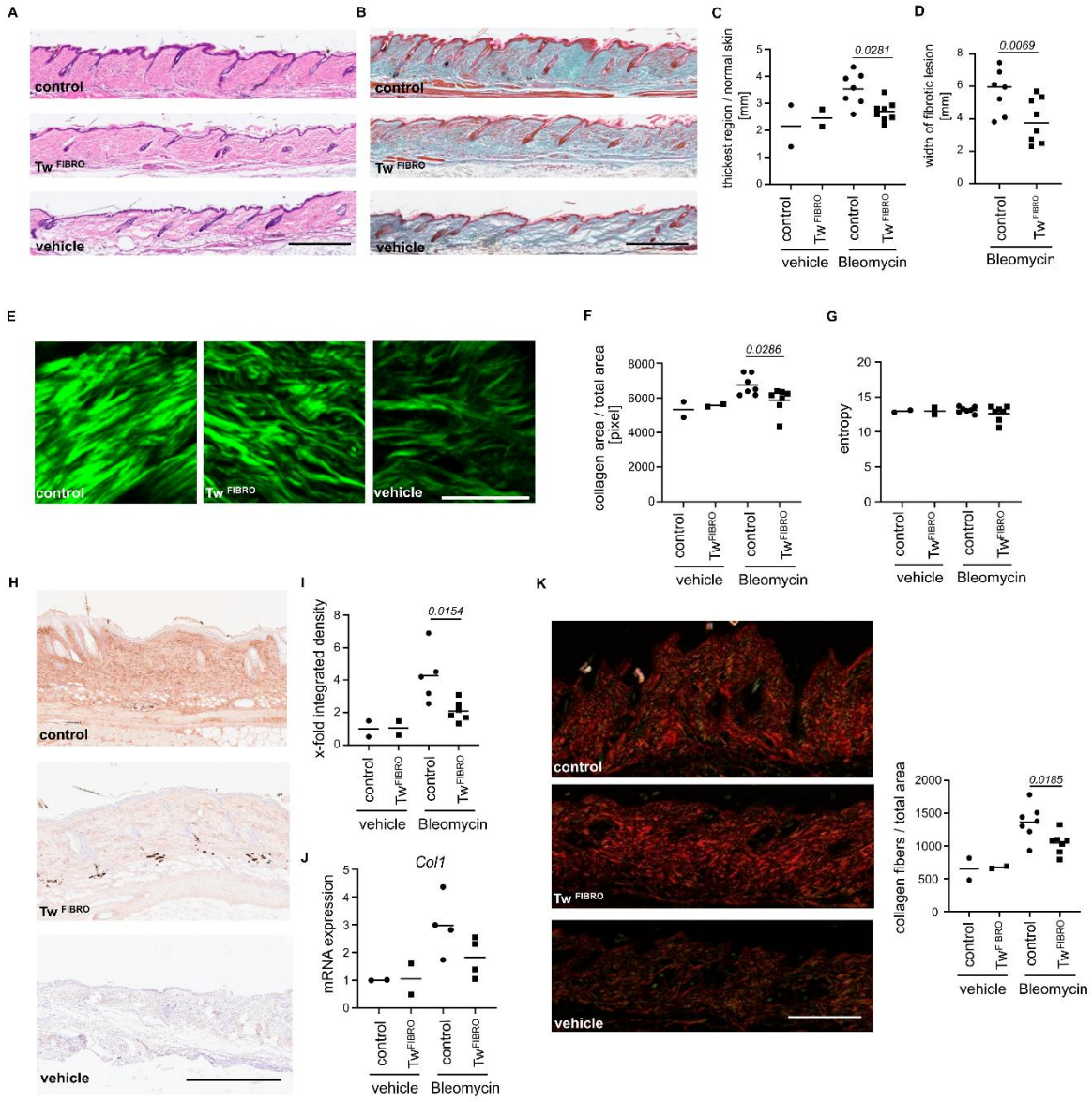

Figure 26: Attenuated fibrotic response in Twinkle^{FIBRO} mice. (A) HE staining (purplish blue: nucleus; pink: cytoplasm and tissue) and **(B)** TM staining illustrating dermal thickness and collagen deposition in the dermis (blue/green: collagen; red: myosin, keratin; pink: nucleus; brown: cytoplasm); (n = 4 vehicle (NaCl), 2 per genotype; n = 7 control mice; n = 8 Twinkle^{FIBRO} mice. Scale bar: 500 µm). Both stainings were photographed on the Slide Scanner (Hamamatsu S360). **(C)** Measurement of dermal thickness as the ratio of the centre of the fibrotic lesion or the thickest region to normal skin (n = 4 vehicle-treated mice, 2 per genotype; n = 7 control mice; n = 8 Twinkle^{FIBRO} mice). **(D)** Width of fibrotic lesion measured in mm (n = 7 control mice; n = 8 Twinkle^{FIBRO} mice). **(E)** Second Harmonic Generation images showing collagen fibres, enabling measurement of **(F)** collagen area per total area and **(G)** entropy (n = 4 vehicle-treated mice, 2 per genotype; n = 7 control mice; n = 8 Twinkle^{FIBRO} mice, scale bar: 20 µm). **(H)** Col1 immunohistochemistry (Scale bar: 500 µm)**. (I)** Integrated density of Col1 protein expression in immunohistochemistry and **(J)** mRNA expression (n = 4 vehicle (NaCl), 2 per genotype; n = 4-5 control mice; n = 4-6 Twinkle^{FIBRO} mice). **(K)** Quantification of total collagen fibres relative to the total area in Sirius Red stained samples visualised under polarised microscopy (n = 4 vehicle (NaCl), 2 per genotype; n = 7 control mice; n = 8 Twinkle^{FIBRO} mice. Scale bar: 200 µm). The figure was adapted from Mitochondrial DNA mutations attenuate Bleomycin-induced dermal fibrosis by inhibiting differentiation into myofibroblasts, by Reiter et al., Matrix Biology in 2024.

5.5 Deletions accumulate in Bleomycin-treated mice without impacting mtDNA copy number

To elucidate the role of the K320E-Twinkle mutation in dermal fibroblasts in chronic inflammation, we conducted analysis on mtDNA content and mitochondrial function. As mentioned, our results showed that mtDNA deletions accumulate in unchallenged Twinkle^{FIBRO} dermis. Since fibroblasts proliferate in response to fibrotic stimuli[140], we hypothesised that increased mtDNA replication during cell division may promote the clonal expansion of deleted mtDNA due to their potential replicative advantage[138,141]. We show that mtDNA deletions increase when Twinkle^{FIBRO} fibroblasts are challenged, particularly at 4361 bp and 2027 bp) (Figure 23 B). We further demonstrated that mtDNA deletions 1, 3 and 17, accumulate in Bleomycin-treated Twinkle^{FIBRO} mice[142]. While mtDNA deletions increase upon fibrotic conditions, total mtDNA copy number remained unchanged (Figure 23 A).

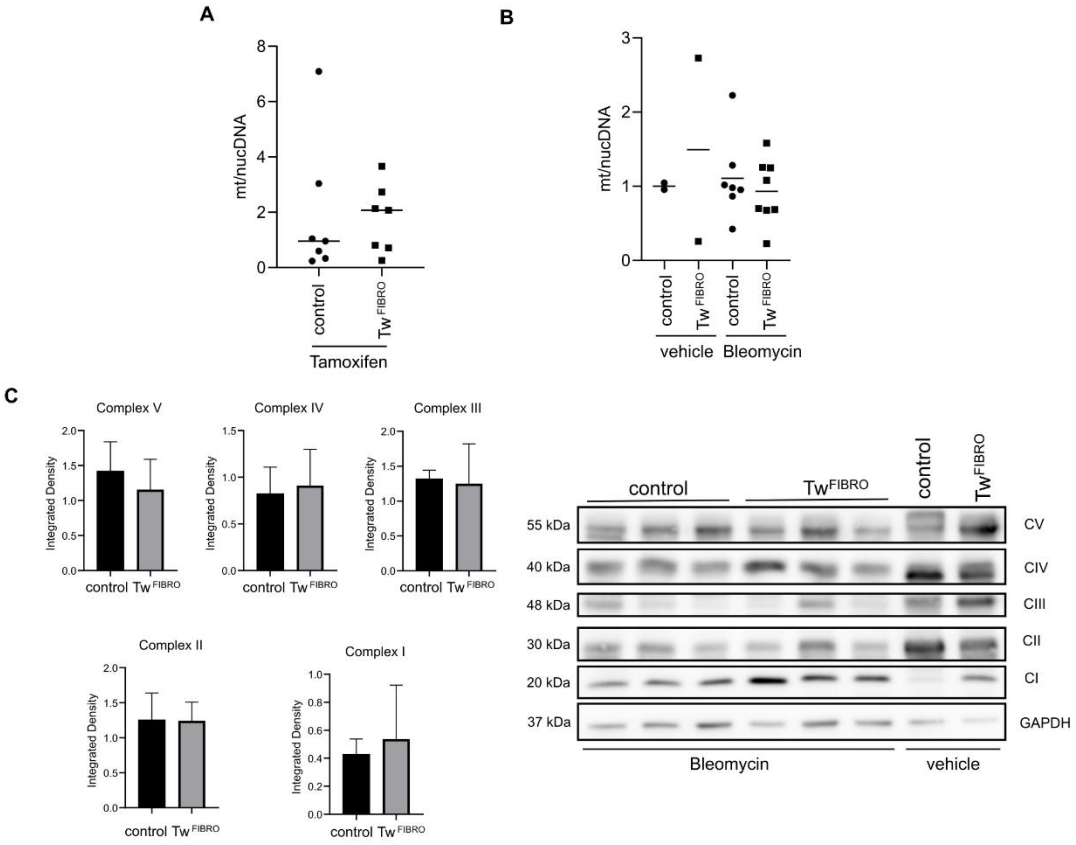

Figure 27: Copy number of mtDNA and Oxphos stoichiometry are not affected in Bleomycin-treated Twinkle^{FIBRO} mice. (A) Twinkle^{FIBRO} mice were fed with Tamoxifen for 5 weeks. 7 mice per group were used. (**B)** Bleomycin-treated Twinkle^{FIBRO} mice (n = 4 vehicle; n = 7 controls; n = 8 Twinkle^{FIBRO}). The relative mtDNA copy number was calculated by comparison to nuclear DNA, using 2-DDcT. The graphs were designed using Prism. **(C)** Subunits of complex I (NDUFA9), II (SDH), III (UQCRC2), IV (mtCO3) and V (ATP5A) are depicted. Data are represented as means. For the comparison, the unpaired t-test was performed using Prism. GAPDH was used as a loading control.

5.6 OxPhos complex stoichiometry was not altered in Twinkle^{FIBRO} mice

We questioned whether an increased rate of mtDNA deletions affects OxPhos in Twinkle^{FIBRO} mice. All samples showed a reduced expression of OxPhos complexes compared to the NaCltreated vehicle, except for complex I, which was upregulated in all Bleomycin-treated mice. This trend was higher in mutants than controls, although not significantly (Figure 27 C). The expression of the remaining complexes within the Bleomycin samples showed no difference. We conclude that fibrotic development attenuates OxPhos stoichiometry independently of mtDNA deletions.

5.7 Proliferation and apoptosis are not altered in Twinkle^{FIBRO} mice

Next, we analysed potential alterations of fibroblast functions underlying the attenuated fibrosis in Twinkle^{FIBRO} mice. First, we hypothesised a potential imbalance between proliferation and apoptosis in the context of mtDNA deletions and a subsequent altered fibrotic development as these functions rely on intact mitochondria. The proliferation and apoptosis rate was assessed depicting ki-67 positive nuclei and caspase-3 positive cytosol of fibroblasts, respectively (Figure 28 C-F). Fibrotic areas showed an increased number of Ki-67 positive cells; however, no significant difference in dermal proliferation and apoptosis was observed between Bleomycin-treated control and mutant mice (Figure 28 C-E). Ultimately, proliferation and apoptosis rates are similar after four weeks of Bleomycin treatment in Twinkle^{FIBRO} mice.

5.8 Senescence is not induced in fibrotic Twinkle^{FIBRO} dermis

Concordantly to overall unremarkable levels of proliferation and apoptosis, we speculated that the attenuated fibrosis in mutants is related to a quiescent status of Twinkle^{FIBRO} fibroblasts, leading to reduced collagen production and secretion of pro-fibrotic cytokines. We investigated whether senescence occurs in a steady state both *in vitro* and *in situ*. To assess this process, we used chromogenic substrate 5-bromo-4-chloro-3-indolyl-β-D-galactopyranoside (x-gal), targeting β-galactosidase enzyme activity, which is specific for the senescence process[143]. However, no senescent cells were detectable either in fibroblasts *in vitro* (Figure 28 B) or Twinkle^{FIBRO} mice *in situ* (Figure 28 A). This indicates that mtDNA deletions and depletion do not induce senescence in this mouse model.

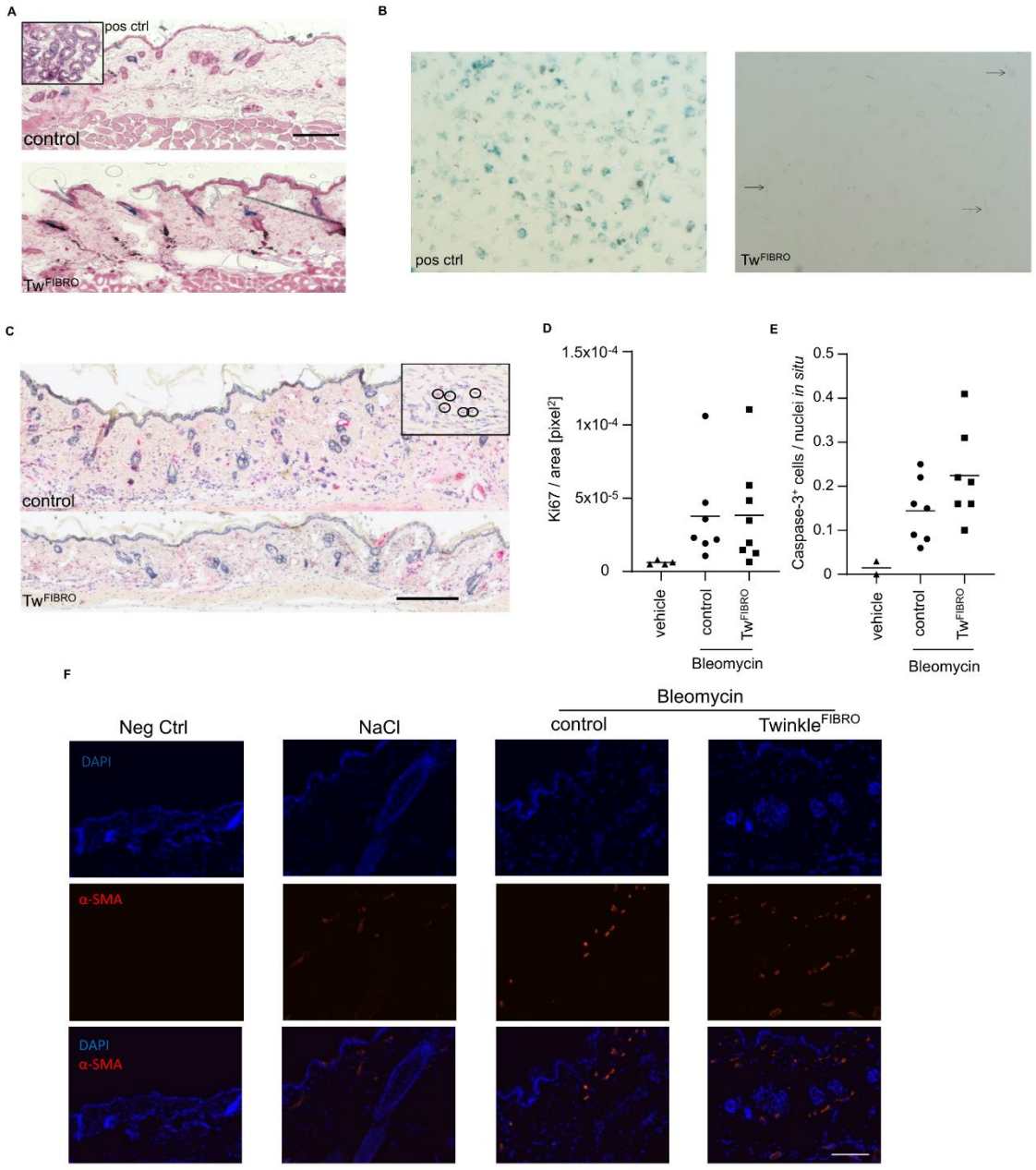

Figure 28: Senescence, proliferation and apoptosis rate are not impaired in Bleomycin-treated Twinkle^{FIBRO} dermis. (A) x-gal staining in Twinkle^{FIBRO} dermis *in situ*. The upper panel displays the skin of control mice, while the lower panel shows the skin of Twinkle^{FIBRO} mice. Blue staining represents elevated βgalactosidase activity, observed exclusively in the caput epididymis tissue of WT-type mice used as a positive control (inset in the upper left panel, 20x magnification). Scale bar 10 × 100 µm. **(B)** x-gal staining in in Twinkle^{FIBRO} fibroblasts *in vitro*. Wild-type fibroblasts were irradiated with 20 Gray as a positive control and incubated for 7 additional days (left). Arrows indicate fibroblasts (right); however, none are blue. **(C)** Proliferation assessment using ki-67 detection. Counted were those cells containing purplish nuclei, indicating the presence of ki-67 as shown in the upper right panel (nuclei=blue; ki-67=pink). Scale Bar 250 µm. The epidermis, the skin layer with the highest cell turnover, was a positive control. **(D)** Quantitative analysis showed positive ki-67 cells normalised to nuclei and (E) the number of apoptotic cells normalised to DAPI. All graphs were made on Prism. **(F)** Caspase-3 was detected throughout immunofluorescence staining. Again, the rich apoptotic epidermis served as a positive control. Red fluorescent cytosols indicate an apoptotic process. 20x Magnification, Scale Bar 100 µm.

5.9 Autophagy is unaffected in Twinkle^{FIBRO} mice

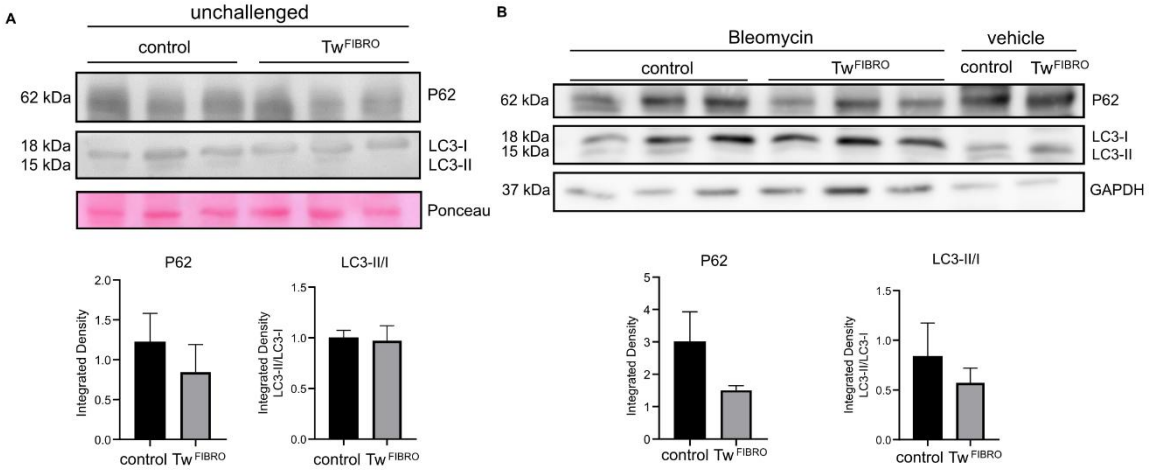

Figure 29: Autophagy is not affected in Twinkle^{FIBRO} dermis. (A) Immunoblots depicting autophagic markers in a steady state. Mice were fed with Tamoxifen for 5 weeks; 3 per group were used. For LC3 analysis, LC3-II was divided by LC3-I and values were normalised to controls. Ponceau served as a loading control. **(B)** Autophagy biomarkers in fibrotic Twinkle^{FIBRO} dermis. 3 mice per group were taken. LC3 values were normalised to the controls. GAPDH was used as a loading control. Graphs were made using Prism.

To explore fibrosis modulators, we assessed autophagy, which can potentially disrupt tissue homeostasis if altered. To analyse autophagic activity, we investigated P62 and LC3-II/I in immunoblotting, two key components of macroautophagy, and used to determine autophagic flux[144]. In a steady state, a slight but not significant, reduction of P62 in mutants compared to controls was observed (Figure 29 A), while the LC3 turnover remains unchanged (Figure 29 A). To further investigate whether mtDNA depletion can affect mitophagy, we analysed mitochondrial mass using Mitotracker Deep Red Dye in flow cytometry. To induce mitophagy, Twinkle^{FIBRO} fibroblasts were treated with a low carbonyl cyanide m-chlorophenyl hydrazone (CCCP) dose for 12 hours. This procedure was successful, as shown in the reduced mitochondrial mass degraded by mitophagy compared to untreated controls (p=0.061, 114.0 ± 19.34 vs. 54.27 ± 2.86 in GFP^-; p=0.0124, 103.3 ± 19.97 vs. 52.9 ± 2.95 in GFP^+; untreated vs. CCCP-treated) (Figure 24 C). However, the degradation was similar between Twinkle^{FIBRO} and control fibroblasts, indicating that mitophagy is likely not impaired upon mtDNA depletion.

Bleomycin-treated mice exhibited a significant reduction of P62 expression compared to the vehicle, whereas the mutant's P62 expression was halved compared to controls (Figure 29 B). However, the lack of corresponding LC3 conversion to the decrease of P62 in fibrotic Twinkle^{FIBRO} dermis makes a significant upregulation of autophagy upon an increased rate of mtDNA deletions unlikely.

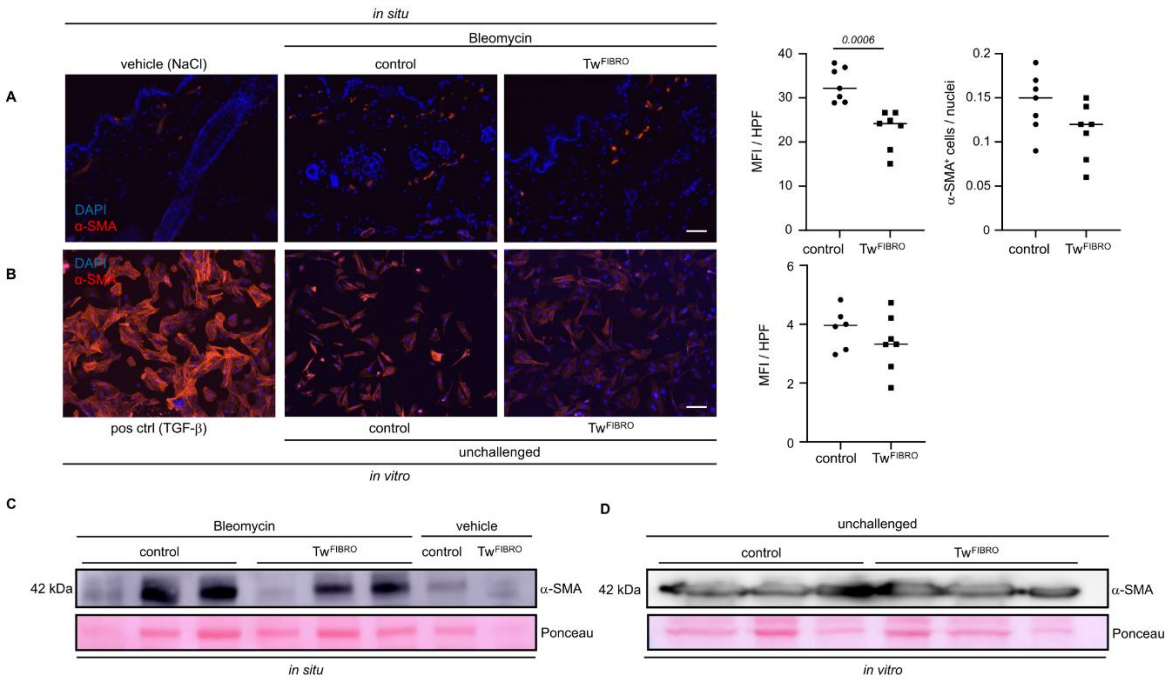

Figure 30: Impaired differentiation of Twinkle^{FIBRO} to myofibroblasts protects against fibrosis progression. **(A)** Immunofluorescence staining of α-SMA in Bleomycin-treated Twinkle^{FIBRO} mice *in situ* (scale bar 10 × 100 µm) and **(B)** sorted *in vitro* Twinkle^{FIBRO} fibroblasts. TGF-β treated fibroblasts served as a positive control. Scale bar 100 µm, 10x magnification. For each sample, the mean fluorescence intensity (MFI) of selected myofibroblasts was averaged across high-power fields (HPF) with background noise subtracted; additionally, the number of α-SMA+ cells was normalised to the number of DAPI+ nuclei (n = 6–7 controls; n = 7 Twinkle^{FIBRO}). Graphs were made on Prism. **(C)** Immunoblot showing α-SMA protein expression in Bleomycin-treated Twinkle^{FIBRO} mice compared to controls (n = 3 per group) and **(D)** in unchallenged Twinkle^{FIBRO} fibroblasts *in vitro*. For both, Ponceau staining was used as the loading control.

5.10 Differentiation into myofibroblasts is restricted in fibrotic Twinkle^{FIBRO} dermis

Lastly, we investigated whether an affected fibroblast-to-myofibroblast transition may be involved in the attenuated phenotype in Twinkle^{FIBRO} mice. For this purpose, we visualised the α-smooth muscle actin (α-SMA) intensity in immunofluorescence staining, reflecting the abundance of stress fibres and correlating with the extent of myofibroblast activity (Figure 30 A and B). We observed that Twinkle^{FIBRO} fibroblasts showed a reduction *in vitro* (Mean ± SD: 3,85 ± 0.70 in controls vs. 3,35 ± 0.96 in mutants) (Figure 30 B), consistent with no relevant difference in α-SMA expression in western blots (Figure 30 D). Nevertheless, α-SMA intensity was reduced *in situ* (p=0.006, mean ± SD: 33.02 ± 3.85 in controls vs. 22,77 ± 4.41 in mutants) (Figure 30 A and C). Concordantly, the quantification of α-SMA+ cells (α-SMA^{+}) in the fibrotic area was also reduced (mean ± SD: 0.14 ± 0.03 in controls vs. 0.11 ± 0.03 in mutants) (Figure 30 A). These results suggest that the K320E-mutation substantially attenuates α-SMA expression.

6. Discussion

In this study, we induced the K320E-Twinkle mutation in a mouse model that mimics "physiological" ageing, which leads to mtDNA mutations in fibroblasts. The results reveal previously unrecognised effects of mtDNA deletions and depletion in dermal fibroblasts and highlight the role of mutation load in modulating the development of diseases, such as chronic inflammation, including potential protective outcomes.

Under cell culture circumstances, the compromised mtDNA replication machinery could not keep pace with the artificially rapid cell proliferation, leading to mtDNA depletion (28% copy number compared to nuclear DNA), a previously described phenomenon[122]. This is also applicable in a mouse model developed by our working group, where the Twinkle mutation is expressed in the highly proliferative keratinocytes *in situ*[84].

MtDNA copy number has a significant clinical relevance, particularly in the onset of the socalled mtDNA depletion syndromes, which are autosomal recessive diseases characterised by abnormal tissue-specific mtDNA depletion[2]. Specifically, the degree of depletion correlates with disease severity, as seen in Leber's hereditary optic neuropathy, where low mtDNA copy number is linked to greater disease penetrance and earlier vision loss[145,146]. Conversely, higher copy number often indicate better outcomes, for example, due to compensatory enhanced mtDNA biogenesis in response to mutations[147,148]. Nevertheless, these mechanisms can be tissue-specific[149], and there is limited data on skin and associated mitochondriopathies. Most mtDNA depletion syndromes occur with OxPhos deficiency, but this study's mouse model shows otherwise. MtDNA depletion and reduced mitochondrial membrane potential (mtMP) did not impair OxPhos, and low levels of mitochondrial-derived reactive oxygen species (mtROS) indicate minimal mitochondrial damage. These parameters were similar in other cellspecific Twinkle mouse models, such as in keratinocytes or chondrocytes[84,150], contrasting with those showing severe mitochondrial damage and increased oxidative stress markers[2,151,152]. Using Mitotracker Deep Red in flow cytometry, we also demonstrate that mitochondrial mass and mitophagy induction were not affected in Twinkle^{FIBRO} fibroblasts, likely ruling out a significant impairment of mitochondrial biogenesis and degradation[112]. Overall, these results offer valuable insights into the effect of mtDNA depletion in skin fibroblasts, without necessarily leading to severe alterations of mitochondrial function.

Notably, inducing the K320E-Twinkle mutation in post-mitotic fibroblasts in a steady state does not cause a spontaneous phenotype or specific symptoms in mice[142]. Wounds in Twinkle^{FIBRO} mice healed at a rate like controls, likely due to functional epidermal keratinocytes closing the wound efficiently, compensating for fibroblast deficits. Despite an increased rate of mtDNA deletions in Twinkle^{FIBRO} mice, especially when challenged with Bleomycin-induced fibrosis, the

overall level of deletions remained discrete and did not result in compromised tissue function, aligning with ageing-related mtDNA mutations that typically have negligible effects on tissue. However, we stress that mtDNA deletions are difficult to target in tissue homogenates due to high mosaicism (successful induction of the K320E-Twinkle mutation in 25-30% of cells), meaning the true amount of deletions may be higher than detected by Long-Range PCR[1,17]. Of note, despite that mice used in the experiments were middle-aged (27-30 weeks) and may have accumulated physiological mtDNA deletions, these are reported to remain limited at this age, as such increases in post-mitotic tissues typically occur after 16 months[153]. We then showed that mtDNA deletions did not alter OxPhos stoichiometry in Twinkle^{FIBRO} mice, which matched findings from Twinkle^{FIBRO} fibroblasts *in vitro* showing mtDNA depletion. However, OxPhos abundance was mildly reduced in Bleomycin-treated mice, aligning with MTCO1 downregulation in fibroblasts derived from Morphea patients[142] and decreased TFAM in Systemic Sclerosis (SSc) patients[24]. This reduction in OxPhos protein expression in Bleomycin treated mice was genotype-independent, suggesting that neither mtDNA deletions nor fibrosis had exceeded a pathological threshold that induces severe mitochondrial damage and respiratory chain (RC) impairment[25]. Several studies have investigated the residual OxPhos activity and specific biochemical thresholds in different cell types associated with various mitochondrial disease mutations. It is estimated that OxPhos impairment occurs with 60-90% of large mtDNA pathologies, whereas high-energy demanding tissues exhibit lower thresholds[3,149,154]. A review by Smith et al. suggests biochemical thresholds for complexes I and IV in dermal fibroblasts at 50-90%, and over 90% in complexes III and V[6]. However, other disease-related factors can influence these thresholds, such as inflammatory triggers, like fibrosis. Nevertheless, RC integrity alone may not fully capture mitochondrial dysfunction, highlighting the need to investigate other parameters such as mitochondrial dynamics and metabolism.

It is essential to nuance the difference between mitochondrial and mtDNA damage since deletions do not necessarily impair OxPhos or mitochondrial function. Accumulating mtDNA mutations are tolerated to a certain extent without generating harm; in Twinkle^{FIBRO} mice, the remaining intact mtDNA likely is sufficient to generate the synthesis of RC subunits.

Several studies have highlighted the role of mitochondria in fibrotic and autoimmune diseases. In idiopathic pulmonary fibrosis and systemic sclerosis (SSc)-associated interstitial lung disease, lung tissues exhibit elevated mtROS, mtDNA damage, and impaired RC activity[155,156]. Likewise, in SSc fibroblasts, free circulating mtDNA is a possible trigger of inflammatory TLR9 signalling[157]. In systemic lupus erythematosus, impaired mitophagy and fission increase mitochondrial mass in T-cells cause progressive dysfunction[158]. These examples suggest a pathophysiology involving severe mitochondrial damage, RC dysfunction, and altered

mitochondrial dynamics as underlying causes of excessive inflammatory responses. Conversely, in Bleomycin-treated Twinkle^{FIBRO} mice, we demonstrate that fibrosis is attenuated in the presence of low levels of mtDNA deletions. This is also the case in dermal Twinkle^{FIBRO} fibroblasts *in vitro*, which exhibit an anti-inflammatory and anti-fibrotic mRNA expression profile, such as impaired contractility[142]. This study is the first to describe a putative protective effect of mtDNA deletions in fibrosis development in the skin.

In light of mitochondrial damage UV-A causes in the context of phototherapy[159,160], our results invite to question a possible underlying mechanism behind UV-A-induced mtDNA deletions affecting skin fibrosis through inflammatory modulation. Phototherapy is widely used to ameliorate skin fibrosis in autoimmune diseases like SSc, Morphea or sclerodermiform graftversus-host diseases[21]. The pathophysiology is complex, but there is emerging evidence that this treatment entails both the downregulation and upregulation of pro-fibrotic and anti-fibrotic pathways, respectively[75,161]. Furthermore, in UVA-1 irradiated primary fibroblasts, reduced mRNA expression of TGF-β isoforms and increased collagen-degrading MMPs were shown, both associated with fibrosis attenuation, likely due to IL-1β overexpression (a proinflammatory cytokine), which applies to the mouse model used in our study[142]. To the best of our knowledge, the correlation between UV-induced mtDNA deletions and fibrosis amelioration has not been previously studied and deserves further exploration.

Some studies support the concept of mitohormesis, where mild mitochondrial stress activates protective compensatory mechanisms[162,163]. For instance, MLCK1-mutant mice with reduced ubiquinone synthesis exhibit elevated mitochondrial ROS but decreased stress in other compartments, resulting in extended lifespan[151]. Similarly, glucose restriction in *C. elegans* increases mitochondrial ROS and lifespan, an effect blocked by antioxidants[164]. This concept aligns with the observed attenuated inflammation in K320E-Twinkle mice, where the mtDNA deletions might activate compensatory stress responses without tipping the balance toward disease. However, this concept remains hypothetical and lacks mechanistic validation.

One of the key findings in this study is the attenuated differentiation of Twinkle^{FIBRO} fibroblasts both *in vitro* and *in situ*, indicated by lower levels of α-SMA-positive cells in immunofluorescence staining and protein expression in immunoblotting. We hypothesise that mtDNA depletion is involved in the reduced capacity of Twinkle^{FIBRO} fibroblasts to differentiate *in vitro*, as reduced levels of mtDNA copy number may hinder the process, as observed in Twinkle keratinocytes and chondrocytes[84,150]. Additionally, decreased levels of mtROS and mtMP in Twinkle^{FIBRO} fibroblasts may contribute to this restricted differentiation, as lower mtMP and ROS levels have been associated with reduced fibrosis and myofibroblast formation through NRF2-signalling[152,165,166].

Reduced α-SMA expression in Twinkle^{FIBRO} mice, correlating with myofibroblast activity, likely explains the attenuated fibrosis and offers the first evidence for this impairment related to accumulating mtDNA deletions. Indeed, mitochondria are fundamental in myofibroblast activity. Recent studies have described that the proper activity and distribution of mitochondria in alveolar tissue play essential roles in differentiation, sufficient active myofibroblasts generation, and functionality, including migration and contraction[167].

The decreased number of α-SMA-positive myofibroblasts in fibrotic skin prompted an investigation on whether mtDNA deletions affected apoptosis or proliferation, influencing myofibroblast quantity. *In vitro* results, such as reduced mtMP and reduction of TGF-β expression (Reiter et al.), both known to increase apoptosis susceptibility in myofibroblasts through pro-apoptotic BAX (a pro-apoptotic BCL-2 family protein) translocalisation and IL-1β stimuli, raised the possibility of increased apoptosis reducing myofibroblast abundance under the K320E-Twinkle mutation[70,168,169]. However, apoptosis rates were not significantly altered *in situ*, suggesting that mitochondria-mediated cell death is not a major driver of the mutant skin phenotype. Likewise, proliferation was not altered in fibrosis or wound healing[142]. However, since these analyses reflect single timepoints and transient effects on apoptosis or proliferation during early inflammatory phases of fibrosis (i.e. within the first two weeks of Bleomycin treatment) cannot be excluded[170].

Myofibroblast quantity can significantly impact the extent of fibrosis, but it is not the sole determinant. While the number of myofibroblasts correlates with disease severity in SSc, it does not necessarily relate to the extent of reticular hyalinised collagen[171]. Notably, the distribution of myofibroblasts accounting for distinct roles in the dermis, varies; SSc myofibroblasts are more abundant in the lower reticular than in the papillary dermis[172,173]. Shook et al. highlighted the importance of myofibroblast subsets heterogeneity, as different populations of mesenchymal cells vary in terms of ECM production, proliferation, and migration, affecting tissue repair differently[174]. For instance, in Bleomycin-treated wild-type mice, there is a significant increase in CD29-expressing fibroblasts, massively contributing to collagen deposition. Conversely, those containing adipocyte precursor cell surface markers, which are more abundantly involved in matrix cross-linking, are present in fewer numbers—a pattern also observed in wound beds of aged mice. This invites to study the dynamics of certain fibroblast sub-populations further to gain deeper insights into myofibroblast distribution, potentially affecting inflammatory processes.

Studies have reported that TGF-β-induced autophagy promotes fibroblast differentiation and collagen production, supporting our results of downregulated P62 in Bleomycin-treated samples[175]. Furthermore, blockage of autophagy in *Atg7* KO mice ameliorates

Bleomycininduced fibrosis[175]. While autophagy holds significant importance in fibrosis, its involvement in the attenuation observed in Twinkle^{FIBRO} mice is not decisive. The absence of LC3-conversion in both unchallenged and challenged Twinkle^{FIBRO} mice, along with unaltered mitophagy induction upon CCCP treatment in Twinkle^{FIBRO} fibroblasts, suggests that relevant alterations in autophagy and mitophagy are unlikely. Previous examinations in Twinkle mice from our laboratory unravelled a specific endosomal-mitophagy pathway that counteracts mitochondrial dysfunction and suggests alternative pathways for defective mtDNA removal[176]. However, considering the stable mitochondrial mass in Twinkle^{FIBRO} fibroblasts, we avoid making additional assumptions on mtDNA removal.

mtDNA deletions can trigger senescence. Particularly the mitochondrial dysfunctionassociated senescence (MiDAS), which displays a unique form of senescence-associated secretory phenotype (SASP) factors, is primarily driven by mitochondrial metabolites such as a low NAD+/NADH ratio, but also other alterations including mtDNA damage[177]. Conversely, mitochondrial depletion correlates with a reduced spectrum of senescence effectors and phenotypes, suggesting a complex and context-dependent regulation[178]. Although senescence and mitochondrial dysfunction have been widely described as intertwined in the ageing process and chronic diseases, this critical role has not been proven, neither in Twinkle^{FIBRO} fibroblasts *in vitro* nor *in situ*, indicating that mtDNA deletions or depletion do not likely induce senescence modulating myofibroblast differentiation in this context. In fibroblasts, the role of senescence is disputed and varies depending on tissue and disease. In skin, senescent cells can accelerate wound kinetics in mice through early SASP factors that induce myofibroblast differentiation. However, the absence of these cells impairs repair and may exacerbate fibrosis due to reduced secretion of matricellular proteins like CCN1[80,179,180]. Conversely, excessive or prolonged senescence has been linked to fibrosis progression in diseases such as SScInterstitial Lung Disease through sustained SASP signalling[181].

Further mechanisms may also be implicated in attenuated fibrosis observed in mutant mice. Fibrotic tissue has reduced oxygenation due to ECM deposition and poor vascularisation, promoting a metabolic shift toward glycolysis[70]. In post-radiotherapy fibrotic skin, wide-genome transcriptome profiling shows a clear up- and downregulation of glycolysis and fatty acid oxidation-associated genes, respectively[182]. Importantly, anaerobic glycolysis and specific metabolites such as phosphofructokinase-1, stimulate myofibroblast differentiation[135,183]. Furthermore, HIF-1α activation under hypoxia supports glycolytic metabolism and myofibroblast differentiation, while its inhibition reduces TGF-β mediated fibrosis in Bleomycininduced lung fibrosis models[184]. Although we do not expect aerobic glycolysis to be

affected in Twinkle^{FIBRO} mice, we cannot exclude the possibility that glycolysis shifts are involved in fibrosis development. While our study does not address this topic directly, it remains a consideration and warrants further research.

Finally, inflammatory cells and signals are drivers of fibrosis, with cells such as macrophages or neutrophils initiating myofibroblast differentiation. Classically activated macrophages (M1) and neutrophils promote myofibroblast activation through factors like IL-1, TNF-α, and ROS, while alternatively activated macrophages (M2) have anti-fibrotic properties (e.g., in the liver)[70]. Neutrophil extracellular traps increase differentiation autophagy-dependently, potentially perpetuating fibrosis in Bleomycin-induced lung fibrosis and in skin fibroblasts from Systemic Lupus Erythematosus patients[185,186]. Although we cannot exclude an interplay, inflammatory infiltrates remain considerable in Twinkle^{FIBRO} mice[142], which makes a major role for neutrophils and macrophages unlikely. Notably, the mutation in the Twinkle^{FIBRO} mice is fibroblast specific, limiting inflammatory signalling involving massive immune cell infiltration.
In Twinkle^{FIBRO} mice, subtle mtDNA damage correlates with a transcriptional downregulation of *il-6* and upregulation of *il-10*, corresponding to pro- and anti-inflammatory cytokines affecting differentiation[142]. Additionally, mRNA and protein levels of the pro-inflammatory cytokine IL-1β were paradoxically upregulated, which might also be involved in this process. IL-1β plays an ambivalent role in fibrosis and has been reported to inhibit TGF-β mediated differentiation to myofibroblasts, α-SMA, and Col1 expression, which supports our data[187]. Considering the proinflammatory profile in Twinkle^{FIBRO} fibroblasts[142], we hypothesise that mtDNA deletions are responsible for a downregulation of TGF-β and IL-6, both known to correlate with dermal thickness in fibrosis[42,188] and for the upregulation of IL-1β, all acting on fibroblasts in a cellautonomous fashion. Thus, mtDNA deletions mitigate the inflammatory response toward a profibrotic stimulus, leading to restricted SMAD3-dependant differentiation to myofibroblasts. These findings point to a cell-autonomous, protective role of mtDNA deletions against fibrosis. However, some studies present contrasting evidence. Zhou et al. described a TFAM KO mouse model where resulting mtDNA deletions and decreased mtDNA copy number made skin and lungs more sensitive to TGF-β, worsening fibrosis[24]. Nevertheless, this model displays severely damaged mitochondria, unlike Twinkle^{FIBRO} mice. Additionally, there is increasing evidence that mtDNA deletions are involved in systemic inflammation through downstream targets of TGF-β, such as FGF-21, a local and systemic messenger of mitochondrial dysfunction, shifting metabolic programming and inflammatory responses to sustain homeostasis[189]. FGF-21 has also been associated with fibrosis attenuation in the liver by regulating inflammatory factors such as IL-6, likely through a SMAD3-dependent mechanism[190,191].

This study unravels a potential protective role of fibroblasts in skin inflammation linked to accumulating mtDNA deletions. Through a reduced pro-fibrotic and pro-inflammatory signature, such as restricted differentiation to myofibroblasts, mtDNA mutations can confer a protective effect, provided they remain below a pathological threshold. The skin is an ideal organ for studying the impact of mtDNA deletions *in vivo* and depletion *in vitro*, due to its accessibility and a wide array of cells with different metabolic implications and energy requirements. The Twinkle^{FIBRO} mouse model, reflecting the physiological accumulation of mtDNA indels during ageing, offers a valuable platform for such investigations, contributing to our understanding of mitochondrial function in skin homeostasis.

7. Limitations

In the following, I will briefly discuss the methodological limitations of this study. I acknowledge that mtROS, mtMP, and mitophagy are indirect measurements of mitochondrial function. We could not assess mitochondrial functions directly since our attempts to measure oxygen consumption and TCA metabolites were unsuccessful due to insufficient tissue volume and GFP^+ sorted cells, which remained scarce in our samples. However, we do not believe the RC was affected since OxPhos stoichiometry remains unchanged.

There are some limitations associated with the methods used to assess autophagy and mitophagy. Notably, P62 is also a substrate for other signalling molecules (i.e. CASP6 or CASP8) and can be upregulated independently of truly altered autophagic flux, particularly in inflammatory settings[144]. LC3 tends to vary depending on the tissue, and antibodies may not be highly isotope specific (e.g. LC3A instead of LC3B), requiring careful interpretation in combination with other markers[192]. Although LC3 is subject to variations independent of autophagy, but LC3 turnover remaining unchanged, we believe the changes of P62 are negligible. Future *in vitro* validation was not feasible in our study due low yield of Tamoxifentreated, LC3-GFP–transfected fibroblasts, with mutation activation in only ~25-30% of cells. Mitophagy was induced by treatment with carbonyl cyanide 3-chlorophenylhydrazone (CCCP) for 12 hours, a strategy previously described[193]. However, some limitations lie in this approach since this staining is used for mitochondrial mass detection in the first place and is dependent on mtMP, making it unsuitable for quantitative measurement of mitophagy dynamics[194]. Knowing that uptake but not retention of Mitotracker relies on mtMP, cells were stained before treatment to allow proper evaluation. This technique was used solely to assess mitophagy induction in similarly treated samples, and we refrain from making any statements on quantitative mitophagy dynamics.

Our analysis was conducted four weeks after Bleomycin treatment, capturing the postinflammatory phase when fibrosis is most pronounced. Unlike studies focusing on earlier stages (e.g., Myeloid STAT-3 deficient mice at two weeks[170,195]), our results represent a single timepoint, and we cannot comment on inflammatory alterations occurring earlier. However, we chose the 4-week time point as fibrosis extent is most visible at that point in Bleomycin mouse models, with a peak of dermal thickness and collagen abundance[196]. Finally, as with all studies involving mice, this study contains limitations related to the restricted availability of animals, constraining the number of biological replicates and statistical power.

8. References

1. Kauppila TES, Kauppila JHK, Larsson NG. Mammalian Mitochondria and Aging: An Update. *Cell Metab* 2017; 25(1): 57-71.
2. Picca A, Guerra F, Calvani R, et al. The contribution of mitochondrial DNA alterations to aging, cancer, and neurodegeneration. *Exp Gerontol* 2023; 178: 112203.
3. Stewart JB, Chinnery PF. The dynamics of mitochondrial DNA heteroplasmy: implications for human health and disease. *Nat Rev Genet* 2015; 16(9): 530-42.
4. Kujoth GC, Bradshaw PC, Haroon S, Prolla TA. The role of mitochondrial DNA mutations in mammalian aging. *PLoS Genet* 2007; 3(2): e24.
5. Ross JM, Stewart JB, Hagstrom E, et al. Germline mitochondrial DNA mutations aggravate ageing and can impair brain development. *Nature* 2013; 501(7467): 412-5.
6. Smith KK, Moreira JD, Wilson CR, et al. A systematic review on the biochemical threshold of mitochondrial genetic variants. *Genome Res* 2024; 34(3): 341-65.
7. Liu X, Longchamps RJ, Wiggins KL, et al. Association of mitochondrial DNA copy number with cardiometabolic diseases. *Cell Genom* 2021; 1(1).
8. Saada A SA, Mandel H, Nevo Y, Eriksson S, Elpeleg O. Mutant mitochondrial thymidine kinase in mitochondrial DNA depletion myopathy. *Nat Genet* 2001 Nov;29(3):342-4. doi: 10.1038/ng751.
9. Goffart S, Cooper HM, Tyynismaa H, Wanrooij S, Suomalainen A, Spelbrink JN. Twinkle mutations associated with autosomal dominant progressive external ophthalmoplegia lead to impaired helicase function and in vivo mtDNA replication stalling. *Hum Mol Genet* 2009; 18(2): 328-40.
10. Kirschenbaum D, Hedberg-Oldfors C, Oldfors A, Scherer E, Budka H. Distinctive cerebral neuropathology in an adult case of sensory ataxic neuropathy with dysarthria and ophthalmoplegia (SANDO) syndrome. *Neuropathol Appl Neurobiol* 2018; 44(6): 639-42.
11. Moscatelli M, Ardissone A, Lamantea E, et al. Kearns-Sayre syndrome: expanding spectrum of a "novel" mitochondrial leukomyeloencephalopathy. *Neurol Sci* 2022; 43(3): 2081-4.
12. Rahman S. Mitochondrial disease in children. *J Intern Med* 2020; 287(6): 609-33.
13. Lopez-Otin C, Blasco MA, Partridge L, Serrano M, Kroemer G. Hallmarks of aging: An expanding universe. *Cell* 2023; 186(2): 243-78.
14. Trifunovic A, Wredenberg A, Falkenberg M, et al. Premature ageing in mice expressing defective mitochondrial DNA polymerase. *Nature* 2004; 429(6990): 417–23.
15. Stewart JB, Chinnery PF. Extreme heterogeneity of human mitochondrial DNA from organelles to populations. *Nat Rev Genet* 2021; 22(2): 106-18.
16. Monzio Compagnoni G, Di Fonzo A, Corti S, Comi GP, Bresolin N, Masliah E. The Role of Mitochondria in Neurodegenerative Diseases: the Lesson from Alzheimer's Disease and Parkinson's Disease. *Mol Neurobiol* 2020; 57(7): 2959-80.
17. Baris OR, Ederer S, Neuhaus JF, et al. Mosaic Deficiency in Mitochondrial Oxidative Metabolism Promotes Cardiac Arrhythmia during Aging. *Cell Metab* 2015; 21(5): 667-77.
18. Bodemer C. Hair and Skin Disorders as Signs of Mitochondrial Disease. *Paediatrics* 1999.
19. Feichtinger RG, Sperl W, Bauer JW, Kofler B. Mitochondrial dysfunction: a neglected component of skin diseases. *Experimental Dermatology* 2014; 23(9): 607-14.
20. Birket MJ, Birch-Machin MA. Ultraviolet radiation exposure accelerates the accumulation of the aging-dependent T414G mitochondrial DNA mutation in human skin. *Aging Cell* 2007; 6(4): 557-64.
21. Kurz B, Berneburg M, Baumler W, Karrer S. Phototherapy: Theory and practice. *J Dtsch Dermatol Ges* 2023; 21(8): 882-97.
22. Berneburg M, Plettenberg H, Medve-Konig K, et al. Induction of the photoaging-associated mitochondrial common deletion in vivo in normal human skin. *J Invest Dermatol* 2004; 122(5): 1277-83.
23. Cantanhede IG, Liu H, Liu H, et al. Exploring metabolism in scleroderma reveals opportunities for pharmacological intervention for therapy in fibrosis. *Frontiers in Immunology* 2022; 13. 73
24. Zhou X, Trinh-Minh T, Tran-Manh C, et al. Impaired Mitochondrial Transcription Factor A Expression Promotes Mitochondrial Damage to Drive Fibroblast Activation and Fibrosis in Systemic Sclerosis. *Arthritis Rheumatol* 2022; 74(5): 871-81.

25. Larsson NG. Somatic mitochondrial DNA mutations in mammalian aging. *Annu Rev Biochem* 2010; 79: 683-706.
26. Menon GK, Kligman AM. Barrier functions of human skin: a holistic view. *Skin Pharmacol Physiol* 2009; 22(4): 178-89.
27. Pilkington SM, Bulfone-Paus S, Griffiths CEM, Watson REB. Inflammaging and the Skin. *J Invest Dermatol* 2021; 141(4S): 1087-95.
28. Richard B. Weller MD FE, Hamish J.A. Hunter BSc (Hons), MBChB, MRCP (UK) (Derm), Margaret W. Mann The Function and Structure of the Skin; 2014.
29. Candi E, Schmidt R, Melino G. The cornified envelope: a model of cell death in the skin. *Nat Rev Mol Cell Biol* 2005; 6(4): 328-40.
30. Aleemardani M, Trikic MZ, Green NH, Claeyssens F. The Importance of Mimicking Dermal-Epidermal Junction for Skin Tissue Engineering: A Review. *Bioengineering (Basel)* 2021; 8(11).
31. Rittie L, Fisher GJ. Natural and sun-induced aging of human skin. *Cold Spring Harb Perspect Med* 2015; 5(1): a015370.
32. Driskell RR, Jahoda CA, Chuong CM, Watt FM, Horsley V. Defining dermal adipose tissue. *Exp Dermatol* 2014; 23(9): 629-31.
33. Chen BB LP, Shih TT, Liu TH, Shen YC, Lu LC, Lin ZZ, Hsu C, Hsu CH, Cheng AL, Shao YY. Sarcopenia and myosteatosis are associated with survival in patients receiving immunotherapy for advanced hepatocellular carcinoma. *Eur Radiol* 2023 Jan;33(1):512-522. doi: 10.1007/s00330-022-08980-4. Epub 2022 Jul 21.
34. Talbott HE, Mascharak S, Griffin M, Wan DC, Longaker MT. Wound healing, fibroblast heterogeneity, and fibrosis. *Cell Stem Cell* 2022; 29(8): 1161-80.
35. Ziegler E. General Pathology, or The Science of the Cause, Nature and Course of the Pathological Disturbances Which Occur in the Living Subject. *Journal of the American Medical Association* 1899; XXXIII(19): 1182-.
36. Tigges J, Krutmann J, Fritsche E, et al. The hallmarks of fibroblast ageing. *Mech Ageing Dev* 2014; 138: 26-44.
37. Schuster R, Younesi F, Ezzo M, Hinz B. The Role of Myofibroblasts in Physiological and Pathological Tissue Repair. *Cold Spring Harb Perspect Biol* 2023; 15(1).
38. Lu P, Takai K, Weaver VM, Werb Z. Extracellular matrix degradation and remodeling in development and disease. *Cold Spring Harb Perspect Biol* 2011; 3(12).
39. Dhouailly D. Formation of Cutaneous Appendages
in Dermo-Epidermal Recombinations
between Reptiles, Birds and Mammals. *Acta Biomaterialia* 1974.
40. Pakshir P, Alizadehgiashi M, Wong B, et al. Dynamic fibroblast contractions attract remote macrophages in fibrillar collagen matrix. *Nat Commun* 2019; 10(1): 1850.
41. Plikus MV, Wang X, Sinha S, et al. Fibroblasts: Origins, definitions, and functions in health and disease. *Cell* 2021; 184(15): 3852-72.
42. Juhl P, Bondesen S, Hawkins CL, et al. Dermal fibroblasts have different extracellular matrix profiles induced by TGF-beta, PDGF and IL-6 in a model for skin fibrosis. *Sci Rep* 2020; 10(1): 17300.
43. Ferrer RA, Saalbach A, Grunwedel M, et al. Dermal Fibroblasts Promote Alternative Macrophage Activation Improving Impaired Wound Healing. *J Invest Dermatol* 2017; 137(4): 941-50.
44. Olson LE, Soriano P. Increased PDGFRalpha activation disrupts connective tissue development and drives systemic fibrosis. *Dev Cell* 2009; 16(2): 303-13.
45. Gonzalez R, Moffatt G, Hagner A, et al. Platelet-derived growth factor signaling modulates adult hair follicle dermal stem cell maintenance and self-renewal. *NPJ Regen Med* 2017; 2: 11.
46. Siadat SM, Ruberti JW. Mechanochemistry of collagen. *Acta Biomater* 2023; 163: 50-62.
47. Malfait F, Symoens S, Coucke P, Nunes L, De Almeida S, De Paepe A. Total absence of the alpha2(I) chain of collagen type I causes a rare form of Ehlers-Danlos syndrome with hypermobility and propensity to cardiac valvular problems. *J Med Genet* 2006; 43(7): e36.

48. Zhu J, Hoop CL, Case DA, Baum J. Cryptic binding sites become accessible through surface reconstruction of the type I collagen fibril. *Sci Rep* 2018; 8(1): 16646.
49. Darby IA, Laverdet B, Bonte F, Desmouliere A. Fibroblasts and myofibroblasts in wound healing. *Clin Cosmet Investig Dermatol* 2014; 7: 301-11.
50. Eming SA, Wynn TA, Martin P. Inflammation and metabolism in tissue repair and regeneration. *Science* 2017.
51. Rigau AR, Luber M, Distler JHW. Mouse Models of Skin Fibrosis. *Methods in Molecular Biology* 2021.
52. Bueno M, Papazoglou A, Valenzi E, Rojas M, Lafyatis R, Mora AL. Mitochondria, Aging, and Cellular Senescence: Implications for Scleroderma. *Curr Rheumatol Rep* 2020; 22(8): 37.
53. Rockey DC, Bell PD, Hill JA. Fibrosis--a common pathway to organ injury and failure. *N Engl J Med* 2015; 372(12): 1138-49.
54. Henderson NC, Rieder F, Wynn TA. Fibrosis: from mechanisms to medicines. *Nature* 2020; 587(7835): 555-66.
55. Weiskirchen R, Weiskirchen S, Tacke F. Organ and tissue fibrosis: Molecular signals, cellular mechanisms and translational implications. *Mol Aspects Med* 2019; 65: 2-15.
56. Ramachandran P, Iredale JP. Macrophages: central regulators of hepatic fibrogenesis and fibrosis resolution. *J Hepatol* 2012; 56(6): 1417-9.
57. Peng D, Fu M, Wang M, Wei Y, Wei X. Targeting TGF-beta signal transduction for fibrosis and cancer therapy. *Mol Cancer* 2022; 21(1): 104.
58. Gieseck RL, 3rd, Wilson MS, Wynn TA. Type 2 immunity in tissue repair and fibrosis. *Nat Rev Immunol* 2018; 18(1): 62-76.
59. Amico D, Spadoni T, Rovinelli M, et al. Intracellular free radical production by peripheral blood T lymphocytes from patients with systemic sclerosis: role of NADPH oxidase and ERK1/2. *Arthritis Res Ther* 2015; 17(1): 68.
60. Barnes JL, Gorin Y. Myofibroblast differentiation during fibrosis: role of NAD(P)H oxidases. *Kidney Int* 2011; 79(9): 944-56.
61. Del Campo JA, Gallego P, Grande L. Role of inflammatory response in liver diseases: Therapeutic strategies. *World J Hepatol* 2018; 10(1): 1-7.
62. Hammerich L, Tacke F. Interleukins in chronic liver disease: lessons learned from experimental mouse models. *Clin Exp Gastroenterol* 2014; 7: 297-306.
63. van Caam A, Vonk M, van den Hoogen F, van Lent P, van der Kraan P. Unraveling SSc Pathophysiology; The Myofibroblast. *Front Immunol* 2018; 9: 2452.
64. Katsumoto TR, Whitfield ML, Connolly MK. The pathogenesis of systemic sclerosis. *Annu Rev Pathol* 2011; 6: 509-37.
65. Kim KK, Sheppard D, Chapman HA. TGF-beta1 Signaling and Tissue Fibrosis. *Cold Spring Harb Perspect Biol* 2018; 10(4).
66. Sonnylal S, Denton CP, Zheng B, et al. Postnatal induction of transforming growth factor beta signaling in fibroblasts of mice recapitulates clinical, histologic, and biochemical features of scleroderma. *Arthritis Rheum* 2007; 56(1): 334-44.
67. Luong VH, Chino T, Oyama N, et al. Blockade of TGF-beta/Smad signaling by the small compound HPH-15 ameliorates experimental skin fibrosis. *Arthritis Res Ther* 2018; 20(1): 46.
68. Shull MM. Targeted disruption of the mouse transforming growth factor-β1 gene results in multifocal inflammatory disease. *Nature* 1992.
69. Kulkarni AB. Transforming growth factor beta 1 null mutation in mice causes excessive inflammatory response and early death. *Proc Nati Acad Sci USA* 1993.
70. Wynn TA, Ramalingam TR. Mechanisms of fibrosis: therapeutic translation for fibrotic disease. *Nat Med* 2012; 18(7): 1028-40.
71. Lancaster LH, de Andrade JA, Zibrak JD, et al. Pirfenidone safety and adverse event management in idiopathic pulmonary fibrosis. *Eur Respir Rev* 2017; 26(146).
72. Dees C, Chakraborty D, Distler JHW. Cellular and molecular mechanisms in fibrosis. *Exp Dermatol* 2021; 30(1): 121-31.
73. Jun JI, Lau LF. Resolution of organ fibrosis. *J Clin Invest* 2018; 128(1): 97-107.

74. Kaissling B, Lehir M, Kriz W. Renal epithelial injury and fibrosis. *Biochim Biophys Acta* 2013; 1832(7): 931-9.
75. Rombold S, Lobisch K, Katzer K, Grazziotin TC, Ring J, Eberlein B. Efficacy of UVA1 phototherapy in 230 patients with various skin diseases. *Photodermatol Photoimmunol Photomed* 2008; 24(1): 19-23.
76. Gill SE, Huizar I, Bench EM, et al. Tissue inhibitor of metalloproteinases 3 regulates resolution of inflammation following acute lung injury. *Am J Pathol* 2010; 176(1): 64-73.
77. Raghu G, Brown KK, Collard HR, et al. Efficacy of simtuzumab versus placebo in patients with idiopathic pulmonary fibrosis: a randomised, double-blind, controlled, phase 2 trial. *Lancet Respir Med* 2017; 5(1): 22-32.
78. Oakley F, Teoh V, Ching ASG, et al. Angiotensin II activates I kappaB kinase phosphorylation of RelA at Ser 536 to promote myofibroblast survival and liver fibrosis. *Gastroenterology* 2009; 136(7): 2334-44 e1.
79. Anan A, Baskin-Bey ES, Bronk SF, Werneburg NW, Shah VH, Gores GJ. Proteasome inhibition induces hepatic stellate cell apoptosis. *Hepatology* 2006; 43(2): 335-44.
80. Jun JI, Lau LF. The matricellular protein CCN1 induces fibroblast senescence and restricts fibrosis in cutaneous wound healing. *Nat Cell Biol* 2010; 12(7): 676-85.
81. Maltseva O. Fibroblast Growth Factor Reversal of the Corneal Myofibroblast Phenotype. *Investigative Ophthalmology & Visual Science* 2001.
82. Plikus MV, Guerrero-Juarez CF, Ito M, et al. Regeneration of fat cells from myofibroblasts during wound healing. *Science* 2017; 355(6326): 748-52.
83. Gyorfi AH, Matei AE, Distler JHW. Targeting TGF-beta signaling for the treatment of fibrosis. *Matrix Biol* 2018; 68-69: 8-27.
84. Weiland D, Brachvogel B, Hornig-Do HT, et al. Imbalance of Mitochondrial Respiratory Chain Complexes in the Epidermis Induces Severe Skin Inflammation. *J Invest Dermatol* 2018; 138(1): 132-40.
85. Baris OR, Klose A, Kloepper JE, et al. The mitochondrial electron transport chain is dispensable for proliferation and differentiation of epidermal progenitor cells. *Stem Cells* 2011; 29(9): 1459-68.
86. Hamanaka RB, Glasauer A, Hoover P, et al. Mitochondrial reactive oxygen species promote epidermal differentiation and hair follicle development. *Sci Signal* 2013; 6(261): ra8.
87. Krutmann J, Schroeder P. Role of mitochondria in photoaging of human skin: the defective powerhouse model. *J Investig Dermatol Symp Proc* 2009; 14(1): 44-9.
88. Yanes B, Rainero E. The Interplay between Cell-Extracellular Matrix Interaction and Mitochondria Dynamics in Cancer. *Cancers (Basel)* 2022; 14(6).
89. Zanotelli MR, Goldblatt ZE, Miller JP, et al. Regulation of ATP utilization during metastatic cell migration by collagen architecture. *Mol Biol Cell* 2018; 29(1): 1-9.
90. Akamata K. SIRT3 is attenuated in systemic sclerosis skin and lungs, and its pharmacologic activation mitigates organ fibrosis. *Oncotarget* 2016.
91. Kizilay Mancini O, Acevedo M, Fazez N, et al. Oxidative stress-induced senescence mediates inflammatory and fibrotic phenotypes in fibroblasts from systemic sclerosis patients. *Rheumatology (Oxford)* 2022; 61(3): 1265-75.
92. Sreedhar A, Aguilera-Aguirre L, Singh KK. Mitochondria in skin health, aging, and disease. *Cell Death & Disease* 2020; 11(6).
93. Harman D. Aging: a theory based on free radical and radiation chemistry. *J Gerontol* 1956; 11(3): 298-300.
94. Koziel R, Greussing R, Maier AB, Declercq L, Jansen-Durr P. Functional interplay between mitochondrial and proteasome activity in skin aging. *J Invest Dermatol* 2011; 131(3): 594-603.
95. DeBalsi KL, Hoff KE, Copeland WC. Role of the mitochondrial DNA replication machinery in mitochondrial DNA mutagenesis, aging and age-related diseases. *Ageing Res Rev* 2017; 33: 89-104.
96. Berneburg M, Kamenisch Y, Krutmann J, Rocken M. 'To repair or not to repair - no longer a question': repair of mitochondrial DNA shielding against age and cancer. *Exp Dermatol* 2006; 15(12): 1005-15.

97. Kennedy SR, Salk JJ, Schmitt MW, Loeb LA. Ultra-sensitive sequencing reveals an age-related increase in somatic mitochondrial mutations that are inconsistent with oxidative damage. *PLoS Genet* 2013; 9(9): e1003794.
98. Kauppila JH, Stewart JB. Mitochondrial DNA: Radically free of free-radical driven mutations. *Biochim Biophys Acta* 2015; 1847(11): 1354-61.
99. Lehmann D, Tuppen HAL, Campbell GE, et al. Understanding mitochondrial DNA maintenance disorders at the single muscle fibre level. *Nucleic Acids Res* 2019; 47(14): 7430-43.
100. Wiesner RJ, Zsurka G, Kunz WS. Mitochondrial DNA damage and the aging process: facts and imaginations. *Free Radic Res* 2006; 40(12): 1284-94.
101. Stout R, Birch-Machin M. Mitochondria's Role in Skin Ageing. *Biology (Basel)* 2019; 8(2).
102. Eshaghian A, Vleugels RA, Canter JA, McDonald MA, Stasko T, Sligh JE. Mitochondrial DNA deletions serve as biomarkers of aging in the skin, but are typically absent in nonmelanoma skin cancers. *J Invest Dermatol* 2006; 126(2): 336-44.
103. Wang AS, Dreesen O. Biomarkers of Cellular Senescence and Skin Aging. *Front Genet* 2018; 9: 247.
104. Kaneko N, Vierkoetter A, Kraemer U, et al. Mitochondrial common deletion mutation and extrinsic skin ageing in German and Japanese women. *Exp Dermatol* 2012; 21 Suppl 1: 26-30.
105. Powers JM, Murphy G, Ralph N, O'Gorman SM, Murphy JE. Mitochondrial DNA deletion percentage in sun exposed and non sun exposed skin. *J Photochem Photobiol B* 2016; 165: 277-82.
106. Majora M, Wittkampf T, Schuermann B, et al. Functional consequences of mitochondrial DNA deletions in human skin fibroblasts: increased contractile strength in collagen lattices is due to oxidative stress-induced lysyl oxidase activity. *Am J Pathol* 2009; 175(3): 1019-29.
107. Singh B, Schoeb TR, Bajpai P, Slominski A, Singh KK. Reversing wrinkled skin and hair loss in mice by restoring mitochondrial function. *Cell Death Dis* 2018; 9(7): 735.
108. Ajoolabady A, Pratico D, Tang D, Zhou S, Franceschi C, Ren J. Immunosenescence and inflammaging: Mechanisms and role in diseases. *Ageing Res Rev* 2024; 101: 102540.
109. Ghosh-Choudhary SK, Liu J, Finkel T. The role of mitochondria in cellular senescence. *FASEB J* 2021; 35(12): e21991.
110. Huttemann M, Lee I, Samavati L, Yu H, Doan JW. Regulation of mitochondrial oxidative phosphorylation through cell signaling. *Biochim Biophys Acta* 2007; 1773(12): 1701-20.
111. Davies AM, Holt AG. Modeling mitochondria, where are the numbers? *Neural Regen Res* 2024; 19(7): 1435-6.
112. Tabara LC, Segawa M, Prudent J. Molecular mechanisms of mitochondrial dynamics. *Nat Rev Mol Cell Biol* 2025; 26(2): 123-46.
113. Martic I, Papaccio F, Bellei B, Cavinato M. Mitochondrial dynamics and metabolism across skin cells: implications for skin homeostasis and aging. *Front Physiol* 2023; 14: 1284410.
114. Mellem D, Sattler M, Pagel-Wolff S, et al. Fragmentation of the mitochondrial network in skin in vivo. *PLoS One* 2017; 12(6): e0174469.
115. Rorteau J, Chevalier FP, Bonnet S, et al. Maintenance of Chronological Aging Features in Culture of Normal Human Dermal Fibroblasts from Old Donors. *Cells* 2022; 11(5).
116. Wedel S, Martic I, Guerrero Navarro L, et al. Depletion of growth differentiation factor 15 (GDF15) leads to mitochondrial dysfunction and premature senescence in human dermal fibroblasts. *Aging Cell* 2023; 22(1): e13752.
117. Calvo SE, Clauser KR, Mootha VK. MitoCarta2.0: an updated inventory of mammalian mitochondrial proteins. *Nucleic Acids Res* 2016; 44(D1): D1251-7.
118. Fontana GA, Gahlon HL. Mechanisms of replication and repair in mitochondrial DNA deletion formation. *Nucleic Acids Research* 2020; 48(20): 11244-58.
119. Gupta R, Kanai M, Durham TJ, et al. Nuclear genetic control of mtDNA copy number and heteroplasmy in humans. *Nature* 2023; 620(7975): 839-48.
120. Falkenberg M, Larsson NG, Gustafsson CM. Replication and Transcription of Human Mitochondrial DNA. *Annu Rev Biochem* 2024; 93(1): 47-77.
121. Falkenberg JPUM. In Vitro Analysis of mtDNA Replication; 2020.

122. Tyynismaa H, Sembongi H, Bokori-Brown M, et al. Twinkle helicase is essential for mtDNA maintenance and regulates mtDNA copy number. *Hum Mol Genet* 2004; 13(24): 3219-27.
123. Milenkovic D, Matic S, Kuhl I, et al. TWINKLE is an essential mitochondrial helicase required for synthesis of nascent D-loop strands and complete mtDNA replication. *Hum Mol Genet* 2013; 22(10): 1983-93.
124. Jin S, Bueno C, Lu W, et al. Computationally exploring the mechanism of bacteriophage T7 gp4 helicase translocating along ssDNA. *Proc Natl Acad Sci U S A* 2022; 119(32): e2202239119.
125. Fernandez-Millan P, Lazaro M, Cansiz-Arda S, et al. The hexameric structure of the human mitochondrial replicative helicase Twinkle. *Nucleic Acids Res* 2015; 43(8): 4284-95.
126. Peter B, Farge G, Pardo-Hernandez C, Tangefjord S, Falkenberg M. Structural basis for adPEO-causing mutations in the mitochondrial TWINKLE helicase. *Hum Mol Genet* 2019; 28(7): 1090-9.
127. Bing Zheng ZZ, Carol M. Black. Ligand-Dependent Genetic Recombination in Fibroblasts. *American Journal of Pathology* 2002; Vol. 160.
128. Blyszczuk P, Kozlova A, Guo Z, Kania G, Distler O. Experimental Mouse Model of Bleomycin-Induced Skin Fibrosis. *Curr Protoc Immunol* 2019; 126(1): e88.
129. Xian H LY, Rundberg Nilsson A, Gatchalian R, Crother TR, Tourtellotte WG, Zhang Y, Aleman-Muench GR, Lewis G, Chen W, Kang S, Luevanos M, Trudler D, Lipton SA, Soroosh P, Teijaro J, de la Torre JC, Arditi M, Karin M, Sanchez-Lopez E. Metformin inhibition of mitochondrial ATP and DNA synthesis abrogates NLRP3 inflammasome activation and pulmonary inflammation. *Immunity* 2021 Jul 13;54(7):1463-1477.e11. doi: 10.1016/j.immuni.2021.05.004. Epub 2021 Jun 10.
130. Sanchez-Spitman AB, Swen JJ, Dezentje VO, Moes D, Gelderblom H, Guchelaar HJ. Clinical pharmacokinetics and pharmacogenetics of tamoxifen and endoxifen. *Expert Rev Clin Pharmacol* 2019; 12(6): 523-36.
131. Willenborg S, Eckes B, Brinckmann J, et al. Genetic ablation of mast cells redefines the role of mast cells in skin wound healing and bleomycin-induced fibrosis. *J Invest Dermatol* 2014; 134(7): 2005-15.
132. Gray PADG. PCR Mutation Detection Protocols; 2002.
133. Forsström S JC, Carroll CJ, Kuronen M, Pirinen E, Pradhan S, Marmyleva A, Auranen M, Kleine IM, Khan NA, Roivainen A, Marjamäki P, Liljenbäck H, Wang L, Battersby BJ, Richter U, Velagapudi V, Nikkanen J, Euro L, Suomalainen A. Fibroblast Growth Factor 21 Drives Dynamics of Local and Systemic Stress Responses in Mitochondrial Myopathy with mtDNA Deletions. *Cell Metab* 2019 Dec 3;30(6):1040-1054.e7. doi: 10.1016/j.cmet.2019.08.019. Epub 2019 Sep 12.
134. Al-Janobi A. Performance evaluation of cross-diagonal texture
matrix method of texture analysis. *Pattern recognition* 1999.
135. Gibb AA, Lazaropoulos MP, Elrod JW. Myofibroblasts and Fibrosis: Mitochondrial and Metabolic Control of Cellular Differentiation. *Circ Res* 2020; 127(3): 427-47.
136. Avram CE, Cooper TG. Development of the caput epididymidis studied by expressed proteins (a glutamate transporter, a lipocalin and beta-galactosidase) in the c-ros knockout and wild-type mice with prepubertally ligated efferent ducts. *Cell Tissue Res* 2004; 317(1): 23-34.
137. Yoshimoto S, Yoshida M, Ando H, Ichihashi M. Establishment of Photoaging In Vitro by Repetitive UVA Irradiation: Induction of Characteristic Markers of Senescence and its Prevention by PAPLAL with Potent Catalase Activity. *Photochem Photobiol* 2018; 94(3): 438-44.
138. Wanrooij S, Goffart S, Pohjoismaki JL, Yasukawa T, Spelbrink JN. Expression of catalytic mutants of the mtDNA helicase Twinkle and polymerase POLG causes distinct replication stalling phenotypes. *Nucleic Acids Res* 2007; 35(10): 3238-51.
139. Cicchi R, Kapsokalyvas D, De Giorgi V, et al. Scoring of collagen organization in healthy and diseased human dermis by multiphoton microscopy. *J Biophotonics* 2010; 3(1-2): 34-43.
140. Kendall RT, Feghali-Bostwick CA. Fibroblasts in fibrosis: novel roles and mediators. *Front Pharmacol* 2014; 5: 123.
141. Russell OM, Fruh I, Rai PK, et al. Preferential amplification of a human mitochondrial DNA deletion in vitro and in vivo. *Sci Rep* 2018; 8(1): 1799.

142. Reiter L, Niehoff N, Weiland D, et al. Mitochondrial DNA mutations attenuate Bleomycin-induced dermal fibrosis by inhibiting differentiation into myofibroblasts. *Matrix Biol* 2024.
143. Dimri GP, Lee X, Basile G, et al. A biomarker that identifies senescent human cells in culture and in aging skin in vivo. *Proc Natl Acad Sci U S A* 1995; 92(20): 9363-7.
144. Klionsky DJ, Abdelmohsen K, Abe A, et al. Guidelines for the use and interpretation of assays for monitoring autophagy (3rd edition). *Autophagy* 2016; 12(1): 1-222.
145. Bianco A, Valletti A, Longo G, et al. Mitochondrial DNA copy number in affected and unaffected LHON mutation carriers. *BMC Research Notes* 2018; 11(1).
146. Bianco A, Bisceglia L, Russo L, et al. High Mitochondrial DNA Copy Number Is a Protective Factor From Vision Loss in Heteroplasmic Leber's Hereditary Optic Neuropathy (LHON). *Invest Ophthalmol Vis Sci* 2017; 58(4): 2193-7.
147. Grady JP, Pickett SJ, Ng YS, et al. mtDNA heteroplasmy level and copy number indicate disease burden in m.3243A>G mitochondrial disease. *EMBO Mol Med* 2018; 10(6).
148. Haumann S, Boix J, Knuever J, et al. Mitochondrial DNA mutations induce mitochondrial biogenesis and increase the tumorigenic potential of Hodgkin and Reed-Sternberg cells. *Carcinogenesis* 2020; 41(12): 1735-45.
149. Sanchez-Contreras M, Sweetwyne MT, Tsantilas KA, et al. The multi-tissue landscape of somatic mtDNA mutations indicates tissue-specific accumulation and removal in aging. *Elife* 2023; 12.
150. Holzer T, Probst K, Etich J, et al. Respiratory chain inactivation links cartilage-mediated growth retardation to mitochondrial diseases. *Journal of Cell Biology* 2019; 218(6): 1853-70.
151. Lapointe J, Hekimi S. Early mitochondrial dysfunction in long-lived Mclk1+/- mice. *J Biol Chem* 2008; 283(38): 26217-27.
152. Blagov AV, Summerhill VI, Sukhorukov VN, Zhigmitova EB, Postnov AY, Orekhov AN. Potential use of antioxidants for the treatment of chronic inflammatory diseases. *Front Pharmacol* 2024; 15: 1378335.
153. Vermulst M, Bielas JH, Kujoth GC, et al. Mitochondrial point mutations do not limit the natural lifespan of mice. *Nat Genet* 2007; 39(4): 540-3.
154. Hayashi J-i. Introduction of disease-related mitochondrial DNA deletions into. 1991.
155. Gazdhar A, Lebrecht D, Roth M, et al. Time-dependent and somatically acquired mitochondrial DNA mutagenesis and respiratory chain dysfunction in a scleroderma model of lung fibrosis. *Sci Rep* 2014; 4: 5336.
156. Jaeger VK, Lebrecht D, Nicholson AG, et al. Mitochondrial DNA mutations and respiratory chain dysfunction in idiopathic and connective tissue disease-related lung fibrosis. *Sci Rep* 2019; 9(1): 5500.
157. Fang F, Marangoni RG, Zhou X, et al. Toll-like Receptor 9 Signaling Is Augmented in Systemic Sclerosis and Elicits Transforming Growth Factor beta-Dependent Fibroblast Activation. *Arthritis Rheumatol* 2016; 68(8): 1989-2002.
158. Caza TN, Fernandez DR, Talaber G, et al. HRES-1/Rab4-mediated depletion of Drp1 impairs mitochondrial homeostasis and represents a target for treatment in SLE. *Annals of the Rheumatic Diseases* 2014; 73(10): 1888-97.
159. Berneburg M, Grether-Beck S, Kurten V, et al. Singlet oxygen mediates the UVA-induced generation of the photoaging-associated mitochondrial common deletion. *J Biol Chem* 1999; 274(22): 15345-9.
160. Wei M, He X, Liu N, Deng H. Role of reactive oxygen species in ultraviolet-induced photodamage of the skin. *Cell Div* 2024; 19(1): 1.
161. Tognetti L, Marrocco C, Carraro A, et al. Clinical and laboratory characterization of patients with localized scleroderma and response to UVA-1 phototherapy: In vivo and in vitro skin models. *Photodermatol Photoimmunol Photomed* 2022; 38(6): 531-40.
162. Yun J, Finkel T. Mitohormesis. *Cell Metab* 2014; 19(5): 757-66.
163. Cheng YW, Liu J, Finkel T. Mitohormesis. *Cell Metab* 2023; 35(11): 1872-86.

164. Schulz TJ, Zarse K, Voigt A, Urban N, Birringer M, Ristow M. Glucose restriction extends Caenorhabditis elegans life span by inducing mitochondrial respiration and increasing oxidative stress. *Cell Metab* 2007; 6(4): 280-93.
165. Tomer D, Chippalkatti R, Mitra K, Rikhy R. ERK regulates mitochondrial membrane potential in fission deficient Drosophila follicle cells during differentiation. *Dev Biol* 2018; 434(1): 48-62.
166. Forrester SJ, Kikuchi DS, Hernandes MS, Xu Q, Griendling KK. Reactive Oxygen Species in Metabolic and Inflammatory Signaling. *Circulation Research* 2018; 122(6): 877-902.
167. Zhang K, Yao E, Chen B, et al. Acquisition of cellular properties during alveolar formation requires differential activity and distribution of mitochondria. *Elife* 2022; 11.
168. Hinz B, Lagares D. Evasion of apoptosis by myofibroblasts: a hallmark of fibrotic diseases. *Nat Rev Rheumatol* 2020; 16(1): 11-31.
169. Phan H-YZaSH. Inhibition of Myofibroblast Apoptosis by Transforming Growth Factor β1 *Am J Respir Cell Mol Biol* 1999.
170. Do NN, Willenborg S, Eckes B, et al. Myeloid Cell-Restricted STAT3 Signaling Controls a Cell-Autonomous Antifibrotic Repair Program. *J Immunol* 2018; 201(2): 663-74.
171. Kissin EY, Merkel PA, Lafyatis R. Myofibroblasts and hyalinized collagen as markers of skin disease in systemic sclerosis. *Arthritis Rheum* 2006; 54(11): 3655-60.
172. Rajkumar VS, Howell K, Csiszar K, Denton CP, Black CM, Abraham DJ. Shared expression of phenotypic markers in systemic sclerosis indicates a convergence of pericytes and fibroblasts to a myofibroblast lineage in fibrosis. *Arthritis Res Ther* 2005; 7(5): R1113-23.
173. Tabib T, Huang M, Morse N, et al. Myofibroblast transcriptome indicates SFRP2(hi) fibroblast progenitors in systemic sclerosis skin. *Nat Commun* 2021; 12(1): 4384.
174. Shook BA, Wasko RR, Rivera-Gonzalez GC, et al. Myofibroblast proliferation and heterogeneity are supported by macrophages during skin repair. *Science* 2018; 362(6417).
175. Zehender A, Li YN, Lin NY, et al. TGFbeta promotes fibrosis by MYST1-dependent epigenetic regulation of autophagy. *Nat Commun* 2021; 12(1): 4404.
176. Sen A, Kallabis S, Gaedke F, et al. Mitochondrial membrane proteins and VPS35 orchestrate selective removal of mtDNA. *Nat Commun* 2022; 13(1): 6704.
177. Chapman J, Fielder E, Passos JF. Mitochondrial dysfunction and cell senescence: deciphering a complex relationship. *FEBS Letters* 2019; 593(13): 1566-79.
178. Correia-Melo C, Marques FDM, Anderson R, et al. Mitochondria are required for pro-ageing features of the senescent phenotype. *The EMBO Journal* 2016; 35(7): 724-42.
179. Demaria M, Ohtani N, Youssef SA, et al. An essential role for senescent cells in optimal wound healing through secretion of PDGF-AA. *Dev Cell* 2014; 31(6): 722-33.
180. Quesnel K, Shi-Wen X, Hutchenreuther J, et al. CCN1 expression by fibroblasts is required for bleomycin-induced skin fibrosis. *Matrix Biol Plus* 2019; 3: 100009.
181. Al-Adwi Y, Westra J, van Goor H, et al. Transcriptomic analyses of lung tissues reveal key genes associated with progression of systemic sclerosis-interstitial lung disease (SSc-ILD). *J Autoimmun* 2024; 148: 103297.
182. Zhao X, Psarianos P, Ghoraie LS, et al. Metabolic regulation of dermal fibroblasts contributes to skin extracellular matrix homeostasis and fibrosis. *Nat Metab* 2019; 1(1): 147-57.
183. Bernard K, Logsdon NJ, Ravi S, et al. Metabolic Reprogramming Is Required for Myofibroblast Contractility and Differentiation. *J Biol Chem* 2015; 290(42): 25427-38.
184. Goodwin J, Choi H, Hsieh MH, et al. Targeting Hypoxia-Inducible Factor-1alpha/Pyruvate Dehydrogenase Kinase 1 Axis by Dichloroacetate Suppresses Bleomycin-induced Pulmonary Fibrosis. *Am J Respir Cell Mol Biol* 2018; 58(2): 216-31.
185. Chrysanthopoulou A, Mitroulis I, Apostolidou E, et al. Neutrophil extracellular traps promote differentiation and function of fibroblasts. *J Pathol* 2014; 233(3): 294-307.
186. Frangou E, Chrysanthopoulou A, Mitsios A, et al. REDD1/autophagy pathway promotes thromboinflammation and fibrosis in human systemic lupus erythematosus (SLE) through NETs decorated with tissue factor (TF) and interleukin-17A (IL-17A). *Ann Rheum Dis* 2019; 78(2): 238-48.

187. Mia MM, Boersema M, Bank RA. Interleukin-1beta attenuates myofibroblast formation and extracellular matrix production in dermal and lung fibroblasts exposed to transforming growth factor-beta1. *PLoS One* 2014; 9(3): e91559.
188. Sato. Serum levels of interleukin-6 and interleukin-10 correlate with total skin thickness score in patients with systemic sclerosis. *Journal of Dermatological Science* 2001.
189. Forsstrom S, Jackson CB, Carroll CJ, et al. Fibroblast Growth Factor 21 Drives Dynamics of Local and Systemic Stress Responses in Mitochondrial Myopathy with mtDNA Deletions. *Cell Metab* 2019; 30(6): 1040-54 e7.
190. Meng F, Khoso MH, Kang K, et al. FGF21 ameliorates hepatic fibrosis by multiple mechanisms. *Mol Biol Rep* 2021; 48(11): 7153-63.
191. Jia MQ, Guan CX, Tao JH, Zhou Y. Research Progress of Fibroblast Growth Factor 21 in Fibrotic Diseases. *Oxid Med Cell Longev* 2022; 2022: 5042762.
192. Klionsky DJ. Guidelines for the use and interpretation of assays for monitoring autophagy. *Autophagy* 2012.
193. Mauro-Lizcano M, Esteban-Martinez L, Seco E, et al. New method to assess mitophagy flux by flow cytometry. *Autophagy* 2015; 11(5): 833-43.
194. Xiao B, Deng X, Zhou W, Tan EK. Flow Cytometry-Based Assessment of Mitophagy Using MitoTracker. *Front Cell Neurosci* 2016; 10: 76.
195. Zehender A, Huang J, Gyorfi AH, et al. The tyrosine phosphatase SHP2 controls TGFbeta-induced STAT3 signaling to regulate fibroblast activation and fibrosis. *Nat Commun* 2018; 9(1): 3259.
196. Yamamoto T, Takagawa S, Katayama I, et al. Animal model of sclerotic skin. I: Local injections of bleomycin induce sclerotic skin mimicking scleroderma. *J Invest Dermatol* 1999; 112(4): 456-62.

9. Appendix

9.1 Table of Figures

9.2 List of tables

10. Publication of Results

10.1 Publication upon the submitted thesis

Reiter L, Niehoff N, Weiland D, Helbig D, Eming SA, Krieg T, Etich J, Brachvogel B, Wiesner RJ, Knuever J. Mitochondrial DNA mutations attenuate Bleomycin-induced dermal fibrosis by inhibiting differentiation into myofibroblasts. Matrix Biol. 2024 Sep;132:72-86. doi: 10.1016/j.matbio.2024.07.002. Epub 2024 Jul 14. PMID: 39009171.